EXPERIMENTAL INVESTIGATION OF CONVECTIVE FLOW BOILING IN CONCENTRIC AND ECCENTRIC ANNULUS

A Dissertation

by

JOSEPH SEO

Submitted to the Graduate and Professional School of
Texas A&M University
in partial fulfillment of the requirements for the degree of

DOCTOR OF PHILOSOPHY

Chair of Committee,	Yassin A. Hassan
Committee Members,	Kalyan Annamalai
	Rodolfo Vaghetto
	Thien Nguyen
Head of Department,	Michael Nastasi

December 2021

Major Subject: Nuclear Engineering

ABSTRACT

The convective boiling heat transfer of annular flow in concentric and eccentric annuli was investigated experimentally using a central heating rod in an unheated tube. Advanced measurement techniques—laser-induced fluorescence (LIF) and confocal chromatic sensor (CCS)—were applied to acquire the dynamics and instabilities of the liquid thin film on the tube. Boundary conditions included a heating rod heat flux (167–201 kW/m^2) and mass flow rate (58–155 g/s); the annuli in which the flow occurred have a hydraulic diameter of 15.5 mm. Previous research on isothermal annular flow in bare tubes indicated that vapor superficial velocity is a primary factor that influences liquid film dynamics including base film thickness and wave amplitude. The liquid film thickness in eccentric geometry was found to be constant for liquid superficial velocities ranging from 0.15–0.34 m/s and vapor superficial velocities ranging from 6.5–13.2 m/s. The heat transfer coefficient ranged from 2.734–4.279 $kW/m^2{\cdot}K$ and 2.063–3.096 $kW/m^2{\cdot}K$ for the concentric and eccentric geometries, respectively. The heat transfer coefficient showed an increasing trend with an increase in the liquid superficial velocity; a reverse trend was observed for the vapor superficial velocity. The boiling condition was assumed to be dry out when the measured heat transfer coefficient was exceptionally low (< ~2.0 $kW/m^2{\cdot}K$).

A flow boiling computational fluid dynamics (CFD) simulation was performed using the volume of fluid (VOF) method. Phase change models such as the Lee, Sun, and Chen models were implemented in OpenFOAM and tested. The film thickness data

obtained from the flow boiling simulation were compared with the experimental data to determine the mass transfer intensity (β_e) for the Lee model. The simulation result with $\beta_e = 0.3$ showed the best match with the experimental result.

ACKNOWLEDGEMENTS

I would like to thank my committee chair, Dr. Hassan, and my committee members, Dr. Annamalai, Dr. Vaghetto, and Dr. Nguyen, for their guidance and support throughout the course of this research.

Thanks also go to my friends and colleagues and the department faculty and staff for making my time at Texas A&M University a great experience.

Finally, thanks to my wife, Hansol for her patience and love and to my mother and father for their encouragement.

CONTRIBUTORS AND FUNDING SOURCES

Contributors

This work was supervised by a thesis (or) dissertation committee consisting of Professor Yassin Hassan and Kalyan Annamalai of the Department of Mechanical Engineering and Professor Rodolfo Vaghetto of the Department of Nuclear Engineering and Doctor Thien Nguyen.

All other work conducted for the dissertation was completed by the student independently.

Funding Sources

A part of this study is based upon work for The Consortium for Advanced Simulation of LWRs (CASL) project supported by the Department of Energy. A part of this study is also supported by summer internship program in Idaho National Laboratory (INL).

TABLE OF CONTENTS

Page

LIST OF FIGURES

Page

LIST OF TABLES

Page

CHAPTER I

INTRODUCTION [*]

The concept of two-phase fluid flow covers an exceedingly wide range of subjects including liquid–gas, liquid–liquid, liquid–solid, and gas–solid flows. Since these flows widely exist in industrial applications, it is very important to understand the natural phenomena related to these flows. Among them, the liquid–gas flow is the most widely used because it includes the entire subject of boiling (Hewitt & Hall-Taylor, 1970). Industrial plants that include evaporators, condensers, distillation towers, turbines, and nuclear power plants are some examples that require a considerable amount of understanding about liquid–gas two-phase flow. In pressurized water reactors (PWRs), liquid–gas two-phase flow is observed in core components and steam generators during both normal and off-normal operation conditions. In boiling water reactors (BWRs), such flow is encountered in the core during normal operation. Thus, the proper understanding of the two-phase flow plays an important role in the operation, safety, and cost (Berna et al., 2014). The importance of liquid–gas two-phase flow in industrial fields is evidenced by the extensive research conducted on liquid–gas two-phase flow and the amount of capital invested in the equipment that employs the characteristics of such flow support.

---

[*]Part of this chapter is reprinted with permission from "Experimental investigation of the annular flow caused by convective boiling in a heated annular channel" by J. Seo, S. Lee, S. R. Yang, Y. A. Hassan, 2021. Nuclear Engineering and Design, 376, Copyright 2021 by Elsevier.

Despite numerous studies that focus on liquid–gas two-phase flow, an accurate model that can cover a wide range of flow regimes including flow transitions is yet to be developed (Hewitt & Hall-Taylor, 1970). Such a model is lacking because of the occurrence of extremely complex phenomena in such flows and there being no approach that can obtain detailed information about physical parameters such as local mass flux, velocity, and density distributed across the domain of interest. Further, when the liquid–gas two-phase flow embraces the complexity of turbulence, a complete theoretical turbulence model is required to explain the complex form of flow at the interface between phases.

1.1 Annular Flow Boiling in a Heated Annular Channel

Meaningful progress can be achieved in the study of liquid–gas-two-phase flow by breaking down the flow into the smaller groups. Phases in a two-phase flow travel in several topological configurations called “flow regimes (or patterns)” characterized by the dynamic structures of the interface between phases (Julia & Hibiki, 2011). The introduction of flow regimes help achieve a significant improvement in the analysis of the two-phase flow because closure laws based on flow patterns were derived to describe the mass, momentum, and energy transfer at the interfaces (Levy, 1999). Enormous efforts were invested to achieve further progress in this direction; for example, the research focused on obtaining an accurate and clear understanding of the transition of flow patterns that can directly derive closure laws based on the analytical descriptions of flow patterns and on establishing physical models that can be derived from accurately

measured parameters and consider the effects of various geometries and boundary conditions in the research field.

This study focuses on an annular flow regime among those that can be observed in the vertical upward liquid–gas two-phase flow. Annular flow is characterized by the existence of a continuous liquid film on the wall of the channel and a traveling gas passing the central core, which carries a varying amount of entrained liquid droplets (Levy, 1999). The two regions—the liquid film and the vapor core—are separated by the interface that approximates in shape to that of the channel (Hewitt & Hall-Taylor, 1970). Annular flow can be observed in a wide range of engineering applications such as in evaporators and condensers of conventional power plants and in most steam-water systems operating under high pressure. Further, such flows can be encountered in PWR during a loss of coolant accident (LOCA) and in the normal operation of BWR. Therefore, the results of a high-fidelity analysis on the annular flow can help properly address the design, operation, and safety-related concerns of the nuclear reactor.

However, it is difficult to analyze annular flow because there are a large number of dynamic forces that need to be considered (Levy, 1999); this difficulty dramatically increases when the phase change at the walls is considered. From an engineering viewpoint, the momentum and energy conservation equation can be greatly simplified by introducing assumptions, such as (1) the two phases flow separately in the channel, (2) density within each region remains the same, and (3) the wall shear stress is constant (Hewitt & Hall-Taylor, 1970), to model the annular flow. The modeling of annular flow affords confidence in the prediction of important design parameters such as void fraction

and pressure drop. These system parameters highly depend on the local momentum and heat transfer of the two-phase flow. Therefore, the experimental measurements of local parameters such as the thickness and velocity of the liquid film, size and velocity of droplets and bubbles, and wave characteristics are necessary. Although a considerable number of measurements of such parameters are already made with bare circular tube geometry and applied to models employed to system codes (RELAP5 3D), there are only a few studies that considered annulus geometry. Furthermore, the number of studies decreases significantly when only considering non-isothermal one-component (water & steam) two-phase boiling flow, which is the main motivation of the present work. When the actual operation of the nuclear reactor is considered, the one-component two-phase boiling flow in a annuli channel better simulates phenomena that occurs inside of a subchannel than the two-component (water & air) flow in a bare tube.

An experimental facility for annular flow in annuli is designed, constructed, and operated in the present study. The liquid film thickness, wave characteristics, and behavior of droplets and bubbles need to be measured to provide a validation set of data. Since studies on the measurement techniques for annular flow in the bare circular tube have already been performed (Alekseenko et al., 2008; Berna et al., 2014; Hazuku et al., 2008; Schubring et al., 2010), similar techniques are adopted in this study. Laser-induced fluorescence (LIF) and confocal chromatic sensor (CCS) systems are utilized to measure the liquid film thickness in the annular flow condition, whereas a shadowgraph is applied to observe the behavior of the droplets. The visualization techniques introduced in the previous study are enhanced to cover the increased complexity of the

geometry and the thermal hydraulic phenomena. Further, novel methods are developed to measure and analyze parameters successfully. The liquid film on the tube wall and the droplet dynamics are analyzed by utilizing the data obtained through the present study, and the results are compared with those obtained in former studies.

1.2 Literature Survey

A literature survey was conducted to facilitate an understanding of the physics of the annular flow boiling in annuli, and to gather ideas on existing measurement techniques. Research related to general flow characteristics and modeling of the annular flow are excluded in this step the research topics are extremely diverse and the total number of works is considerable large. Therefore, research on the annular flow in annuli and measurement techniques applied on the annular flow are introduced by narrowing the scope.

1.2.1 Studies on Flow Regimes

One of the earliest works were performed by Kelessidis and Dukler (1989). They investigated flow patterns in vertical upward gas–liquid flow in a concentric and eccentric annulus (eccentricity 50%). A new method for flow pattern identification was proposed based on the probability density function analysis of the conductance probe signals. Flow pattern maps were constructed and mathematical models that could predict the flow pattern transitions were proposed.

Julia et al. (2011) comprehensively summarized the flow regime in a vertical annulus. They collected previous researches on the flow regime maps in the annuli (Furukawa & Sekoguchi, 1986; Jeong et al., 2008; Julia et al., 2009; Kelessidis & Dukler, 1989; Sadatomi et al., 1982; Sun et al., 2004). Annular flow is steadily achieved when superficial gas velocity is greater than 20 m/s and the superficial liquid velocity is less than 0.6 m/s. The result indicates that the test facility does not require a high flow rate pump for liquid flow; however, the heat power needs to be controlled to produce a sufficient amount of vapor while it does not reach the heat flux that can cause damage on a heated rod.

Hernandez et al. (2011) conducted an experimental study on flow regime identification in boiling two-phase flow in a vertical annulus. They used the same facility dimensions as those listed in Table 1.1 with superficial liquid velocities from 0.23 m/s to 2.5 m/s, superficial gas velocities from 0.002 m/s to 1.7 m/s, and heat flux from 55 kW/m^2 to 247 kW/m^2.

1.2.2 Studies on Void Fraction

Void fraction has attracted a major interest in research related to two-phase flows for several decades (Jeong et al., 2008) because of the dependency of the amount of heat transfer that flows through the two-phase flow on the void fraction. Furthermore, the pressure drop in the two-phase flow is correlated with a void fraction, and this can be predicted by many models such as the drift-flux (Zuber & Findlay, 1965) and two-fluid models (Ishii, 1975).

Most common methods adopted to measure the void fraction include double-sensor (Bartel et al., 2001; Bruder et al., 2018; Lee et al., 2002; Situ et al., 2004; Yun et al., 2010) and four-sensor probes (Bottini et al., 2020; Ooi et al., 2019; Ozar et al., 2013). Most recently, Bottini et al. (2020) reported the void fraction data in an internally heated vertical annulus facility with a heated length of 3.0 m and an inner diameter of 19.05 mm using four-sensor probes.

1.2.3 Studies on Droplet Deposition and Entrainments

Droplet deposition and entrainment are key mechanisms of liquid mass transfer between the liquid film and vapor core in the annular flow. Recently, Zhang and Hewitt (Zhang & Hewitt, 2017) proposed new models of droplet deposition and entrainment for CHF in annular flow in the annuli. Anglart (2014) presented an analysis of the entrainment rate in annuli and found that the standard droplet deposition and entrainment correlations derived from tube data are not appropriate for flows in annuli. Therefore, Zhang and Hewitt (Zhang & Hewitt, 2017) developed a set of simple and easy-to-implement models for deposition and entrainment rates in annuli based on the tube-based Hewitt-Govan correlations (Hewitt & Govan, 1990) and consideration of the liquid film flow characteristics in annuli and the geometry effect of the annulus. However, CHF prediction models require an initial condition for the fraction of the liquid phase entrained at the onset of annular flow and the distribution of the remaining liquid (film) between the inner and outer surfaces. Zhang and Hewitt (Zhang & Hewitt, 2017) assumed that the remaining liquid was distributed at the onset of annular flow

such that the film flow per unit periphery was equal on the inner and outer surfaces because there is a lack of experimental information of the liquid film thickness difference between the inner and outer surfaces.

The mechanism of entrainment is intensively studied owing to its importance in modeling. Although they have been clearly observed and analyzed for various geometries, to the best of the authors' knowledge, the mechanisms of entrainment are yet to be thoroughly investigated in the case of flow boiling in annuli. From this viewpoint, works clarifying the mechanisms of droplet entrainment that exists in the flow boiling in annuli would be a meaningful and interesting subject.

1.2.4 Studies on the Measurement of Liquid Film

The measurement of the liquid film thickness is a major target parameter in this study. There are several research studies on the measurement of liquid film thickness in circular tubes, as indicated in Table 1. However, there are a limited number of liquid film measurements in annulus such as those performed by Ueda and Suzuki (1978) and Nakoryakov et al. (1992). In addition, there is a lack of experimental data to study different behaviors of the liquid film in annular flow between concentric and eccentric geometries.

Table 1. Experimental researches on liquid film thickness measurement.

Author (Year)	Measurement Methodology
Okawa et al. (2010)	Laser Focus Displacement (LFD) meter
Hazuku et al. (2008)	LFD (Keyence LT 8100)
Schubring et al. (2010)	LIF
Alekseenko et al. (2008, 2012, 2014, 2015)	LIF & PIV
Zadrazil et al. (2014)	LIF, PIV, & PTV
Hall Taylor et al. (1963)	Conductance probe
Belt et al. (2010)	Conductance probe
Zhao et al. (2013)	Conductance probe
Dasgupta et al. (2017)	Conductance probe
Damsohn and Prasser (2009)	Conductance screen 2D
Hall Taylor et al. (1963)	Photograph
Nedderman & Shearer (1963)	Photograph
Azzopardi (1986)	Photograph
Pham et al. (2014)	Photograph
Dasgupta et al. (2017)	Photograph
Zboray & Prasser (2013)	Neutron Image

In this work, high-speed camera methods and laser displacement sensor systems are employed to measure the liquid film in annular boiling. Thus, several relatively recent works on the liquid film thickness measurement are summarized here. Alekseenko et al. (2008, 2014) conducted experiments using LIF with a Plexiglas cylindrical channel, as shown in Figure 1. In this work, the flow regimes characterized by the presence of disturbance waves and liquid entrainment were investigated.

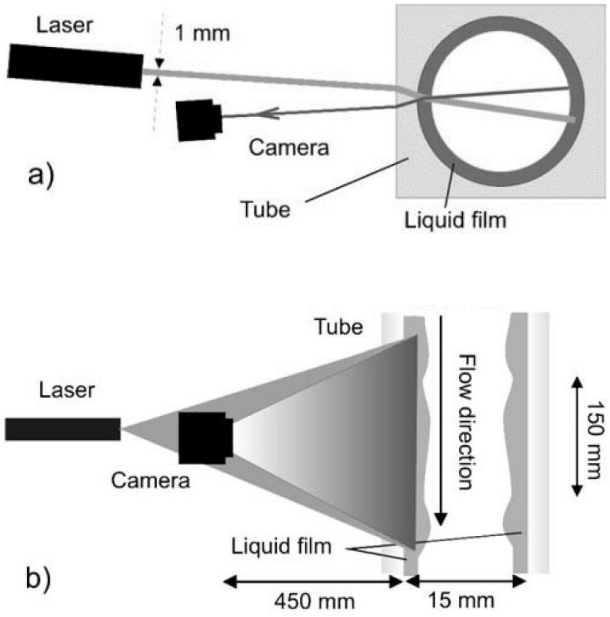

Figure 1. Scheme of experiment: (a) top view and (b) side view [Alekseenko et al. (2008)]

Schubring et al. (2010) used LIF to provide the direct visualization of the liquid film in an upward vertical air–water annular flow. The refractive index matching technique was used with the combination of FEP and water as shown in Figure 2. They produced the data of the distribution of film heights. The standard deviation and average film thickness tend to be an increasing function of liquid flow and a decreasing function of gas flow, with the standard deviation approaching 0.4 times the average at sufficient liquid flow.

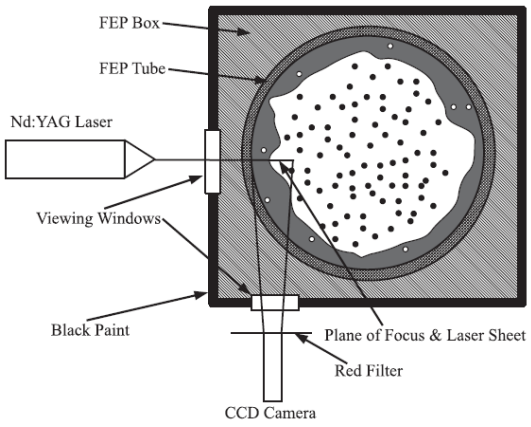

Figure 2. Test section for PLIF measurement [Schubring et al. (2010)]

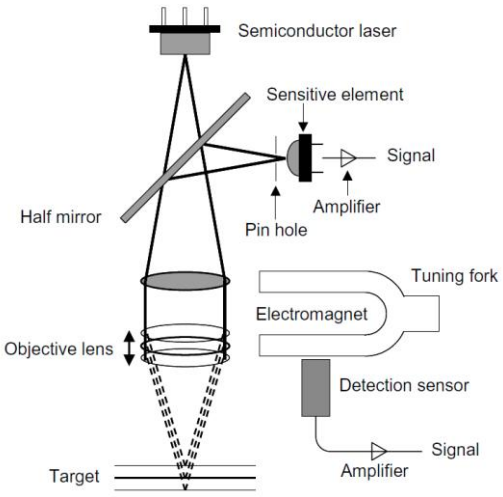

Figure 3. Principle of laser focus displacement meter [Hazuku et al. (2008)]

Hazuku et al. (2008) used a laser focus displacement (LFD) meter to measure the liquid film thickness in annular flow as shown in Figure 3. They obtained local properties such as the minimum thickness, maximum thickness, and passing frequency of the waves, and they proposed a correlation between the minimum film thickness obtained in relation to the interfacial shear stress and the Reynolds number of the liquid.

1.2.5 Studies on Phase Change Simulation

For a few decades, a number of computational schemes have been suggested to model the two-phase flow and interfacial interactions (Samkhaniani & Ansari, 2012). From the simplest homogeneous model to multifluid (two/three equation) models, many models have been suggested and selected based on their advantages and characteristics. Since two-phase flow comprises a wide range of phenomena that can be classified as the flow regime, a numerical scheme and model needs to be carefully selected based on the consideration of the phenomena. Among them, the combination of interface resolving method and single fluid formulism is extensively applied to simulate a two-phase flow with dominant interfacial flow (Angeli & Gavriilidis, 2008; Wörner, 2012). In this method, a single set of conservation equations is solved regardless of the phase distribution. Surface tension is added to the momentum conservation equation as a source term to explain the behavior of the two-phase flow. Although the method solves a single set of equations, it can capture the interface by adopting an interface resolving method. There have been intensive studies on interface resolving methods, and the three most common interface resolving methods include volume of fluid (VOF) (Brackbill et al., 1992), level set (LS) (Sussman, 1994), and front tracking (FT) (Unverdi & Tryggvason, 1992). Similar to two-phase models, interface resolving methods have their own advantages and should be selected considering the characteristics of the phenomena. Among them, the VOF method is known to conserve mass better than LS and FT while it has higher error in the interface curvature and normal vector calculation (Samkhaniani & Ansari, 2012).

The VOF method can be classified by how it reconstructs the interface captured from the calculation. A large number of studies have investigated this research topic and many methods have been suggested by various research groups: simple line interface calculation (SLIC) (Yokoi, 2007) reconstructs the interface as a set of horizontal or vertical segments, and piecewise linear interface construction (PLIC) (Youngs, 1982) uses segments which are not limited to horizontal or vertical directions. To overcome the disadvantage of using VOF, the PLIC algorithm is adopted in this study. Other than the SLIC and PLIC, there are many reconstructing methods such as the parabolic reconstruction of surface tension (Renardy & Renardy, 2002), and compressive interface capturing scheme for arbitrary meshes (Ubbink & Issa, 1999). However, owing to the limitation of implementing the OpenFOAM environment, only PLIC is used in this study.

1.3 Objective of Study

There are several studies on annular flow in circular channels and annuli. However, limited experimental data exist in annular boiling conditions in annulus geometries, which is the main motivation for the current work. Thus, the objective of this study is to generate high-fidelity experimental data of the liquid flow and the behavior of droplets in annular flow to provide validation data for computational fluid dynamics (CFD) code. The objective includes the following measurement targets.

- Thickness of the liquid film on the tube wall of the annulus
- Amplitude and velocity of disturbance waves

- Size and velocity of liquid droplets and bubbles
- Pressure drops

According to the former studies, LIF and CCS systems are utilized for the measurement. LIF will be used to measure the liquid film thickness on the tube wall, and a point-wise high-sampling-rate optical sensor called a CCS will be used to measure the liquid film thickness in multiple locations. A shadowgraph will be used to investigate droplet size, velocity, population, deposition, and entrainment. The measurement of these parameters is highly challenging and only limited number of studies have been made on such geometry and boundary conditions. This study aims to measure and analyze the parameters successfully by developing novel methods.

The data and analysis obtained in the present study can help develop an annular flow boiling model in CFD. Among the various targeted models, this study focuses on investigating and validating phase change models based on the VOF method. The film flow will be simulated using OpenFOAM. The film dynamics and thickness calculated by the simulation will be compared with the experimental result to find the value for the constant of the phase change model.

CHAPTER II

EXPERIMENTAL SETUP[*]

The importance of this study lays on the fact that there are only a limited number of data related to the annular flow caused by boiling in the annulus geometry although they are highly required as a validation set for the CFD simulation of two-phase flows occurring inside nuclear reactors. To provide these data, an experimental setup is designed to investigate the detailed information of the annular flow occurring in concentric and eccentric annuli with a central heating rod in an unheated tube.

2.1 Overview of experimental setup

Figure 4 and Figure 5 present the schematics of the experimental facility. The experimental facility comprises a temperature controllable flow loop, an annular test section with a heating rod, a laser and camera system, and other instruments. The experimental facility was designed considering 3M Novec-7000 refrigerant usage. Novec-7000 (R-347mcc or methyl perfluoropropyl ether, or HFE-7000) has a boiling point of 34.0 °C and its latent heat of vaporization is 133.86 kJ/kg under atmosphere pressure (0.1 MPa). The parametric details of the refrigerant are summarized in Table 2. The length and diameter of the heating rod are 3 m and 0.95 cm, respectively; the

[*] Part of this chapter is reprinted with permission from "Experimental investigation of the annular flow caused by convective boiling in a heated annular channel" by J. Seo, S. Lee, S. R. Yang, Y. A. Hassan, 2021. Nuclear Engineering and Design, 376, Copyright 2021 by Elsevier.

distance between the inlet and outlet of the vertical section is 2.5 m. The test section is made of borosilicate glass for flow visualization. The laser and high-speed camera systems are mounted surrounding the test section to capture images of the liquid film. The details of the test section and heating rod are presented in the next section. The experimental facility can provide both subcooled and saturated liquid flow conditions at the inlet of the test section and annular boiling regime in the annulus. The heat exchangers are equipped with a temperature controller and chiller to provide temperature-controlled liquid flow and the capability to condense the vapor produced during boiling. The heating rod initiates boiling and eventually achieves annular flow.

Table 2. Properties of methyl perfluoropropyl ether (Novec-7000, HFE-7000) under atmosphere pressure.

Parameters	Value	Unit
Boiling Point	34.0	°C
Freeze Point	-122.5	°C
Liquid Density	1379.3	kg/m^3
Gas Density	7.94	kg/m^3
Kinematic Viscosity	0.32	mm^2/s
Latent Heat of Vaporization	133.86	kJ/kg
Specific Heat	1.24	$kJ/kg{\cdot}K$
Surface Tension	12.40 E-03	N/m
Liquid Prandtl Number	7.36	-
Gas Prandtl Number	0.893	-
Thermal Conductivity	0.075	W/K
Critical Pressure	2.48	MPa
Critical Temperature	165.0	°C
Critical Density	553.0	kg/m^3

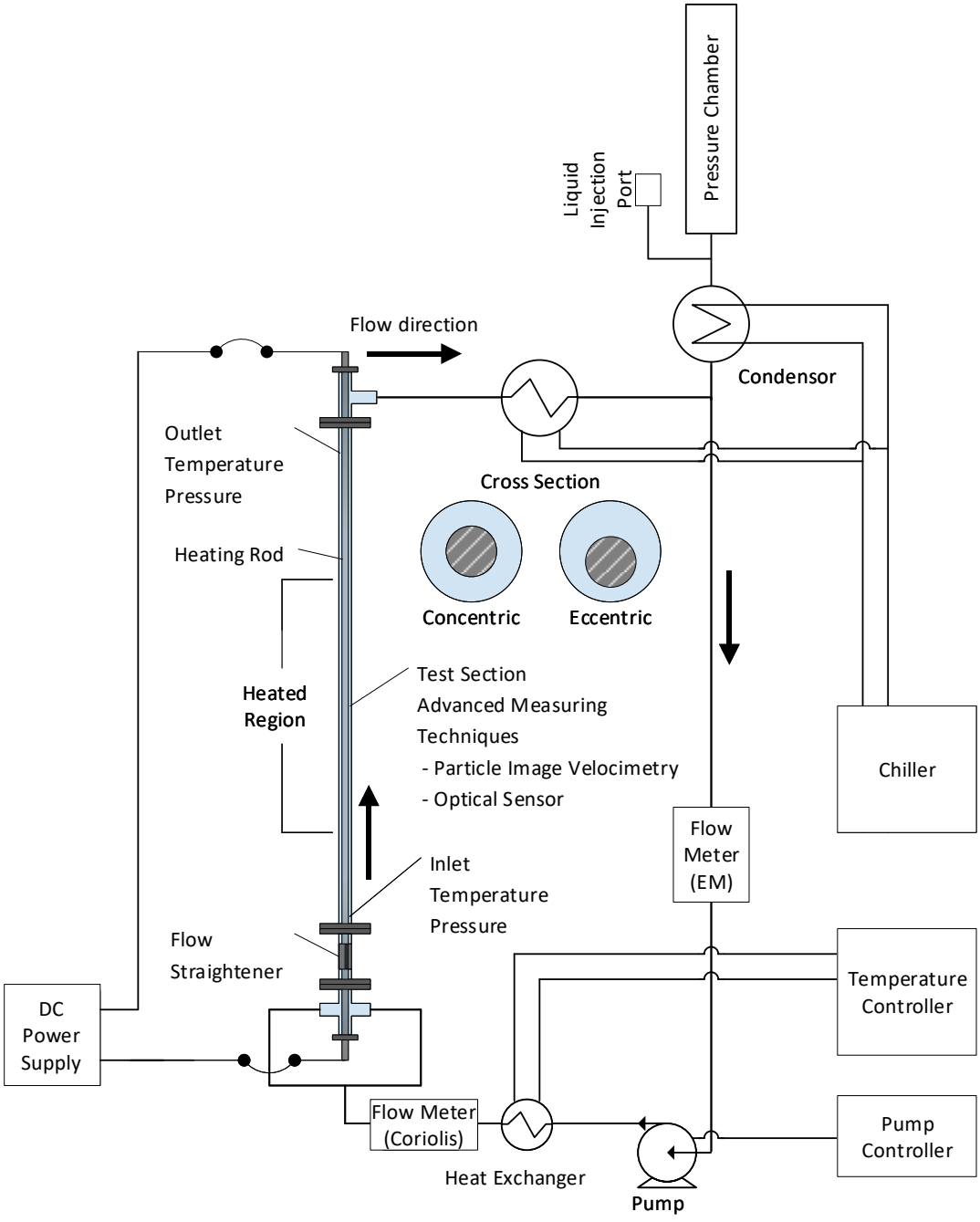

Figure 4. Schematics and picture of the experimental facility.

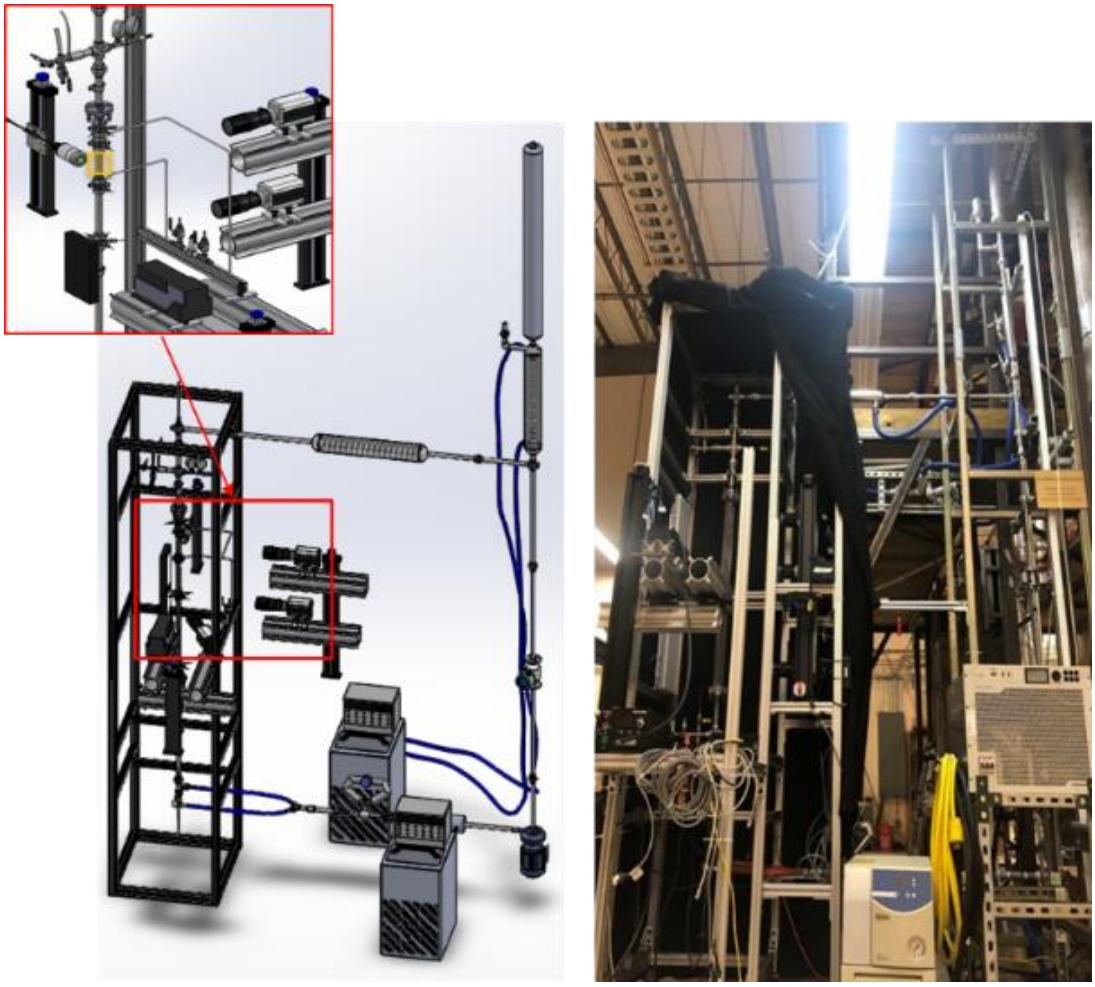

Figure 5. Picture of the experimental facility.

The flow is controlled and monitored using a DC pump with a digital-voltage controller and a Coriolis flowmeter with an accuracy of ± 0.25%. The inlet temperature of the test section, where the heated region of the heating rod begins, is controlled by a temperature controller (Thermo-Scientific MERLIN-M33) connected to a heat exchanger. Three shell- and tube-type heat exchangers are installed in the loop. One is located upstream of the inlet and connected to the temperature controller for maintaining the inlet temperature of the fluid at 33 °C. This is 1 °C below the saturation temperature

of the refrigerant under atmospheric pressure. The other two heat exchangers are located upstream of the pump and are connected to a chiller. The vapor generated during boiling is condensed to the liquid phase inside these two heat exchangers. Two K-type thermocouples (one each at the inlet and outlet) are used to monitor the temperature of the test section. Four thermocouples are embedded in the heating rod: two at the beginning of the heated region, and the other two at the end of the heated region. The thermocouples are connected to the DAQ system. Table 3 and Table 4 present the list of instruments and equipment, respectively.

Table 3. List of instruments.

Instrument	Model	Range	Accuracy
Coriolis Flow Meter	Elite CMF025M	Up to 66.7 g/s, < 204 °C	0.25%
CCS	KEYENCE CL-P015	15mm ± 1.3mm	± 0.49 μm, 1.0 %
Thermocouple	K-type	0 ~ 1250 °C	1.1 °C
Gauge Pressure Transducer	OMEGA MMG015V5P1D0T4A6	0 ~ 15 PSIG	0.03% B.S.L. 0.3% zero/span
Differential Pressure Transducer	OMEGA MMDWB005BIV5P3D0T1A3	± 5 PSID	0.08% B.S.L. 0.5% zero/span
Gauge Pressure Transducer	OMEGA MMDWB005BIV5P2D0T2A3	± 5 PSID	0.08% B.S.L. 0.5% zero/span

Table 4. List of equipment.

Equipment	Model	Range
Temperature Controller	Thermo-Science MERLIN-M33	-15° to +35°C Temperature Stability: ±0.1°C
Chiller	Marrone & Co. ACWC-060-QM	10 to 40 °C
DC Power Supply	TopCon Quadro	~30 VDC, ~500A (15 kW)
High-speed Camera	MIRO-M310	10k fps @ 640X480
High-speed Camera	PHANTOM-v711	7,530 fps @ 1280X800
Laser	CL-AO-L-532	10W

2.2 Test section

The test section comprises a transparent borosilicate glass tube (inner diameter (ID) = 20.6 mm and outer diameter (OD) = 25.5 mm) equipped with an electrically heated stainless-steel rod (diameter = 9.5 mm), as shown in Figure 6. The full length of the stainless-steel heating rod is approximately 3 m with a heated length of 1 m; the wall thickness of the heated region (stainless-steel tube) is 0.5 mm. One concentric and one eccentric annuli design are considered as illustrated in the middle of the figure. The hydraulic diameter of the present design (11.5 mm) closely matches the hydraulic diameter of a typical BWR (Todreas & Kazimi, 2011). The heated test section begins at a distance 60 times the hydraulic diameter away from the inlet of the measurement region to minimize the entrance effect. Two K-type thermocouples are installed upstream of the inlet and downstream of the outlet of the test section. Four K-type thermocouples are embedded in the heated rod to measure the surface temperature. Two of them are installed 13 mm away from the beginning of the heated region, while the other two are embedded 13 mm upstream at the end of the heated region. The outlet temperature is measured 470 mm away from the end of the heated region.

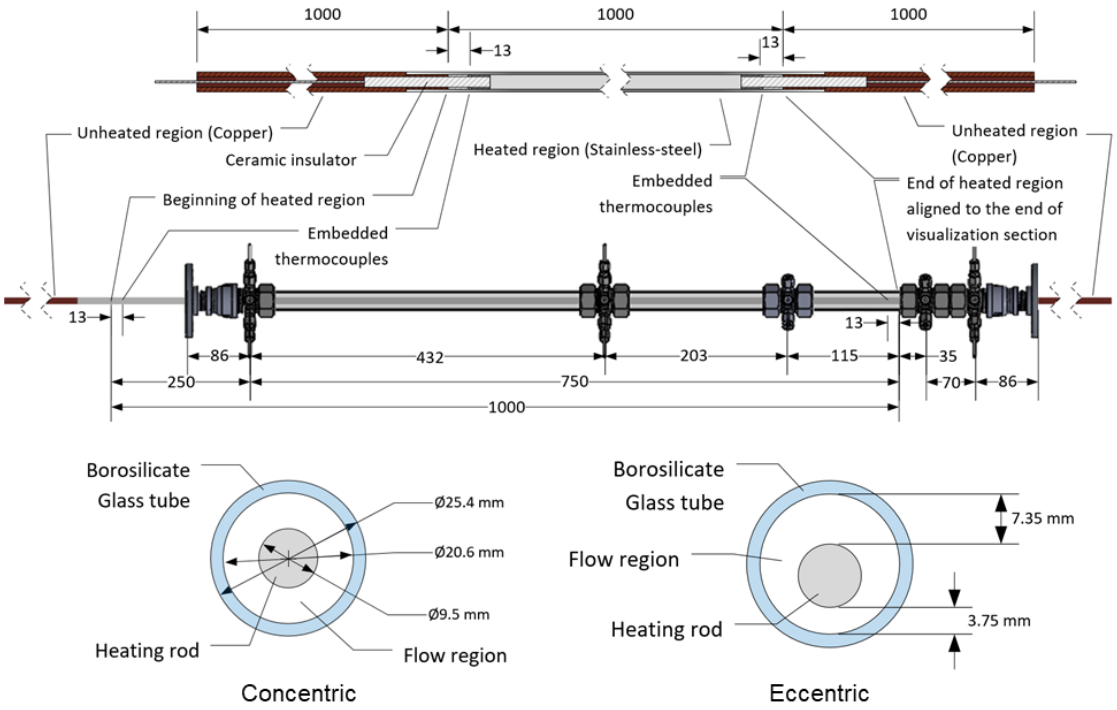

Figure 6. Schematics of the test section.

Figure 7 shows the picture of the measurement section (located 721mm above the inlet of the test section with a total length of 150 mm) at the moment of the actual experiment. Difference pressure (DP) measurement ports are located with a 150 mm distance covering the CCS and LIF measurement area. The CCS was installed to have laser focus at 42 mm upstream at the end of the heated region; the LIF was installed to cover the CCS measurement point. The 10 W continuous laser with a 532 nm of wavelength for the LIF and CCS are mounted on opposite sides.

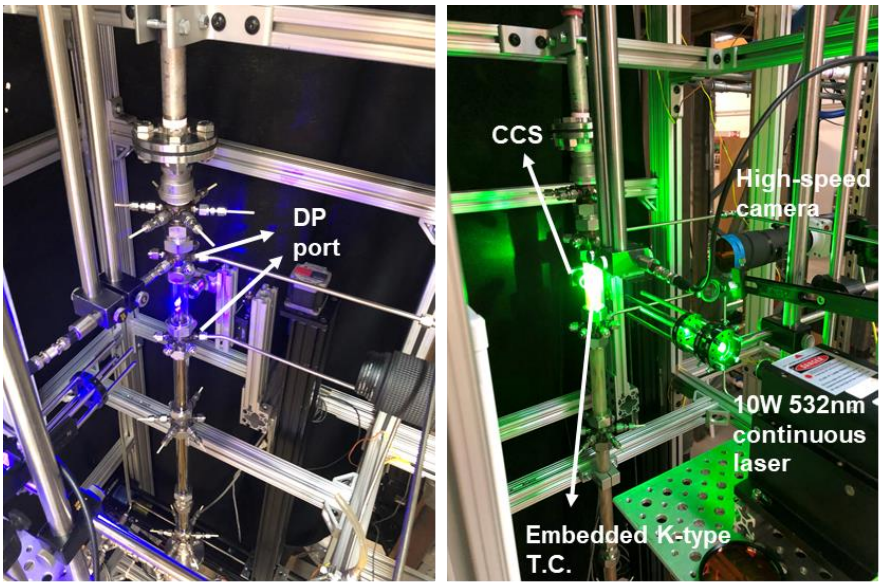

Figure 7. Orientation of the measurement section during the actual experiment.

2.3 Experimental conditions

Table 5 summarizes the experimental conditions applied in the present work. The boundary conditions of the experiment are controlled by adjusting the flow rate and heating power. The heating power of 2.0–4.0 kW corresponding to 67–134 kW/m^2 is applied to the heater. The superficial velocities at the outlet of the test section are calculated based on the equations of mass conservation for the system because it is not feasible to measure the superficial velocities of liquid and vapor in the test section where the annular flow occurs. The heating power is assumed to be fully transferred to the working fluid, which increases its temperature to the saturation temperature (34 °C) and alters its phase from liquid to vapor. The power input rate can be converted to the mass flow rate of the liquid and vapor at the outlet of the test section based on fluid properties such as specific and latent heat. The superficial velocities of each phase are calculated

from the mass flow rates, densities, and cross-sectional area of the channel. Experiments were conducted with the given conditions throughout three flow regimes: churn-to-annular-transition flow regime, annular flow with lumps regime, and annular flow regime (Figure 8). Although the experimental facility can covering regions with a higher superficial velocity of gas, the boiling test loop attained the dry out condition for the inner liquid film even near the border between the churn-to-annular flow regime and the annular flow regime. This is not considered in isothermal (or adiabatic) experiments.

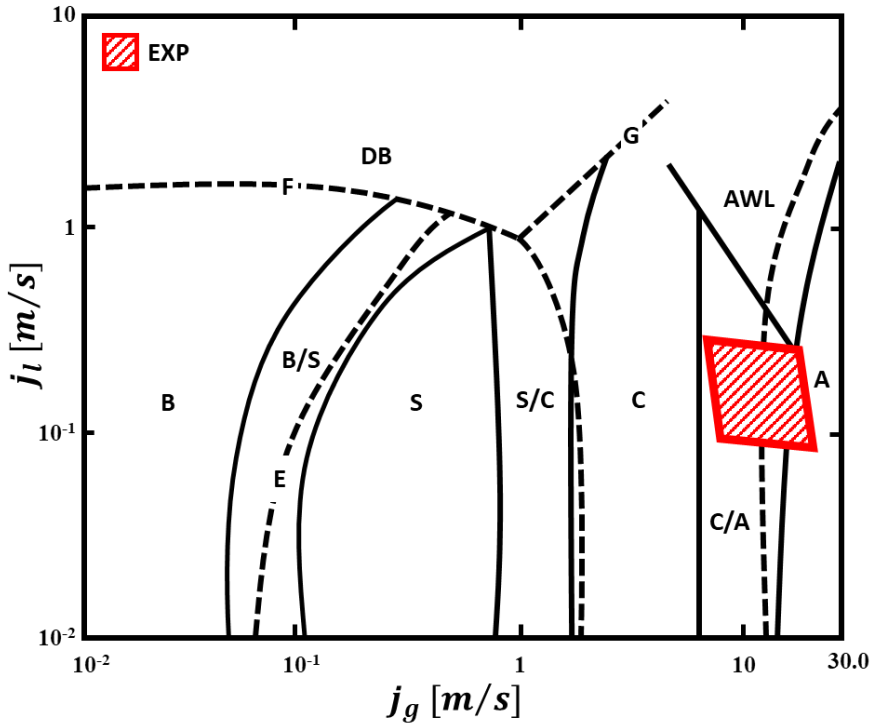

Figure 8. Experimental condition in the flow regime of annuli: Flow regime map (Kelessidis & Dukler, 1989) **and experimental condition, B: Bubble flow, DB: Dispersed-bubbly flow, B/S: Bubble to slug transition flow, S: Slug flow, S/C: Slug to churn transition flow, C: Churn flow, C/A: Churn to annular transition flow, AWL: Annular flow with lumps, A: Annular flow, Curve E:** $j_l = 3.0 j_g - \left[g\left(\rho_l - \rho_g\right)\sigma/\rho_l^2 \right]^{1/4}$ **, Curve F:** $j_l + j_g = 1.726 m/s$ **, and Curve G:** $j_l = 0.92 j_g - 0.08 m/s$ **.**

Table 5. Experimental conditions

Parameters	Values	Accuracy	Units
Mass flow rate	58–155	0.25%	*g/s*
volume flow rate	4.22×10^{-5}–1.13×10^{-4}	0.25%	m^3/s
Inlet Reynolds Number	6.29×10^{3}–1.68×10^{4}	0.25%	-
Inlet Peclet Number	4.63×10^{4}–1.24×10^{5}	0.25%	-
Power	2.0–4.0	0.05%	*kW*
Heat Flux	67–134	0.05%	kW/m^2
Superficial Velocity of Gas at outlet	6.12–13.26	0.05%	*m/s*
Superficial Velocity of Liquid at outlet	0.10–0.39	0.25%	*m/s*

CHAPTER III

MEASUREMENT METHOD*

Although measurement techniques utilized in this study are referred to in former studies, unique skills are required not only to produce the data but also to post-process the data for analysis.

3.1 Laser-induced fluorescence (LIF)

It is necessary to visualize a thin film to measure and analyze the liquid film in annuli using a planar field measurement technique and a thin laser sheet. In this study, LIF is adopted as the measurement method for a liquid film at the inner wall of the outer tube. This is a visualization technique that uses a fluorescent material, laser source, and camera, as shown on the left side of Figure 9. In the liquid film visualization system that uses LIF, the fluorescent material is dissolved in the working fluid, and a thin incident laser sheet is emitted on the fluid to excite the fluorescent material. Fluorescent materials have a distinctive absorption and emission spectrum, as shown on the right side of Figure 9. Once it absorbs the light from the laser, the fluorescent material emits light with constrained wavelengths. One can detect the region where the fluorescent materials are excited by the incident laser by filtering out the light with wavelengths other than the

* Part of this chapter is reprinted with permission from "Experimental investigation of the annular flow caused by convective boiling in a heated annular channel" by J. Seo, S. Lee, S. R. Yang, Y. A. Hassan, 2021. Nuclear Engineering and Design, 376, Copyright 2021 by Elsevier.

emitting spectrum of the fluorescent materials. This characteristic enables the measurement of the shape, boundary, density, and concentration of the fluid on a thin laser sheet.

In this study, Rhodamine-6G is used as the fluorescent material; it has an absorption peak near the wavelength of 530 nm, and an emitting range of 570–660 nm with the maximum at 590 nm. An aqueous solution is prepared by dissolving 1 g of Rhodamine-6G powder in 1 L of ethanol. Considering experimental conditions, 15 ml of the aqueous solution is mixed with 4 L of the working fluid; the concentration of Rhodamine-6G is 3.74 mg/l. A high-speed camera is mounted on the vertical frame, and a continuous laser (532 nm, 10 W) is mounted at the position perpendicular to the camera. A band-pass filter centered in 580 ± 20 nm is installed in front of the camera lens.

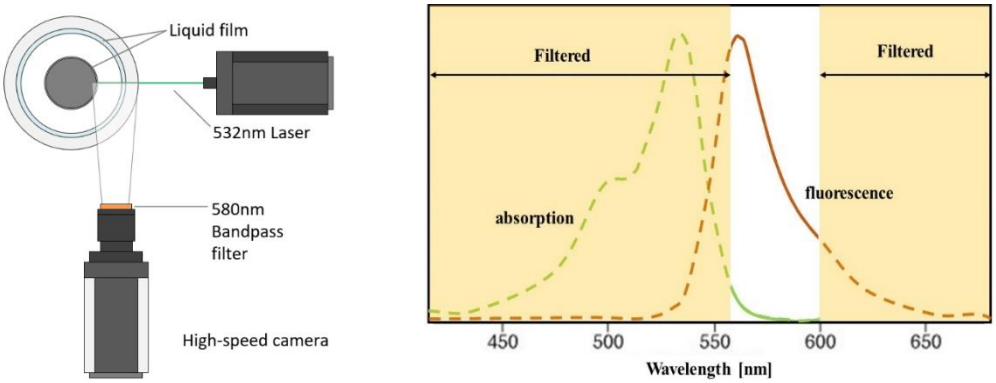

Figure 9. LIF setup (left) and spectral characteristics (right)

The image processing results of the LIF data are presented in Figure 10. The gray-scale images captured using the LIF system are transformed into binary images via image processing. The boundary of the liquid film can be clearly identified in the binary image.

The thickness can be obtained by counting the number of pixels between this boundary and the wall. Then, the pixel to millimeter conversion factor is applied, and finally, the actual thickness is calculated by multiplying the corrected conversion factor with the film thickness.

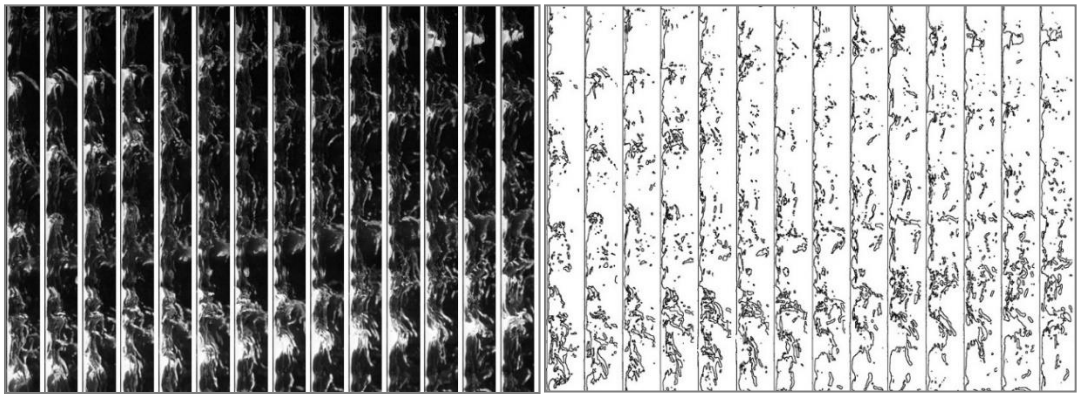

Figure 10. Sequential LIF images (left) and Processed images (right)

3.2 Shadowgraph

In this study, a first-order shadowgraph is adopted to visualize the droplets and bubbles moving inside the annular. Three cameras were mounted along the vertical frame to capture overall phenomena from the onset of flow boiling to annular flow. Two LED backlight panels with 18000 lumens of light intensity were positioned on opposite sides of the high-speed cameras. The frame rate of the camera was set as 20,000 fps with a resolution of 608 × 152. The exposure rate of each frame was 14.13 μs and the trigger for all cameras was controlled via an external pulse. Since a white backlight was used as the light source, no filter was used for the shadowgraph. A polarized film and filter were not used in the present study to maximize the amount of light intensity captured by camera sensor. A lens with a 200 mm of focal length was used with aperture size of f/22

considering the size of the image and the depth of focus. The parameters of interest in the study of droplets and bubbles include velocity, size (diameter), entrainment, and deposition.

Figure 11 shows a series of snapshot captured by the shadowgraph. Since pictures were captured in a temporal sequence with a 16.67 μs interval, the time can be calculated based on the number of pictures. Although there exists a severe distortion in the distance information in the radial direction, no distortion is observed along the stream wise direction because of the characteristics of the geometry. Thus, reliable information regarding the displacement of bubbles and droplets can be obtained by counting the number of pictures. The velocity can be calculated by simply counting pictures and pixels. The bubbles and droplets are sorted based on the axial (or stream wise) velocity of the object. Since a bubble travels inside the liquid film, it is considerably slower than droplet traveling inside the vapor core.

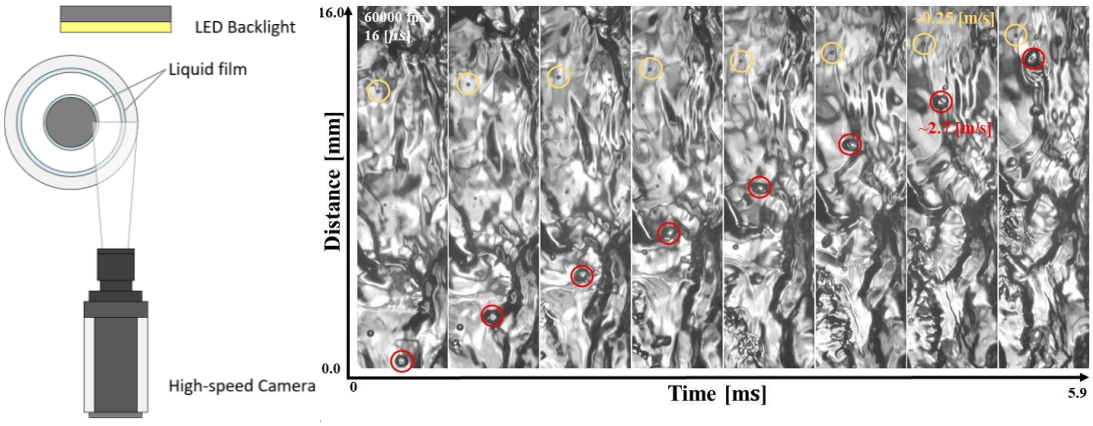

Figure 11. Shadowgraph setup (left) and Trajectories of a bubble (orange circle) and a droplet (red circle) measured by Shadowgraph (right)

3.3 Particle Image Velocimetry (PIV)

Although, the inlet velocity profile may not be very important for CFD simulations in the present work because of the significant boiling effect through the entrance region of the test section, particle image velocimetry (PIV) is used to provide a reasonable estimation for the inlet velocity profile. Before performing the PIV measurement, the velocity profile is assumed to be close to the fully developed profile because the inlet of the test section is more than 30 hydraulic-diameters away from the inlet of the vertical section of the loop. One benefit of performing the PIV measurement is that the turbulence intensity can be reasonably estimated for CFD simulations. The PIV system comprises a high-speed camera (M310, Phantom) and a laser (10 W, 532 nm) with optical lenses as shown in Figure 4.6; the frame rate is 5,000 frames/s (fps), and the exposure time is 200 μs. The trace particle is a hollow glass particles with an average size of 10 μm diameter and a density of 1.02 g/cm^3. The size of the image is 768 pixel × 768 pixels with a magnification factor of 24 μm/pixel. The PIV image in Figure 4.6 shows an inlet flow rate of 35 g/s. Under the given condition, the Reynolds number is approximately 208000 and the particle Stokes number is less than 0.1. A multipath fast Fourier transform (FFT) cross-correlation was applied to the particle images with an interrogation window size and step size of 64 × 32 – 32 × 16 pixels. The final step size of 16 pixels and magnification factor of 24 μm/pixel provided the final spatial resolution of 384 μm.

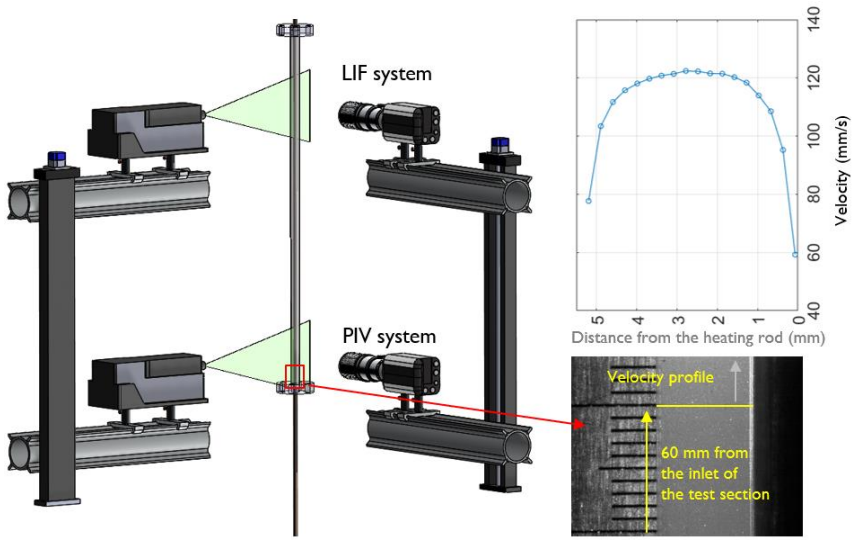

Figure 12. PIV setup and inlet velocity profile measurement

A filter with 7 standard deviations and a median filter with a threshold value of 5 and a minimum normalization level of 0.1 were applied for local post processing. The velocity profile in Figure 12 was captured along the yellow line in the PIV image, which is half of the concentric annular geometry. The current radius ratio *a* is 0.461. The PIV result and fully developed velocity profiles in Figure 13 show that a fully developed velocity profile is more reasonable than a uniform profile or an analytic solution of laminar flow for the CFD simulations when comparing the simulation results with the experimental data of the present work.

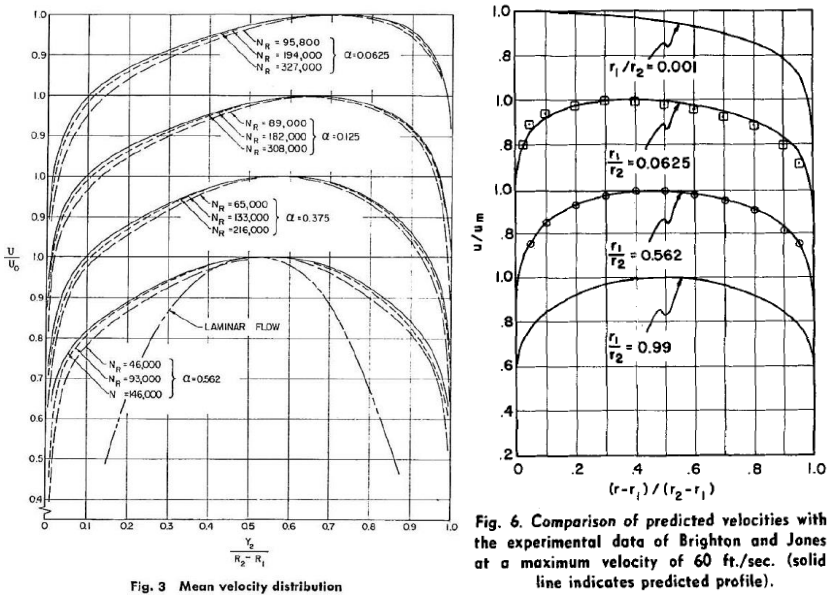

Fig. 3 Mean velocity distribution

Fig. 6. Comparison of predicted velocities with the experimental data of Brighton and Jones at a maximum velocity of 60 ft./sec. (solid line indicates predicted profile).

Figure 13. Fully developed turbulent flow velocity profile in concentric annuli by Brighton and Jones (Brighton & Jones, 1964) **(left) and Clump and Kwasnoski** (Clump & Kwasnoski, 1968) **(right)**

3.4 Confocal chromatic sensor (CCS)

A CCS is a sensing technique that can measure the distances of multiple surfaces through transparent materials using the chromatic aberration optical technique. A CCS system comprises a light source, lens, pinhole, and spectrometer. The light emitted by a polychromatic light-emitting diode (LED) travels through the optical fiber and reaches the lens. The lens is designed to produce a chromatic aberration, which causes lights of different wavelengths to possess varying focal lengths. Therefore, the wavelength of the light reflected at a surface can be an indicator of the distance between the lens and surface. A pinhole is installed at the front of the spectrometer to filter out the unfocused light with different wavelengths from the focused one because unfocused light can also be reflected from the surface.

One benefit of using CCS is that it can measure the thicknesses of multiple-layered objects if these are transparent. This characteristic enables users to perform a nonintrusive measurement of the thickness of a liquid film flowing inside the transparent tube. The system can be operated at a high sampling frequency (up to 10 kHz) with an accuracy of 1 μm. Further, it is free from electrical noise.

Figure 14 shows an example of the data collected by the CCS system. The refractive-index adjustment feature in the CCS software is used to perform measurement considering the reflective indices of Novec-7000 and borosilicate glass. The sensor has an internal modification function for multiple refractive indices up to four layers; users can customize the value of refractive indices using the program provided. The thickness of the base film was measured with a sampling frequency of 2,000 Hz. There are two distinguishable groups of data: the base film thickness and maximum film thickness. The sensor does not return a value if the tilt angle of the surface is out of the measurable range. Further, it is difficult to measure the variation in the thickness of the waves using CCS because it has a surface with a large angle attributed to the shape of the film flow. The number of data is relatively small, and it appears to be challenging to capture the physics of the waves using these data. Meanwhile, CCS measures the base film thickness accurately because the surface of the base film is relatively flat and varies gradually. Therefore, in this study, CCS is used to measure the thickness of the base film. Assuming that the thicknesses of the base film and ripples on the film are smaller than 0.5 mm, the data within the range of 0–0.5 mm are used. The average data for the total

measurement time (10 s) are calculated, and these data are compared with the LIF results for cross-validation.

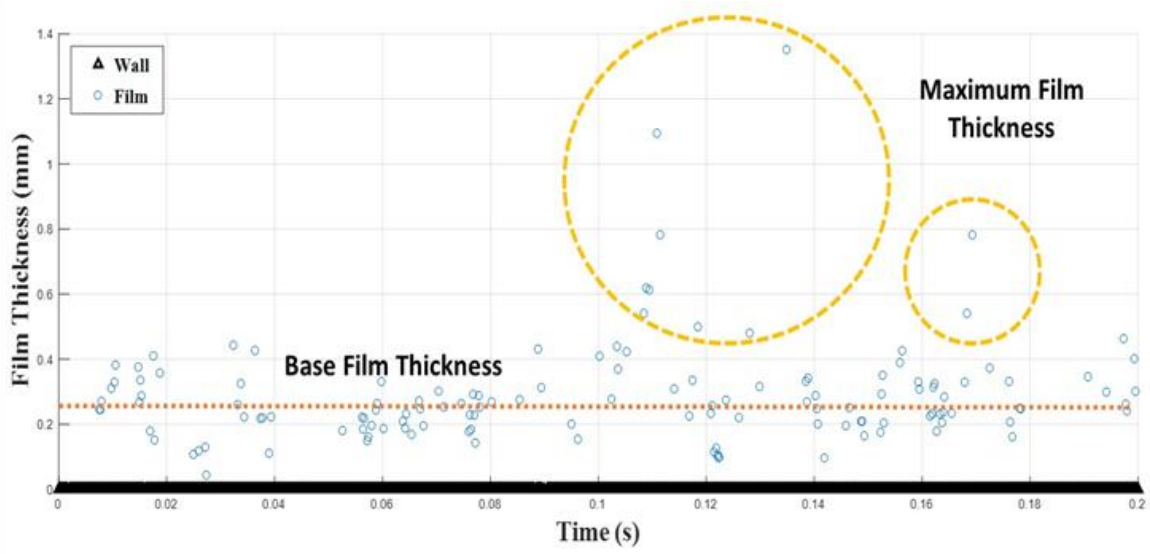

Figure 14. The example of the data collected by the CCS system

3.5 Measurement Uncertainty

In the visual observation of a fluid, a distortion caused by refraction can considerably affect the measurement accuracy. For cylindrical tube geometries, two concentric curved interfaces of the outer and inner walls cause a complex refraction of the light passing through them. Figure 15 shows the picture of the annular flow obtained from the shakedown test, wherein the wall of the glass tube cannot be recognized due to refraction. This indicates that the length information in the radial direction is severely distorted and cannot be accurately measured until it is physically or numerically modified. The image behind the observing plane can be captured by a camera owing to its geometrical characteristics. These problems raise the need for an LIF technique and the efforts to correct the effect of light refraction.

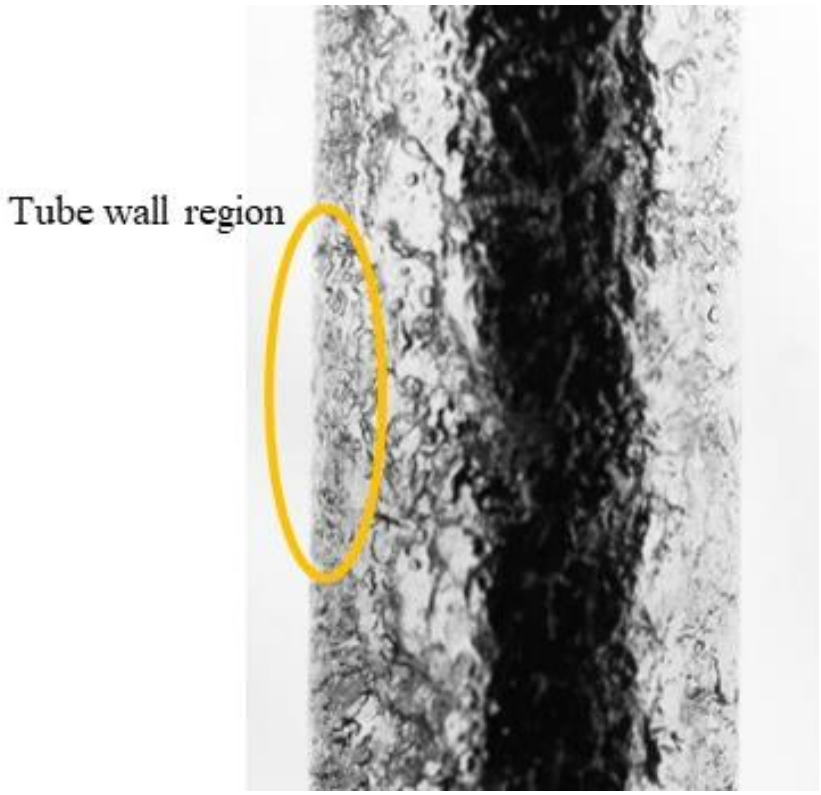

Figure 15. Optical measurement in cylindrical tubes: picture of the annular flow.

The combination of the borosilicate glass tube and Novec 7000 acts as a convex lens, as shown in Figure 16. Based on the ratio of the actual length to the measured length (or deformed length) presented in Figure 16, image correction factors are obtained as two functions of the radial location. The uncertainty of the correction factor is 1%, and the correction factor at 10.3 mm is obtained via linear extrapolation using the two previous values. The resulting uncertainty in the measured value is less than 10%; there was no deformation in the axial direction.

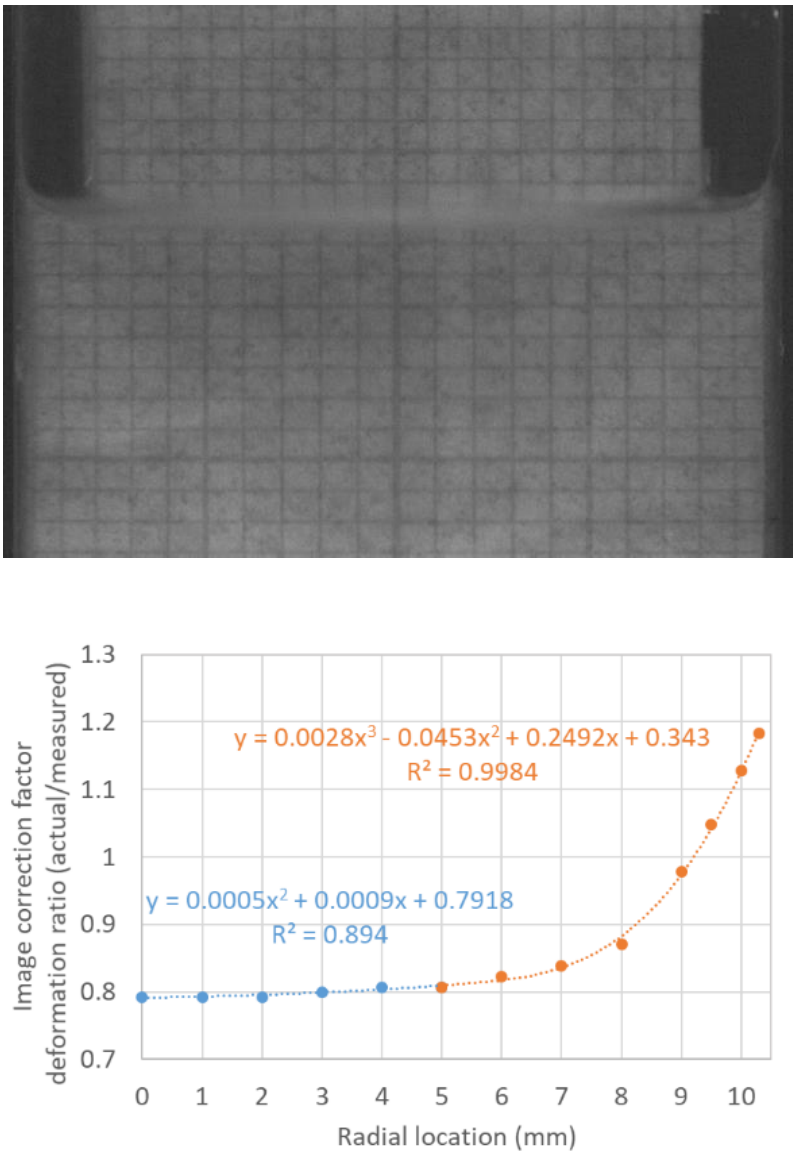

Figure 16. Image deformation in a glass tube and Novec 7000 (top) and Image correction factor (bottom)

The uncertainty of the CCS sensor was quantified from the simplified measurement setup. The spec of the sensor from the manufacturer presents an error less than 1 µm. However, in this study, the sensor measures the distance of the free surface between the liquid and gas. The reflection of the light at the free surface might cause

higher error than the case which the solid surface dominates the reflection. Thus, the uncertainty of the sensor was quantified in laboratory considering the characteristics of the measurement.

Figure 17 present the simplified measurement setup. A beaker with 1000 mL of capacity was located on the top of the sensor. The beaker was initially filled with water and the level of water was measured by the CCS. By adding 1mL of water into the beaker, the water level was increases step-by-step with 0.112 mm of interval. Then, the discrepancy of the actual value and the measured value were compared to check the error of the measurement. As a result, shown in the left side of the figure, the 10% of error bound could be obtained.

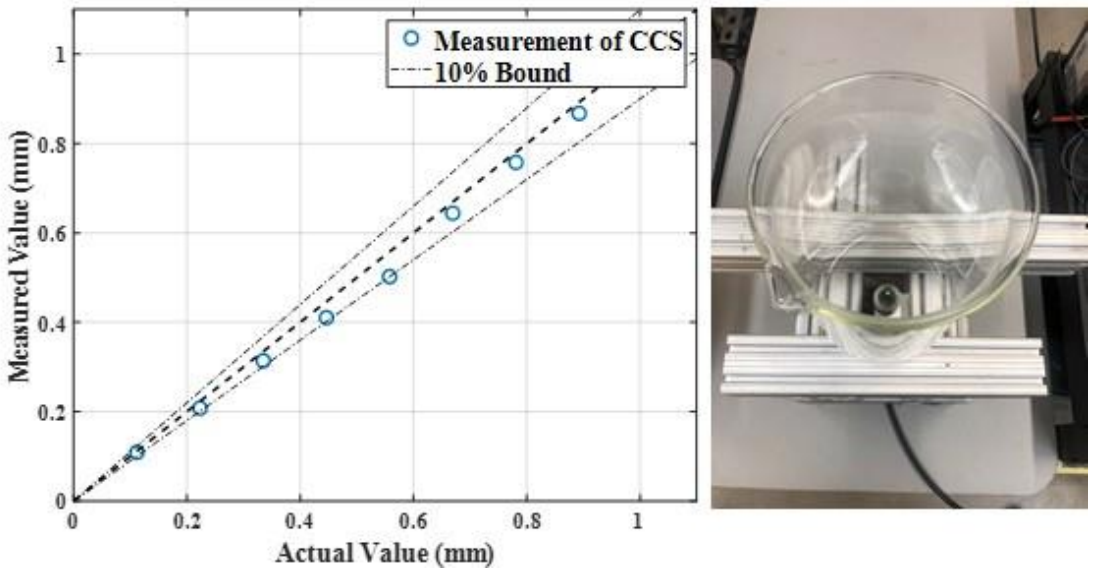

Figure 17. Uncertainty measurement of the CCS.

Uncertainty of the shadow graph for the size and velocity measurement of droplet and bubble was quantified using the similar approach with the LIF. The

schematic and the obtained image of the grid is shown in Figure 18. The aspect ratio of the square was used to calculate the maximum uncertainty of the measurement and it was concluded that the maximum error of the length measurement is 10.8%. The uncertainty was used as an indicator of the maximum error of the measured length from the image. Even though only the small area has such error and the most of the area has much smaller error than that, the error of the measurement was decided to be 10.8% conservatively.

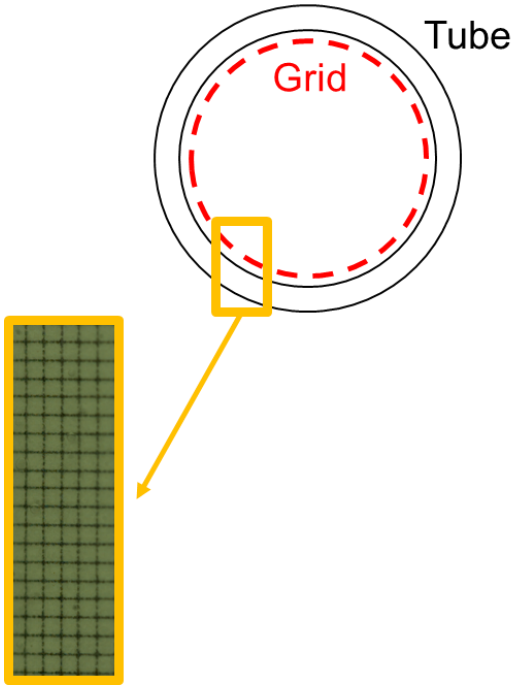

Figure 18. Uncertainty measurement using grid for the shadowgraph.

CHAPTER IV

EXPERIMENTAL RESULTS*

In this study, experiments were conducted for both concentric and eccentric annuli. The boundary conditions are defined in terms of the heat input and flow rate of the working fluid. Several sets of experiments were performed starting with a low heat flux (67 kW/m^3) and high mass flow rate of the fluid (58 g/s) until the boundary condition satisfied the onset of the dry out. Under the normal operation of the annular flow regime, a stable inlet temperature of 33 °C and other thermocouple readings were used as the initial condition for the measurement.

4.1. Film thickness

Snapshots of the sequential images of concentric case are presented in Figure 19. It is challenging to identify the boundary between the base film and waves traveling above it in the case with a high liquid superficial velocity, as shown in Figure 19 (a). Both base film thickness and amplitude of waves appear to decrease as the liquid superficial velocity decreases with the heat flux fixed at 83.75 kW/m^3 (2.5 kW) (Figure 19 (b)–(e)). Various interactions between vapor and liquid can be observed in these LIF images including entrainment mechanisms, droplet decomposition, generation and development of waves, and bubble flow inside the liquid film.

* Part of this chapter is reprinted with permission from "Experimental investigation of the annular flow caused by convective boiling in a heated annular channel" by J. Seo, S. Lee, S. R. Yang, Y. A. Hassan, 2021. Nuclear Engineering and Design, 376, Copyright 2021 by Elsevier.

(a)

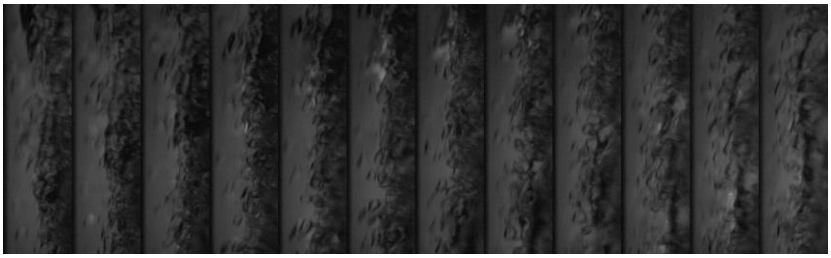

(b)

(c)

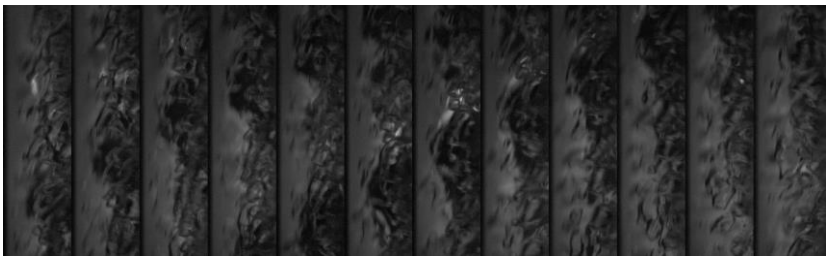

(d)

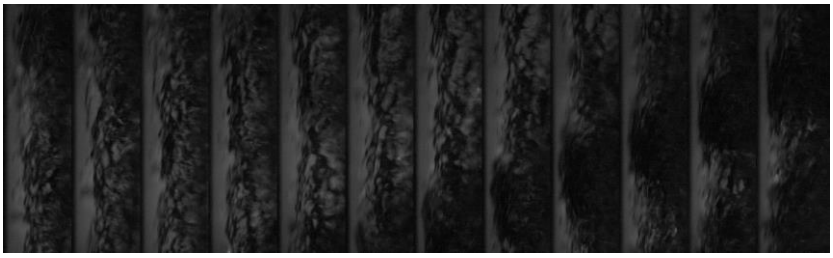

(e)

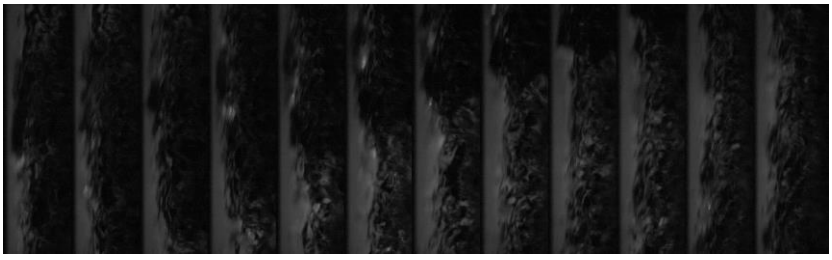

Figure 19. LIF image of concentric annular flow with heat flux of 83.75 kW/m3 and liquid superficial velocity of: (a) $j_i = 0.33$ m/s (b) $j_i = 0.28$ m/s (c) $j_i = 0.24$ m/s (d) $j_i = 0.18$ m/s (e) $j_i = 0.17$ m/s

Figure 20 presents the procedure for calculating the film thickness from LIF images. First, 20,000 images captured by the high-speed camera are added to obtain an averaged intensity field. The yellow line shows the trend of variation in the average intensity from the tube wall (on the left side) to the heater (on the right side). The peak light intensity is observed near the wall because of the abrupt decrease in the light intensity at the wall. The slope varies abruptly on the right side of this peak (in the red circle in Figure 20 (middle)), which is apparent in most of the test cases. Physically, this abrupt variation in intensity cannot occur when there is only one type of flow pattern along the axial direction. A disturbance wave flows on the base film in the case of annular flow (Alekseenko et al. (2008, 2012, 2014, and 2015)). Therefore, this point is likely to be the boundary of the base film and disturbance wave, as shown in Figure 20 (right).

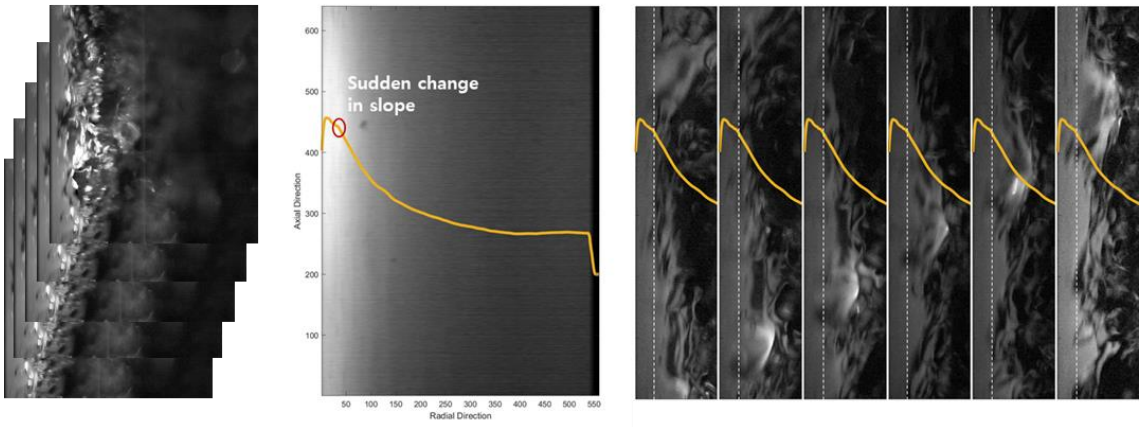

Figure 20. Intensity profile of accumulated images and consecutive images.

The values of film thickness obtained using CCS and LIF in the concentric geometry are listed in Table 6. There are relatively large errors in the first and sixth cases (i.e., 38.63% and 13.60%, respectively); these cases have boundary conditions with high

inlet liquid flow rates (G_{inlet} = 148.33 g/s and 135.0 g/s, respectively) and low heating powers (2.0 kW and 2.5 kW, respectively), which results in the churn to annular transition flow. In this flow regime, measurements performed using CCS capture only a limited amount of data because of its characteristics. Meanwhile, it is challenging to identify the boundary between the base film and disturbance wave from the average intensity field obtained by LIF. The CCS appears to perform reliable measurements when the churn flow is dominant, notwithstanding the uncertainty caused by the small number of data points. However, the LIF measurement provides a value larger than that for CCS in such a case because of the active mixing attributed to the significant error of the churn flow case. Besides these two cases, the two-measurement system shows good agreement with each other (Figure 21), and the points on the graph plotted between the results from the two measurement systems lie within the 10% error boundaries.

Table 6. Result of thickness measurement in the concentric case.

Power [kW]	G_{inlet} [g/s]	J_v [m/s]	J_l [m/s]	CCS Measurement [mm]	LIF Measurement [mm]	Error (%)
2.0	148.33	6.2427	0.3755	0.3964	0.5495	38.63
2.0	125.00	6.3475	0.3103	0.3732	0.4060	8.79
2.0	110.00	6.4148	0.2684	0.3683	0.3644	-1.06
2.0	101.67	6.4523	0.2451	0.3694	0.3540	-4.18
2.0	85.00	6.5271	0.1985	0.3524	0.3435	-2.52
2.5	135.00	8.0298	0.3285	0.3756	0.4267	13.60
2.5	116.67	8.1121	0.2773	0.3744	0.3748	0.11
2.5	102.50	8.1757	0.2377	0.3606	0.3644	1.06
2.5	85.00	8.2543	0.1888	0.3646	0.3435	-5.78
2.5	76.67	8.2917	0.1655	0.3575	0.3748	4.85
3.0	125.00	9.8019	0.2908	0.3552	0.3644	2.59
3.0	105.00	9.8917	0.2349	0.3506	0.3540	0.96
3.0	91.67	9.9516	0.1977	0.3497	0.3644	4.21
3.0	73.33	10.0339	0.1464	0.3358	0.3540	5.41
3.5	113.33	11.5815	0.2484	0.3514	0.3435	-2.24
3.5	96.67	11.6563	0.2019	0.3442	0.3540	2.84
4.0	133.33	13.2189	0.2946	0.3470	0.3435	-1.00

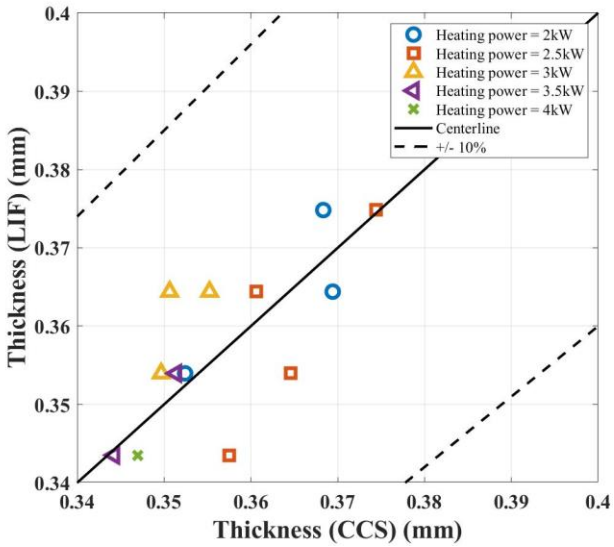

Figure 21. Comparison of thickness data obtained by CCS (x-axis) and LIF (y-axis).

Film thickness data are plotted for both the liquid and vapor superficial velocities in Figure 22. An increasing trend is observed in the plot for liquid superficial velocity, whereas a decreasing trend is observed in the plot for vapor superficial velocity. These trends clearly indicate the effect of both superficial velocities on film thickness. A high liquid mass flow rate causes a thicker liquid film because liquid flows as a film in the annular flow. Meanwhile, a high vapor superficial velocity increases the interaction with the liquid film and causes more droplets to travel inside the vapor (gas) core, which results in a thinner liquid film. This trend corresponds to the models recommended in the previous studies conducted on the water–air environment (Dobran, 1983; Schubring, 2009). This is notwithstanding the difference in boundary conditions and orientations between those studies and the present study.

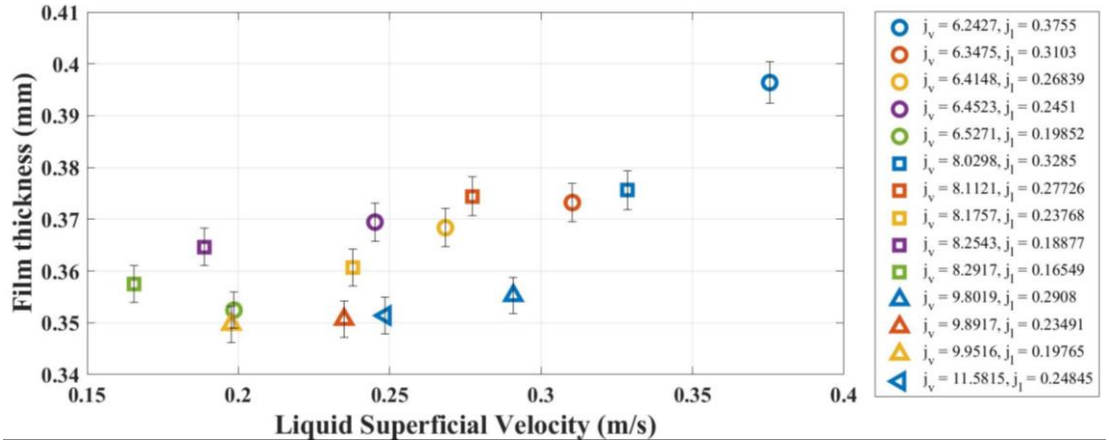

(a)

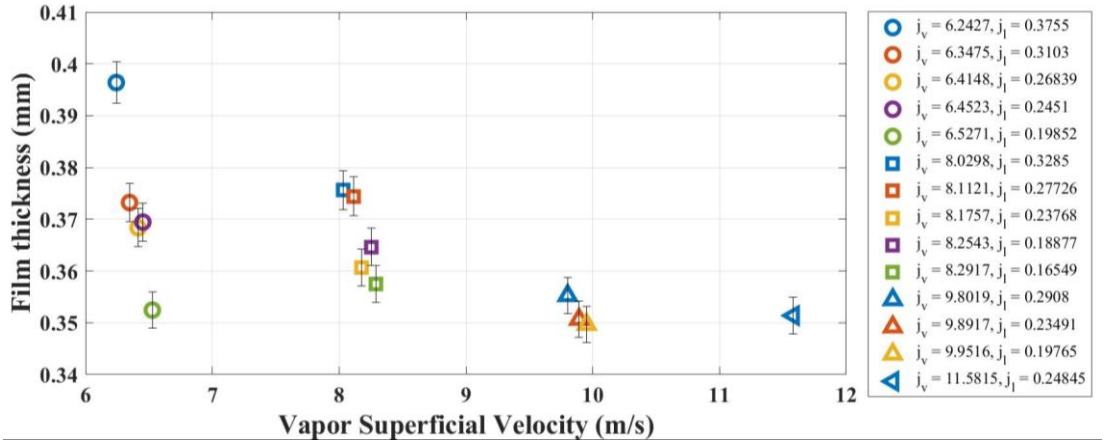

(b)

Figure 22. Thickness for concentric case plotted with respect to (a) liquid superficial velocity, (b) vapor superficial velocity.

Figure 23 presents the film thickness data plotted with respect to both liquid and vapor superficial velocities at the narrow gap side of the eccentric geometry. Although the thickness of the film at the wide gap side is also measured, the data are excluded from the analysis because they show a trend and value similar to those of the concentric case. Meanwhile, the liquid film on the narrow gap side has a smaller value than that for the

concentric geometry case. In both plots, the negligible variation in the thickness was caused by the variation in the liquid superficial velocity from ~0.15–~0.34 m/s and the vapor superficial velocity from ~6.5–~13.2 m/s. Outside these ranges (where the churn flow is likely to be dominant because of the large liquid superficial velocity and marginal vapor superficial velocity), the film thickness varies rapidly because of the variation in both the superficial velocities. Further, the data indicates that a saturated point of the base film thickness occurs when the flow path of the vapor is relatively small. The mechanism of this saturation can be explored further by observing the local vapor core and liquid film velocities.

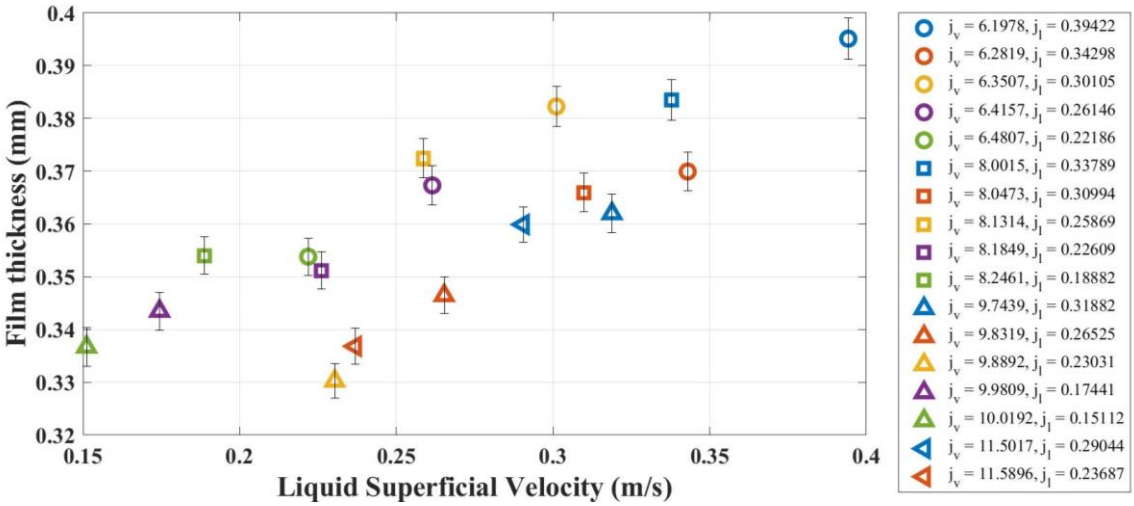

Figure 23. Thickness with respect to liquid superficial velocity plotted for eccentric case.

4.2. Wave characteristics

Figure 24 shows that the film thickness obtained by LIF is plotted using the phase-field of position and time to determine both temporal and spatial characteristics of the liquid film flow. The progress of waves on the surface of the base film can be conveniently visualized in this manner. The slope of the wave indicates that the velocity and peak can be directly converted to the amplitude using the conversion rate. A total of 100 waves were selected from 0 to 2.5 s of the phase-field and measured for each case to increase the statistical reliability of the data. As an example of the measurement, the data at three points and CCS measurement results were plotted with respect to the time scale and presented at the bottom of the figure. The data from the CCS show good agreement with the base film thickness measured by LIF.

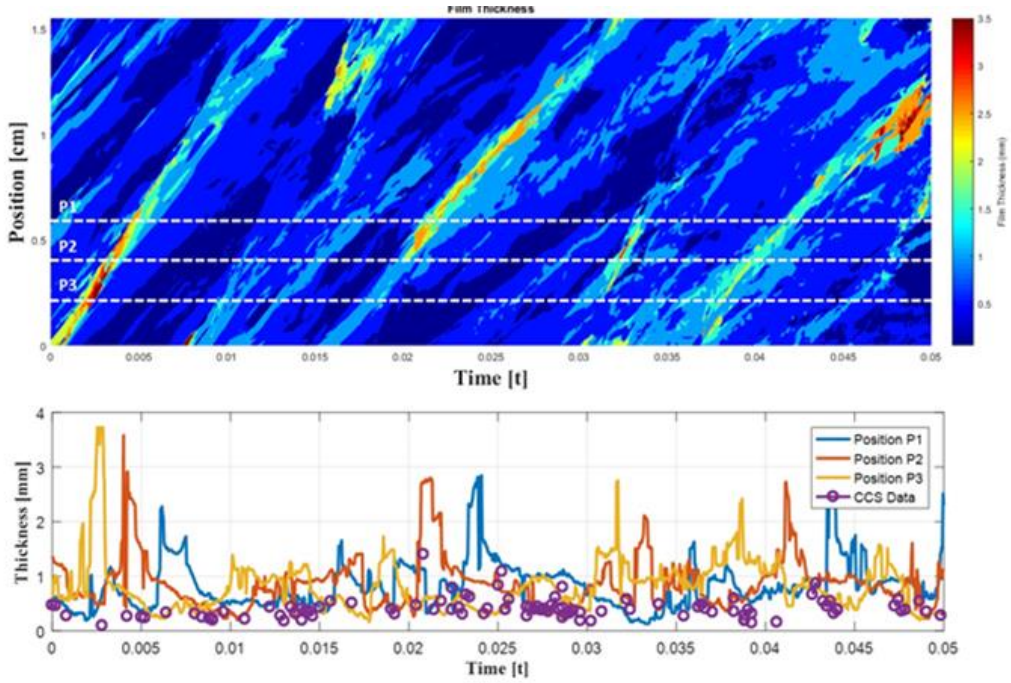

Figure 24. Liquid film phase field with respect to position and time (top) and point-wise liquid film thickness with respect to time (bottom) in annular flow

The amplitude of the wave is plotted with respect to liquid and vapor superficial velocities in Figure 25. The amplitude of the wave increases with an increase in the liquid superficial velocity. This increasing trend can be explained by the liquid flow rate passing through the test section. Furthermore, the amplitude of the disturbance wave can be increased as the wave structure changes from a smooth wave to a roll wave because of the increase in both the liquid and vapor superficial velocities (Levy, 1999). The amplitude attains its maximum value where the breakdown of the roll waves and the onset of liquid entrainment occur.

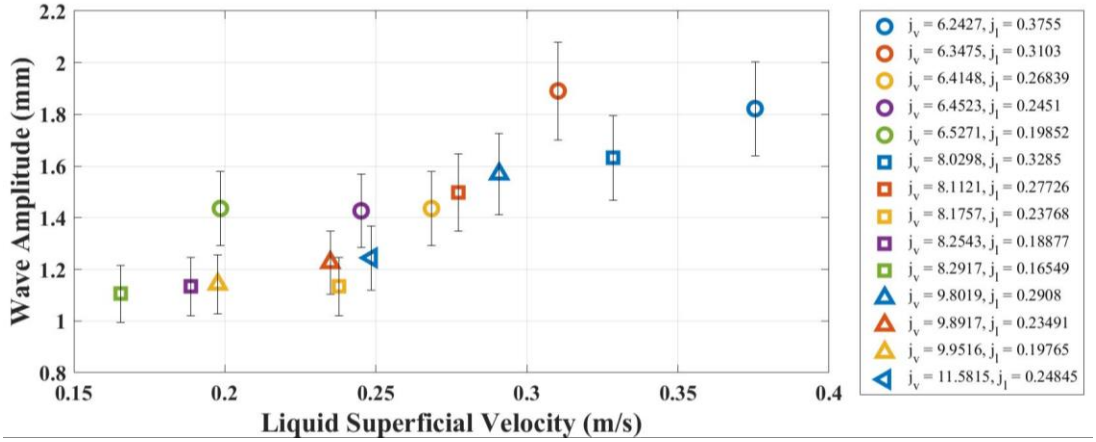

Figure 25. Wave amplitudes plotted with respect to liquid superficial velocity.

Figure 26 presents the result of wave velocity measurement over the vapor superficial velocity. An increasing trend with the vapor superficial velocity can be observed and it indicates that the velocity of the vapor (gas) core has a significant influence on the velocity of the wave. This trend is similar to that observed in the early experiments performed in bare tubes with water–air (Hall Taylor et al., 1963; Nedderman & Shearer,

1963). When the momentum exchange occurs at the interface between the liquid and the vapor, the vapor loses its momentum because it is faster than the liquid film. Therefore, the amplitude and velocity of the disturbance wave are important parameters for modeling the decrease in pressure (Wallis, 1969). Under this context, it is apparent that a higher vapor superficial velocity would cause a higher wave velocity through momentum transfer. Therefore, a larger pressure drop is likely.

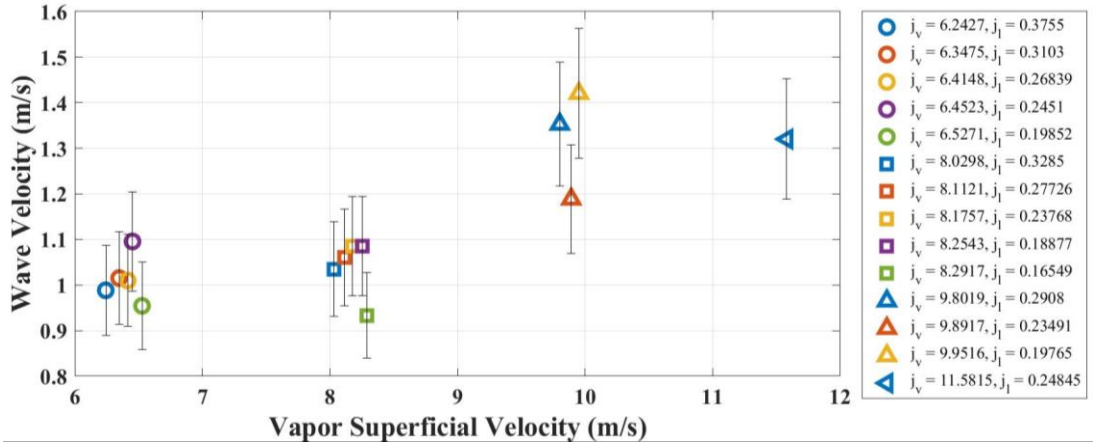

Figure 26. Wave velocity plotted with respect to vapor superficial velocity.

4.3. Heat transfer coefficient

The heat transfer coefficient is calculated using the following equation, and it is based on the assumption of uniform heat flux along the heater surface.

$$h = \frac{q''}{T_{surf.} - T_{sat}} \qquad Eq\ 1$$

where q'', $T_{surf.}$, and T_{sat} represent the heat flux, temperature of the heater surface, and saturation temperature of the fluid, respectively. The uncertainty propagation is performed based on the measurement uncertainty of thermocouples.

Figure 27 presents the heat transfer coefficients calculated according to both the liquid and vapor superficial velocities. The primary relationship between liquid superficial velocity and heat transfer coefficient is presented in Figure 27 (a). This result implies that the thickness and velocity of the liquid film play dominant roles in the heat transfer mechanism at the heater surface. The heat transfer coefficient shows an increasing trend with respect to superficial vapor velocity in Figure 27 (b). The increasing trend can be conjectured to be an effect of the increase in heat flux on the heat transfer coefficient given that the vapor superficial velocity is controlled by the heat flux through the heater. Thus, a higher heat flux can results in a higher heat transfer coefficient until the boundary conditions attain dry out. Three points at the bottom right in Figure 27 (b) show the results of the high-power input cases that attained dry out; the results indicate that the heat transfer coefficient decreases when the boundary conditions attain dry out, which causes the disappearance of the liquid film at the heater surface and a rapid increase in the surface temperature.

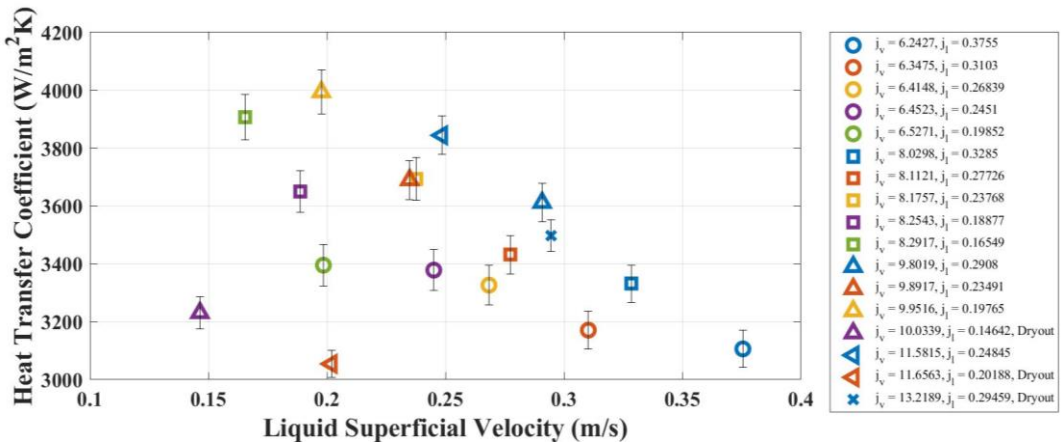

(a)

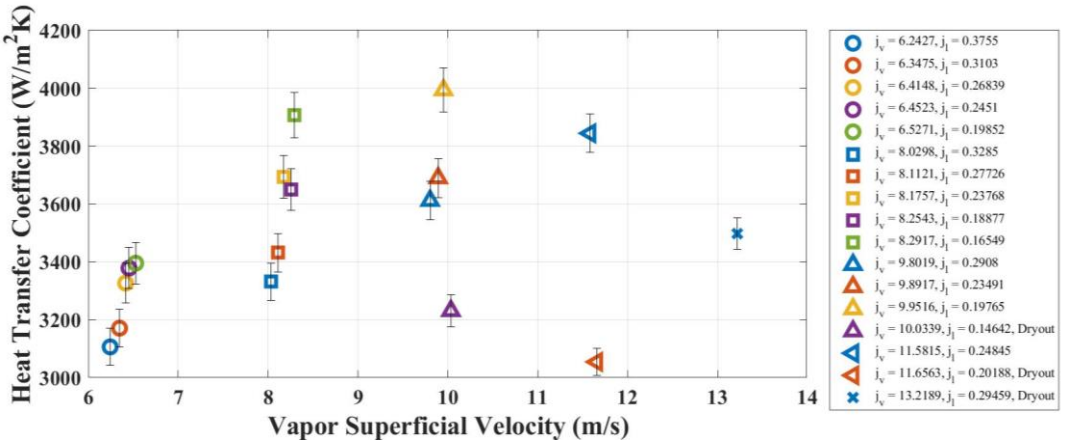

(b)

Figure 27. Heat transfer coefficient for concentric case plotted with respect to (a) liquid superficial velocity, (b) vapor superficial velocity.

The experimental result of the study is compared with the previously indicated correlation in Figure 28. Few experimental studies have been conducted on annular flow with the convective heat transfer in annulus geometry. Therefore, the following general correlation recommended by Kandlikar (1990) for the saturated flow boiling region in smooth circular tubes is used for comparison.

$$h = h_{sp}\left[0.6683\left(\frac{\rho_l}{\rho_v}\right)^{0.1} x(1-x)^{0.64} f(Fr) + 1058\left(\frac{q''}{W \cdot h_{fg}}\right)(1-x)^{0.8} G_{s.f}\right] \qquad Eq\ 2$$

where ρ_l and ρ_v represent the densities of liquid and vapor, respectively; x denotes the time-averaged mass fraction of vapor; $f(Fr)$ represents a stratification parameter equal to one in vertical geometry; W represents the mass flux of the channel; h_{fg} denotes the latent heat; and $G_{s.f}$ represents the surface liquid combination coefficient, which is 1.63 in this study. The single-phase heat transfer coefficient for the turbulent, fully-developed flow in a circular tube (h_{sp}) is calculated using the Dittus–Boelter equation (Dittus & Boelter, 1930):

$$\mathrm{Nu} = 0.023\,\mathrm{Re}^{0.80}\,\mathrm{Pr}^{0.4}. \qquad Eq\ 3$$

The result reveals an offset between the experimental result and the correlation. This offset may have originated from the difference in geometry. In a bare tube geometry, most liquid (i.e., except the droplets traveling inside the vapor core) flows as a film near the heating wall. Meanwhile, in annuli geometry, the liquid film flows in two regions: the inner wall of the outer tube and the wall of the heater. If the total amount of the liquid is identical for the two cases, a smaller amount of liquid flows near the heater surface in the case of the annuli geometry. The lower mass flow rate of the liquid film results in a smaller film thickness, which yields a smaller heat transfer coefficient because the thermal conduction through the liquid film functions as a primary heat transfer mechanism in annular flow (Collier & Thome, 1994). Further, the lower liquid flow rate results in a

smaller amplitude and velocity of the disturbance wave. This was recently revealed to have a non-negligible effect on the heat transfer coefficient in the case of stable annular flow (Su et al., 2019). Therefore, the experimental result reveals a heat transfer coefficient smaller than that calculated using the correlation recommended for a bare tube. This is because a smaller amount of the liquid flows in the heater surface compared with that in the bare tube case.

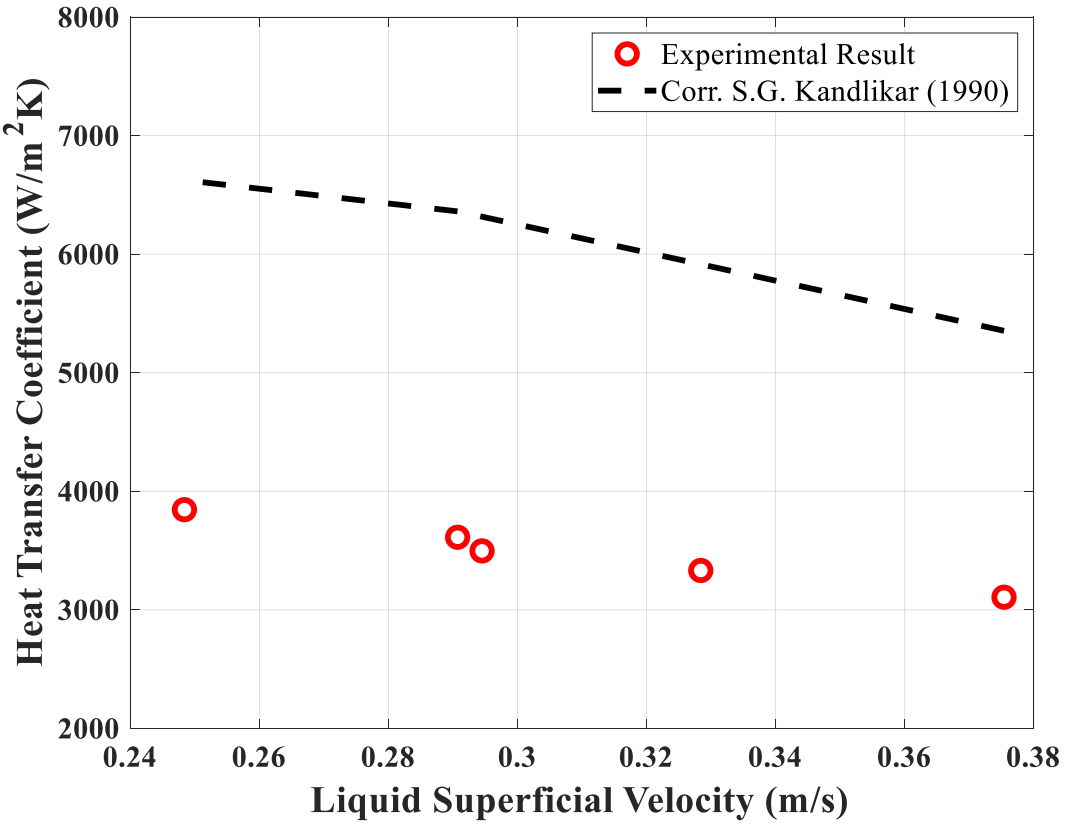

Figure 28. Comparison between heat transfer coefficient obtained from the experimental result of and that obtained using correlation (Kandlikar, 1990).

4.4 Droplets and Bubbles

The measured diameter and velocity from two cases, (a) j_v = 9.744 and j_l = 0.3188; (b) j_v = 10.019 and j_l = 0.1511, are plotted against each other in Figure 29. When the droplet or bubble disappears during tracking, it is marked with different colors. Bubbles and droplets can be distinguished according to their speed. Since bubbles travel inside the liquid film, their velocity is relatively low and has a small variance. Droplets move faster through the gas-core, and therefore, the velocity of bubbles is in the slow region between 0.5 and 2.0 m/s, while that of the droplets is distributed from 1.0 to 5.0 m/s in the present observation.

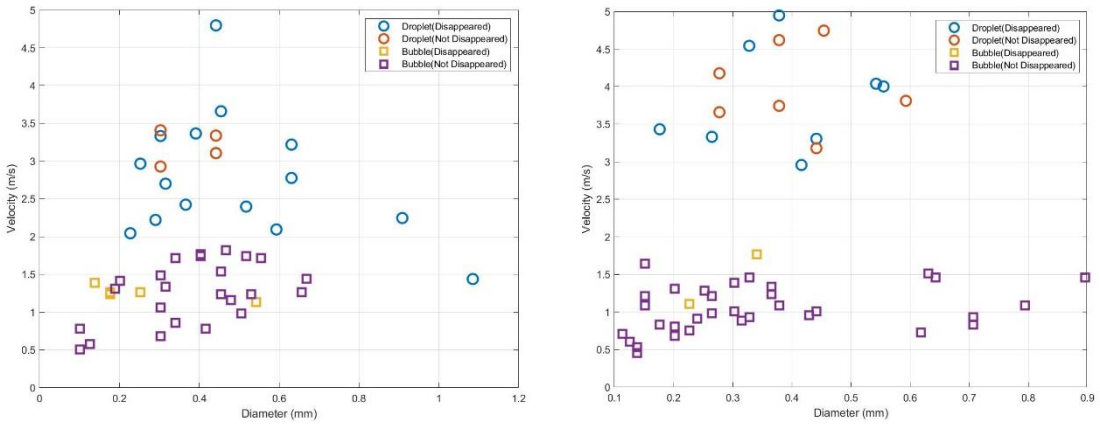

(a) (b)

Figure 29. Size and velocity distributions of droplets and bubbles with boundary conditions, (a) j_v=9.744, j_l=0.3188 (b) j_v=10.019, j_l =0.1511.

The measured diameter and velocity of droplets are plotted in Figure 30 (a), and the results of bubbles are plotted Figure 30 (b). The velocity of the droplets in the case of j_v = 10.019 is higher than that in the case of j_v = 9.744, shown in Figure 30 (a). In contrast, in Figure 30 (b), the velocity of bubbles seems not to be seriously affected by

liquid superficial velocity, even though the ratio of the change in the liquid superficial velocity is considerably larger than the vapor superficial velocity. Further analysis can be made when the study of Moeck and Stachiewicz (Moeck & Stachiewicz, 1972) is introduced. From their study, predict the vapor velocity can be predicted from the size and the velocity of the largest bubble which is ~ 5.5 m/s. Another analysis can be made by Stokes number. From the calculation, a droplet with approximately 100 micrometers can indicate the velocity of the vapor in our system which is not possible to be measured due to the limitation of the visualization. However, it can be expected that no matter how small the droplet is, its velocity will be bounded smaller than 5.5 m/s with the boundary condition.

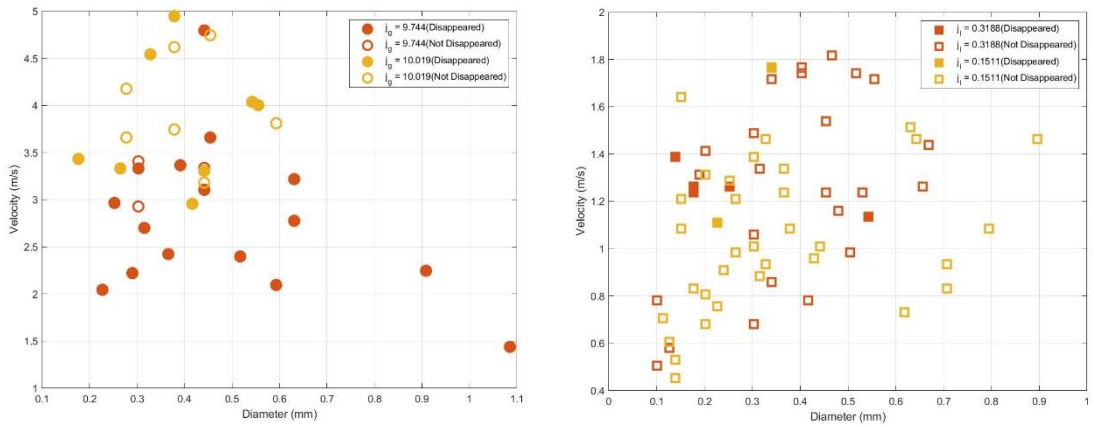

(a) (b)

Figure 30. Size and velocity distributions of (a) droplets and (b) bubbles.

Disappearing bubbles and droplets are presented in Figure 39. A disappearing bubble can be considered as bursting or rupturing into the gas phase from the liquid film.

It seems that there is no significant difference in the velocity and diameter between the disappearing and non-disappearing bubbles. Disappearance of droplets, on the other hand, represents the deposition of droplets. When a droplet hits the surface of liquid film, it leaves its trajectory and generates other droplets by making entrainment phenomena called the liquid impingement. Unlike bubbles, major number of disappearing droplets are located at the velocity range of 1.7 ~ 3.2 m/s and the diameter range of 0.1 ~ 0.4 mm. Non-disappearing droplets, which are not interacting with the liquid film, tend to travel faster than disappearing droplets. However, it seems that the velocity of a non-disappearing droplet decreases as the diameter increases.

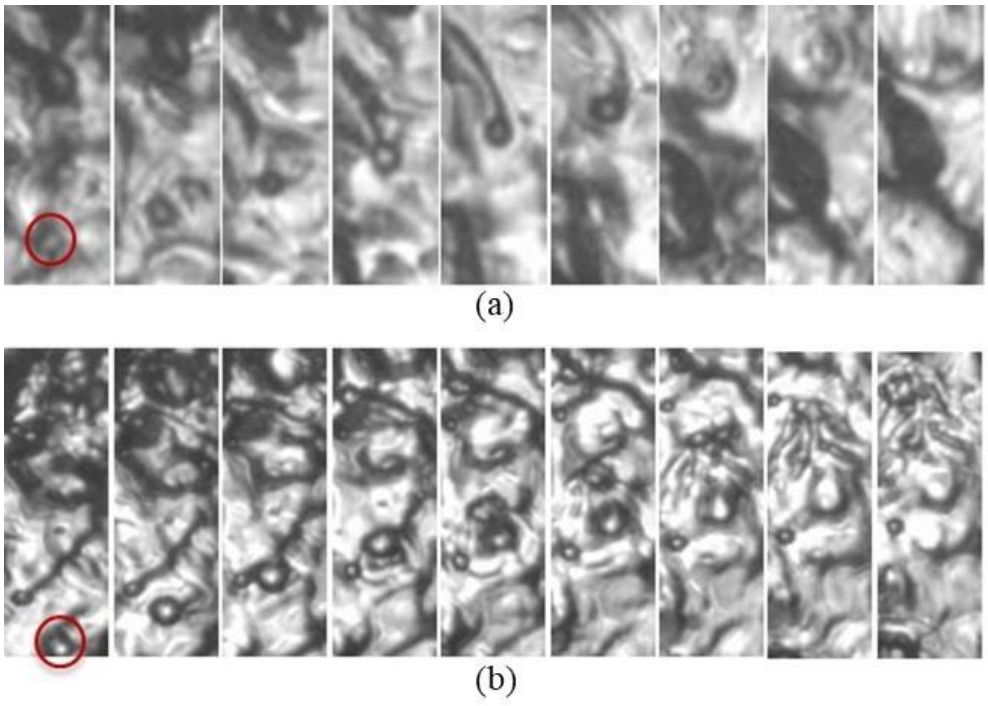

Figure 31. Disappearance of droplets (top, (a)) and bubbles (bottom, (b)) captured by shadowgraph.

Deeper investigation on the diameter and velocity of bubbles were conducted. For each case, 50 bubbles were selected randomly, and their diameter and velocity were measured. In Figure 32, the diameter and velocity information of total bubbles is plotted against each other. The increasing trend of velocity based on diameter can be observed from the plot. The histogram of the diameter shows that the largest number of the bubbles have diameters between 0.2–0.3 mm, and the counts of such bubbles with larger dimeter decreases rapidly. The distribution of the velocity seems to follow the natural distribution with 0.6–0.8 m/s of the centered value.

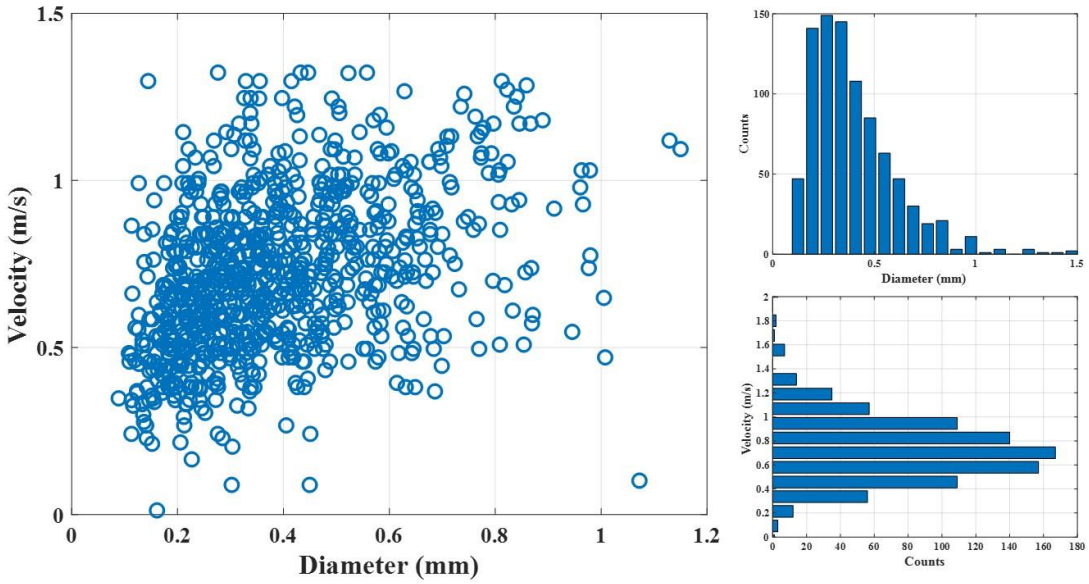

Figure 32. Relationship of diameter and velocity of bubbles and statistics of the measurement.

Figure 33 presents the result of bubble diameter measurement over the vapor superficial velocity. An increasing trend with the liquid superficial velocity can be

observed. The results presented above indicate that the thickness of the liquid film forms a positive relationship with the liquid superficial velocity. Since thicker liquid films flow with higher liquid superficial velocity, larger bubbles can be observed. A decreasing trend is observed for the vapor superficial velocity. The same analysis can be performed because the thickness of the film reduces with an increase in the vapor superficial velocity. Further, a higher vapor superficial velocity interacts with the liquid film that causes bursting or separation of large bubbles near the interface.

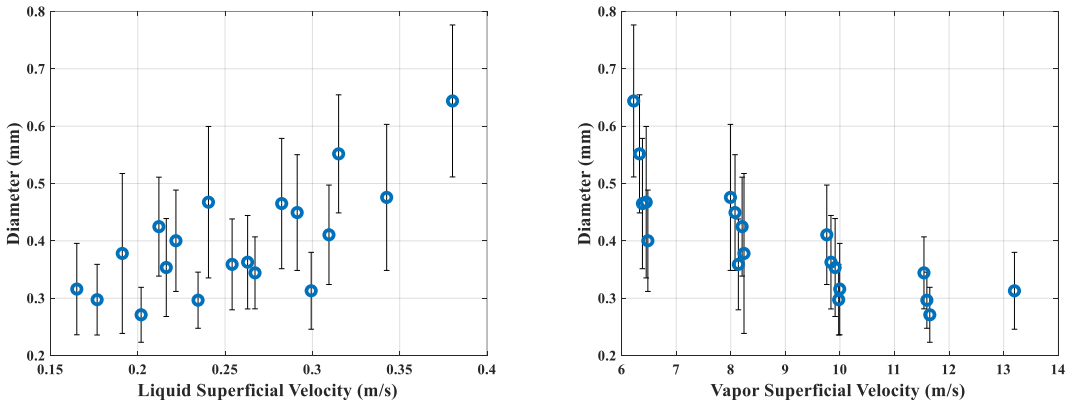

(a) (b)

Figure 33. Diameter of bubbles in concentric geometry plotted with respect to (a) liquid superficial velocity, (b) vapor superficial velocity.

Figure 34 shows plots of the velocity with respect to the vapor and liquid superficial velocities. Unlike the diameter, the velocity of the bubble has weak relationship with these parameters; this is not expected. Faster moving liquids and gases do not cause faster moving bubbles inside the liquid film.

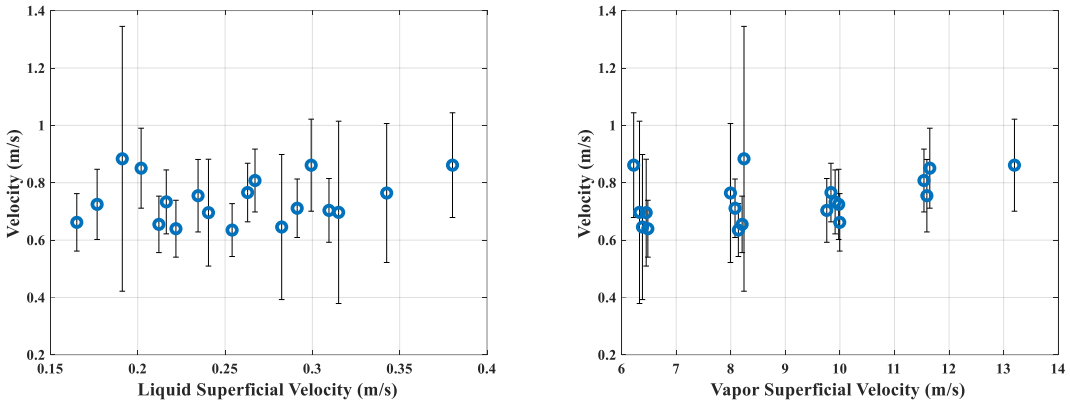

(a) (b)

Figure 34. Velocity of bubbles in concentric geometry plotted with respect to (a) liquid superficial velocity, (b) vapor superficial velocity.

4.5 Pressure Drop

Gauge pressure was measured at the inlet of the test section. The pressure difference between a port 0.23 m before the inlet and a port 0.23 m after the outlet (1.475 m of total distance) of the test section was measured using a DP transducer. Another pair of DP ports were located with a 150 mm distance at the top of the heating region to measure the pressure drop during the annular flow. A total of three types of pressure—gauge pressure at the inlet, pressure drops of the total test section, and pressure drop of the annular flow region—were measured in this study.

4.5.1 Pressure Drop in Single- and Two-Phase Flows

The total pressure drop of the test section during the single-phase flow was measured to check the reliability of the measurement system. Starting from zero, the flow rate was increased up to 160 g/s, which corresponds to a Reynolds number of

15729. The result of the measurement is shown in Figure 35. The marked points present the averaged data, and the shaded region indicates the standard deviation of the data which can be considered as a fluctuation of the pressure drop attributed to the nature of the flow. A regularly increasing trend of the pressure drop based on the Re number can be found except for the case Re = 2593, where the transition from laminar to turbulent flow is expected.

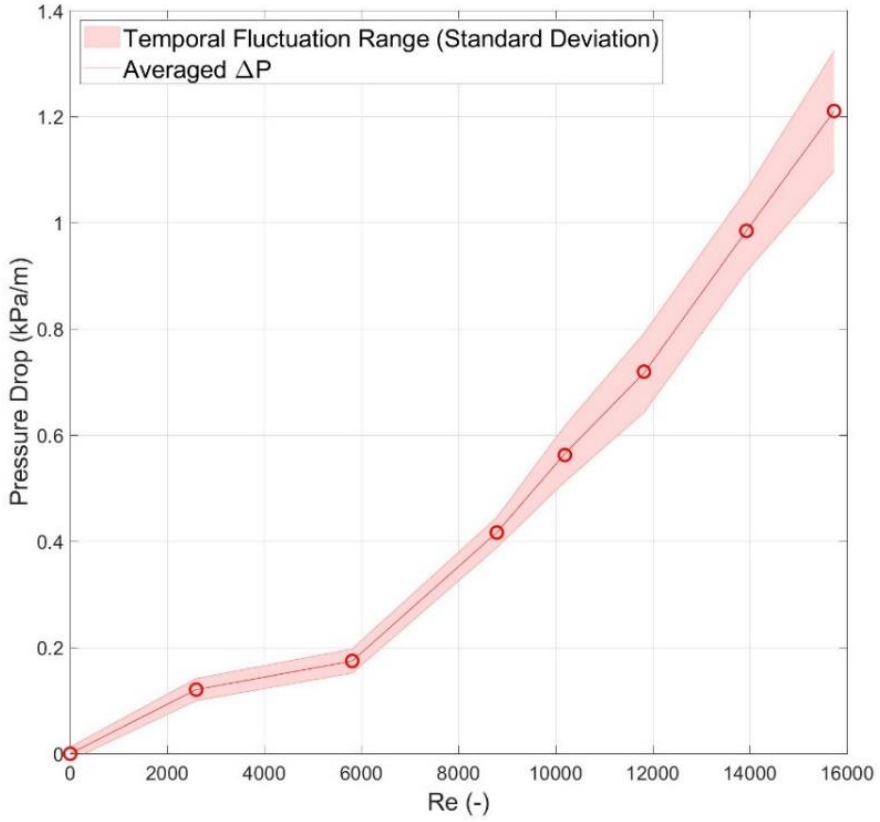

Figure 35. Total pressure drops of single-phase flow experiment.

The total pressure drop of the test section during the two-phase flow was measured by fixing the inlet flow rate while changing the heat flux from 33.51 to 113.92 W/m^2. The result of the measurement is illustrated in Figure 36. The total pressure drop increases with an increase in the heat flux because it has a close relationship with the void fraction and the quality of the channel; this increasing trend seems to be reasonable. An increased temporal fluctuation range can be observed when it is compared with the single-phase flow case. From the nature of the two-phase flow, a higher fluctuation of the pressure can be expected with an increase in the vapor superficial velocity.

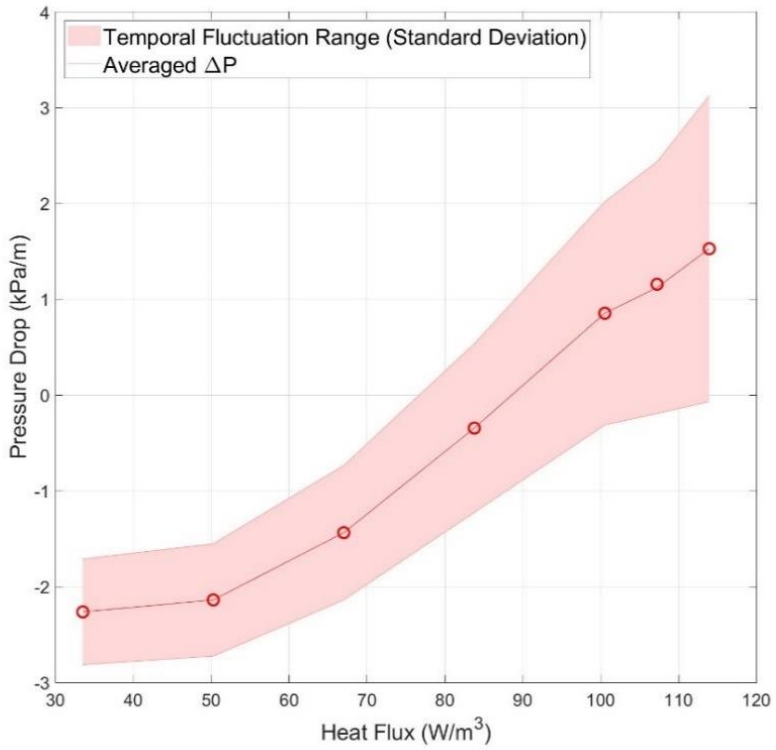

Figure 36. Total pressure drops of two-phase flow experiment.

Figure 37 presents the pressure drop measurement result of the top 0.15-m region where the annular flow is expected to occur during the actual experiment. Unlike the total pressure drop measurement, a clear change in the pressure drop attributed to a change in the flow pattern can be observed because the total distance of the measurement is relatively small. In this case, the heat flux is 107.22 W/m^2, and the annular flow appears at the measured region. At the moment, the pressure drop between the 150 mm distance at the top of the heating region can be measured by the DP transducer, whereas the other one only measures the total pressure drop of the whole channel where the bubbly, churn, and annular flow patterns exist. The result indicate that the pressure drop decrease as heat flux increases until the heat flux reaches 67.01 W/m^2. With an increase in the heat flux to 107.22 W/m^2, the pressure drop increases, and it starts to decrease again when the heat flux is increased to 113.92 W/m^2. A large fluctuation in the pressure can be expected from the standard deviation, which seems reasonable if there is active phase change and interaction between the liquid and the vapor.

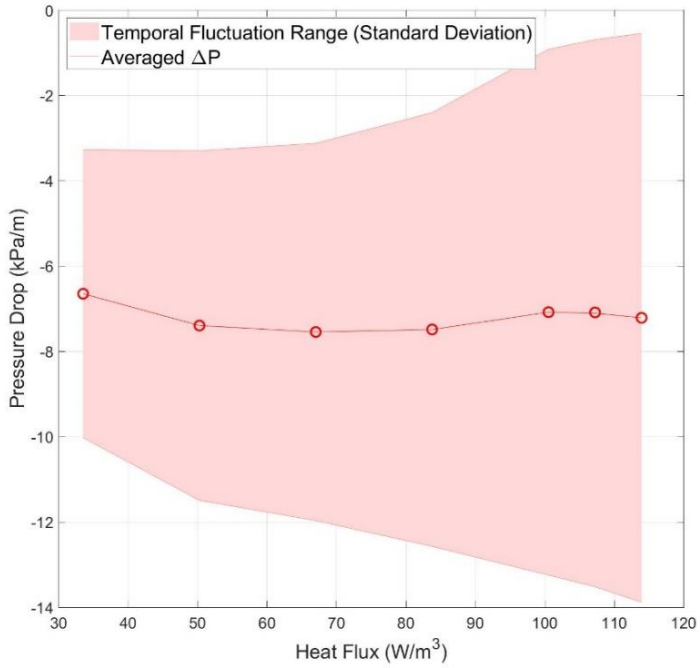

Figure 37. The pressure drops of the annular flow regime.

4.5.2 Pressure Drop of Concentric Case

The pressure drop of the annular flow region is plotted against both the liquid and the vapor superficial velocities in Figure 38. An increasing trend in the pressure drop according to the liquid superficial velocity can be found in Figure 38 (a). The pressure drop seems to decrease with an increase in the vapor superficial velocity. However, this is the result of the strong influence of the superficial liquid velocity. The control variables include the inlet liquid flow rate and the power input, and therefore, the pressure drop attributed to the vapor superficial velocity has to be compared across different conditions. The gray circles in Figure 38 (b) show the effect of vapor superficial velocity with similar values of liquid superficial velocity.

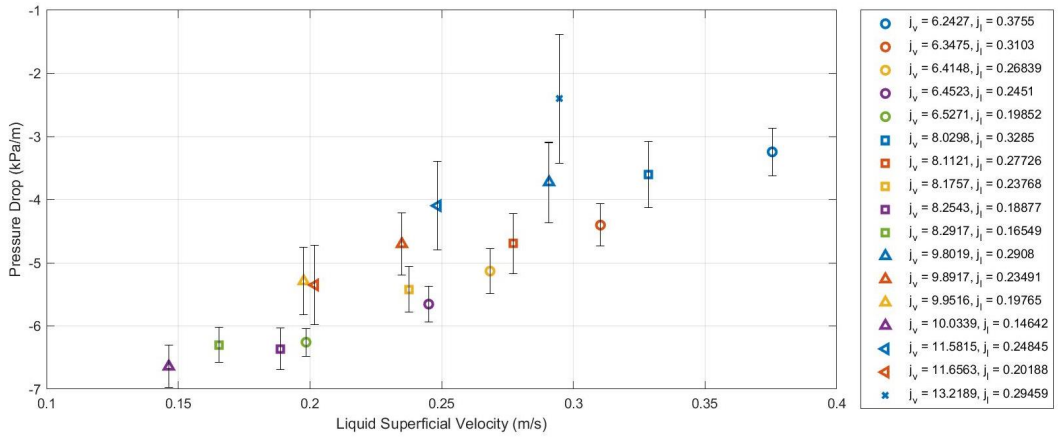

(a)

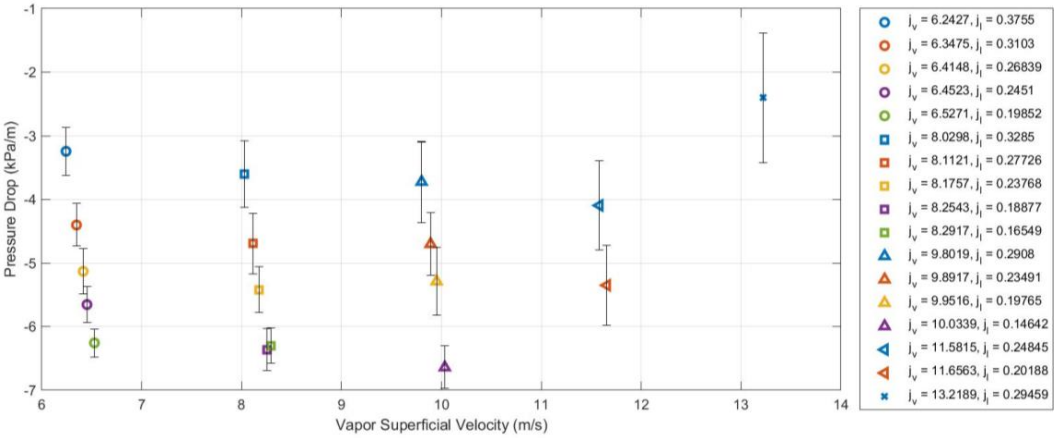

(b)

Figure 38. Pressure drop of concentric case plotted against (a) liquid superficial velocity, (b) vapor superficial velocity.

4.5.3 Pressure Drop of Eccentric Case

Figure 39 presents the result of the pressure drop at the annular flow region in the case of eccentric geometry. The pressure drop length results indicate similar trends with the concentric case, which increases with an increase in the liquid or vapor superficial velocities. When the orientation of the measurement is considered, the pressure drop is

measured at the wide gap side of the test section in the case of eccentric geometry. The center of the heating rod is moved along the perpendicular plane to the camera. The pressure ports are located on a plane that is at 60° with the perpendicular plane. This result implies that there are no significant differences in not only the pressure drop but also the hydraulic parameters such as film thickness, vapor velocity, and wave characteristics between the concentric case and the wide side of the eccentric case.

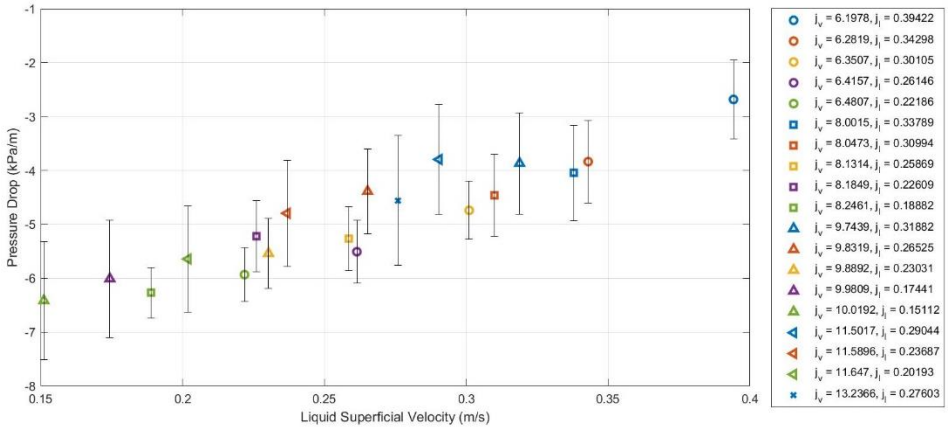

(a)

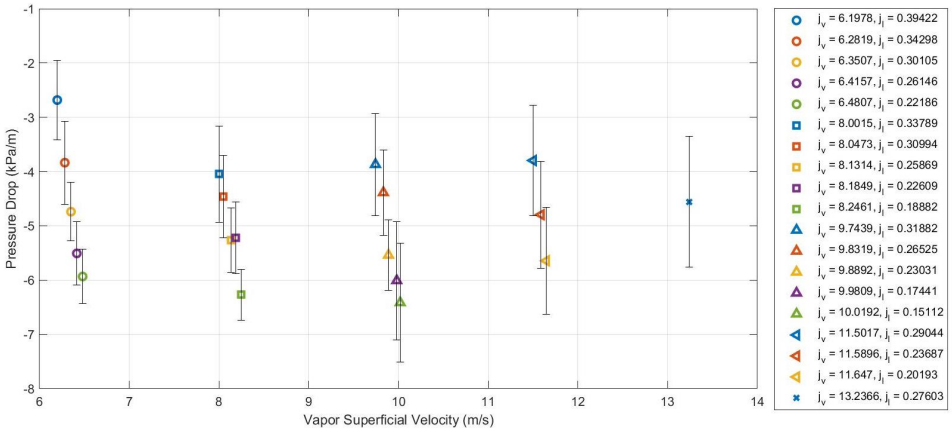

(b)

Figure 39. Pressure drop of eccentric case plotted against (a) liquid superficial velocity, (b) vapor superficial velocity.

CHAPTER V

CFD MODELING

Computational fluid dynamics is a strong tool to analyze the fluid system with high fidelity. CFD can be used as a high-fidelity analysis tool because hydraulic phenomena play a dominant role in the operation of the nuclear reactor. However, there has been a limited number of studies to perform numerical simulations on two-phase flows inside the reactor when it is compared with a single-phase flow. This is because CFD methodology used to analyze the complex multiphase phenomena occurring inside of the reactor is not well-established or modeled. Inside the reactor, there are multiple types of phenomena that require deeper understanding and modeling to be solved numerically; these include phase change, rapid two-phase flow, and interactions at free surface. Modeling those phenomena including the non-isothermal conditions, is a highly challenging issue in the research field of CFD, and it is the primary motivation of this study.

OpenFOAM is a free, open-source CFD software created by Henry Weller in 1989. Since it is free software, OpenFOAM does not require any license purchase and has a huge database created by individual users. The solver provides a wide range of features to solve complex fluid flows, turbulence, and heat transfer. Besides, users can easily and freely create custom solvers and boundary fields in the OpenFOAM environment using the C++ script. From its first release in 2004, the solver has been widely studied, modified, and used in both academic and industrial fields because of its advantages. However, a relatively small number of studies have been conducted for the

two-phase flow using OpenFOAM. The number reduces further when the CFD of phase change is considered; this may be caused by the late introduction of the first standard phase change solver in 2016. Therefore, only a limited number of studies on phase change have been conducted using OpenFOAM, while most of the early studies are conducted using other commercial programs.

In this study, the phase change simulation capability of OpenFOAM will be investigated to evaluate its potential applicability for high-confidence phase change and annular flow modeling and simulation. As a first step, the performance of standard solvers is verified. Then, custom solvers with better performance are built by modifying and merging standard solvers. In the last chapter, phase change models are implemented in the OpenFOAM environment and explored to find the applicable model for the simulation of annular flow in boiling.

5.1 Phase Change Simulation Using Standard Solver

OpenFOAM is a CFD tool that highly encourages personal modification and redistribution. Due to these characteristics, numerous subset solvers have been developed and included by many researchers. The official distributor of the program regularly updates and upload newer versions of OpenFOAM almost once a year. OpenFOAM v1906, which was distributed in 2019, was used in this study.

5.1.1 interCondensatingEvaporatingFoam

Selecting the proper solver based on the case study the first and most important step of using OpenFoam. The selection of the solver is decided based on the choice of multiphase model and the consideration of flow conditions. There are two well-known large groups of models: Euler–Euler and Euler–Lagrange. In this study, the Euler–Lagrange approach is not considered because tracking a large number of particles, droplets, and bubbles is not important for capturing the physics inside the heat pipe. Among the simplified Euler–Euler approaches, the volume of fluid (VOF) model can be used in the case of free-surface multiphase flow while the mixture model and Euler model are more applicable to the case wherein the momentum exchange between two-phase is a dominant parameter. Therefore, VOF is selected as a model to simulate a thermosyphon.

Figure 40 represents the two-phase flow solvers provided by OpenFOAM. The selection of the VOF method narrows down the candidates of solvers to interFoam solvers. There are several solvers in the group of interFoam. For example, interMixingFoam, interPhaseChangeFoam, interIsoFoam, etc. Among them, interCondensatingEvaporatingFoam has the capability of simulating phase change with a nonisothermal condition.

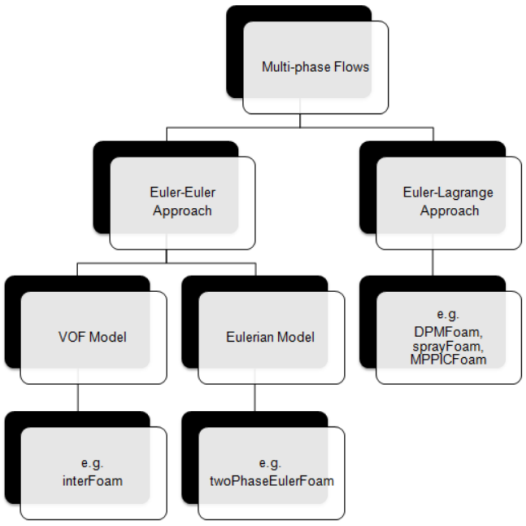

Figure 40. OpenFOAM solvers for two-phase flow (from : http://www.cfdyna.com/Home/of_multiPhase.html)

From OpenFoam manual pages (OpenFOAM Manual), the interCondensatingEvaporatingFoam (iCEF) is explained as,

"Solver for two incompressible, nonisothermal immiscible fluids with phase-change, using VOF phase-fraction based interface capturing. With optional mesh motion and mesh topology changes, including adaptive re-meshing."

Under the assumption that the speed of the vapor inside of a water/vapor thermosyphon is lower than 0.3 C, where C represents the Mach number, the iCEF can be a reasonable choice as a solver.

5.1.2 File Structure of the Solver

Viewing tutorials is a good start point to identify the basic structure of the solver. It is highly recommended to create a directory in which users can copy and run the tutorial.

The tutorial "condensatingVessel" is the only tutorial provided for iCEF in OpenFOAM v.1912. Refrigerant (FC-72) gas is contained in a vessel, and its condensation can be observed after transient calculations. The structure and contents of all files need to be explored thoroughly because this tutorial is a start point of building a solver for the thermosyphon simulation. When users open the directory, they can find three directories (0, constant, system) and two shell scripts (Allrun, Allclean). Directory "0" contains a set of parameters required to solve governing equations. Its name 0 means the initial time step of the simulation. Therefore, all initial boundary conditions and values for every parameter are set in this folder. Once the simulation starts and the numerical calculation moves to the next time steps, the solver generates folders with the name of the simulation time and writes values for each parameter. For example, if a user sets a 1.0 s write interval, the names of output directories will be 1, 2, 3, ..., which have output values of parameters at the time step of their names.

In the next directory, "constant," the user can set properties related to materials and domain. Further, the body force (gravity) can be imposed through this directory. The last directory, "system," contains the setup of the solver, including mesh, scheme, and time marching. Table 7 contains information about each script more in detail.

Table 7. File structure of the tutorial, condensatingVessel

0	T		Initial and boundary conditions of temperature field.
	U		Initial and boundary conditions of velocity field.
	alpha.liquid		Initial and boundary conditions of phase fraction.
	epsilon		Initial and boundary conditions of turbulence modeling parameter, epsilon.
	k		Initial and boundary conditions of turbulence kinetic energy, k.
	nut		Initial and boundary conditions of turbulent kinematic viscosity.
	omega		Initial and boundary conditions of turbulence modeling parameter, omega.
	p		Initial and boundary conditions of pressure.
	p_rgh		Initial and boundary conditions of hydrostatic pressure.
constant	polyMesh	boundary	Domain information.
		faces	
		neighbour	
		owner	
		points	
	g		Gravitational acceleration vector.
	phaseChangeProperties		Phase change coefficient, β_e, β_c. (0.1 for Lee model)
	thermophysicalProperties		Saturation temperature.
	transportProperties		Surface tension, density, specific heat, conductivity, and latent heat.
	turbulenceProperties		Turbulence model.
system	blockMeshDict		Mesh building script.
	controlDict		Time marching control parameters, start time, end time, time interval, max Courant number, and write interval.
	fvSchemes		Schemes for ddt, gradient, divergence, Laplacian, interpolation, etc.
	fvSolution		Solvers for parameters, T, U, p, turbulence model parameters, and pressure coupling method.

5.1.3 Simulation Setup for Phase Change Simulation

The solver that can simulate a simplified two-dimensional phase change is built and tested. The code is modified from the tutorial code to perform both boiling and condensation simulations. The modification of the code is presented step by step, file by file, for future study and use.

Mesh and Boundary Conditions

The schematic and boundary condition of this code is shown in Figure 41. In a square-shaped domain, water at the saturation temperature is filled for the boiling simulation. Three walls—right, left, and bottom—are set, and one outlet condition is applied at the top of the domain. For the right and left walls, a constant heat flux condition is set to ensure boiling. For the condensation case, fluid is changed to steam at the saturation temperature, and the direction of the heat flux is applied in the opposite direction. For both cases, gravity is applied in the direction from the top to the bottom.

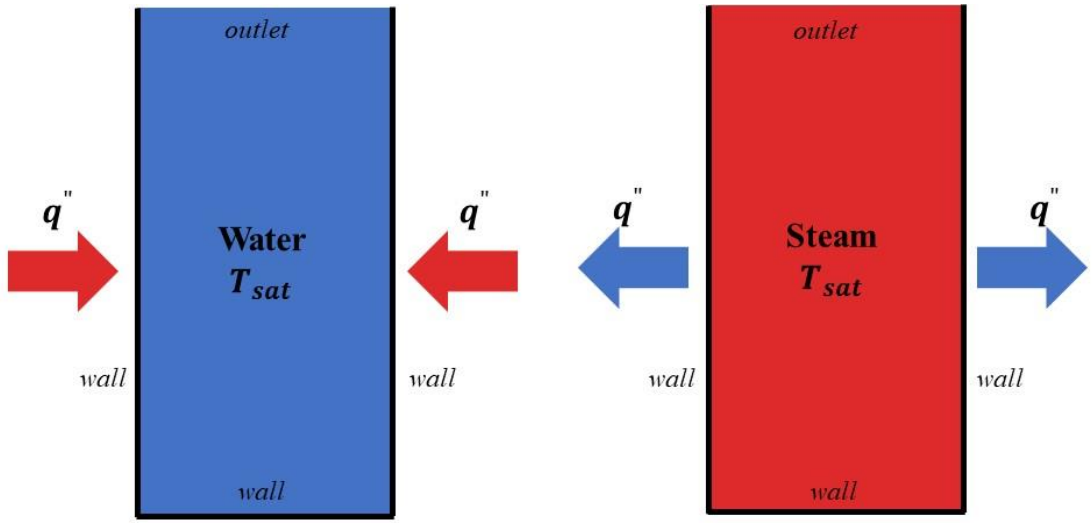

(a) (b)

Figure 41. Schematic of simplified phase change simulation, (a) boiling, (b) condensation

The mesh is built using the *blockMeshDict* file in the system directory. Inside the file, the geometry is built by defining vertices, blocks, and surfaces. The 200 × 100 hex mesh is built with an inflation option near the walls. Domain and boundaries are set in this file. Since OpenFOAM does not provide a 2-D solver, the user should define front and back sides as "empty" boundaries so that the solver does not calculate equations related to those boundaries. The result of the generated geometry and mesh is shown in Figure 42.

The boundary conditions for every parameter can be set in the directory "0". Since most boundary conditions are the same except for values of the internal fields, there are only a few things that need to be changed from the file provided by the tutorial. All initial boundary conditions are listed in

Table 8.

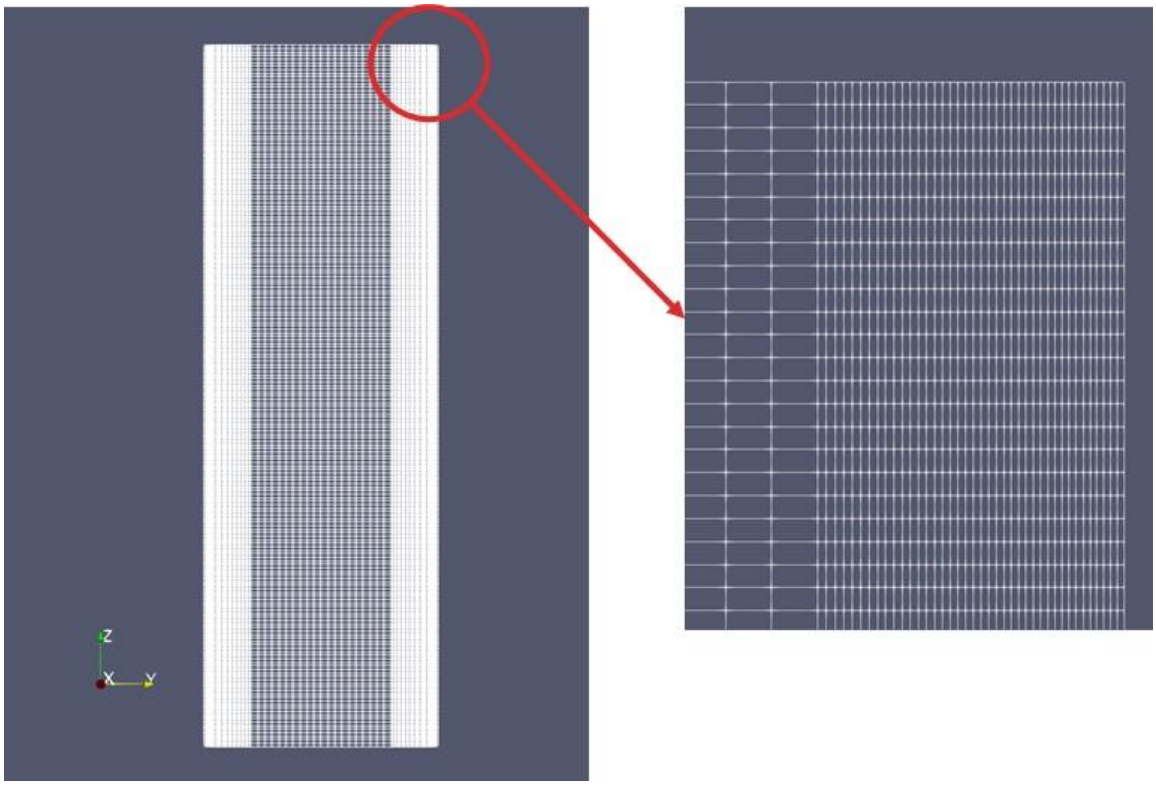

Figure 42. Geometry and mesh of the simply phase change simulation

Table 8. Boundary conditions of the simplified simulation

Parameters	Locations	Conditions
T	internal field	uniform
	bottom wall	zeroGradient
	left and right walls	fixedGradient
	outlet	inletOutlet
U	internal field	uniform
	bottom wall	fixedValue
	left and right walls	fixedValue
	outlet	pressureInletOuletVelocity
alpha.liquid	internal field	uniform
	bottom wall	zeroGradient
	left and right walls	zeroGradient
	outlet	inletOutlet
p	internal field	uniform
	bottom wall	calculated
	left and right walls	calculated
	outlet	calculated
p_rgh	internal field	uniform
	bottom wall	fixedFluxPressure
	left and right walls	fixedFluxPressure
	outlet	totalPressure

Solver Setup

In the “constant” directory, the direction of the gravity needs to be modified. Owing to the difference in geometry, the gravity is set to the y-direction in the tutorial while it needs to be set to the z-direction in this study. Therefore, the gravity vector (0 −9.81 0) is changed to (0 0 −9.81) in the file name “g.” Next, the phase change coefficient (mass transfer intensity factor) is changed according to a previous study (Fadhl and Wrobel, 2013). In the tutorial, both coefficients are set as 150, but Lee’s model suggests a value of 0.1. This change can be made in the file “phaseChangeProperties.” Then, surface tension is applied to simulate the interface between water and vapor. This update is done in the file “transportProperties” by applying a surface tension value at the saturation temperature. The saturation temperature of the water, 373.15 K, can be set in the file “thermophysicalProperties.” The turbulence model is turned off by setting the laminar solver in the file “terbulenceProperties.”

There is nothing to change in the directory “system” except “blockMeshDict” and “controlDict.” In “controlDict,” the end time, time interval, and write interval are adjusted to check the capability of the solver. The same schemes for calculations with tutorials are adopted for this study.

Once this setup is compelete, the simulation can be started by entering the following command.

./Allrun

Result of the Phase Change Simulation

The result of the simulation is shown in Figure 43. Only the calculation of the phase fraction of liquid (alpha.liquid) is checked because of the purpose of this study. The phase change occurs inside the vessel, and the generated steam vapor moves upward while the condensed water liquid moves downward. However, the overall flow patterns of both boiling and condensation do not look physically right. The normal phase change process starts with a generation of the small size of bubbles or droplets attached on the surface of the wall. As time proceeds, the size of objects increases continuously until the buoyancy force becomes the dominant factor of the force balance. After this growing period, bubbles and droplets start to move according to the density difference between the two phases. However, this normal processes are not observed in the result of the simulation.

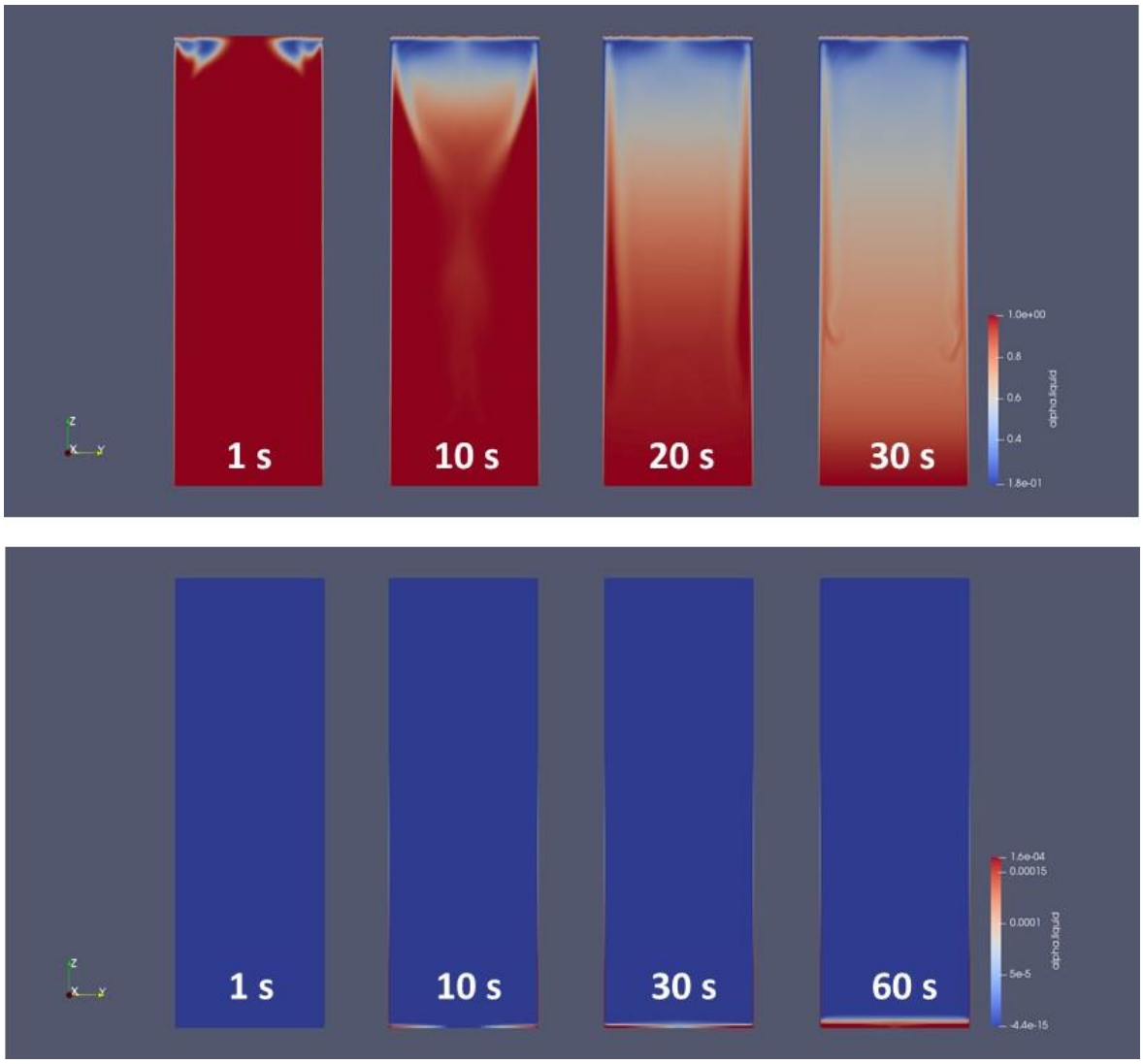

Figure 43. Liquid void fraction result of the simply phase change simulation

5.1.4 Problems of Standard Solver

There may be a severe malfunction in the interface while capturing the features of the solver because no bubbles and droplets appeared; only weird mixing was observed between the liquid and the vapor. Therefore, the performance of interface used for

capturing data was tested to identify problems inside the interface using isothermal rising bubble simulations.

Numerical diffusion of the interface

Problems with the standard solver related to interface capturing that cause the interface to diffuse were observed. The diffusion problem prevented bubbles generated by the phase change near the wall from traveling inside the water phase. Instead, they just spread and mix into the water, which physically does not make any sense. Further, surface tracking and interface sharpening seem to work poorly although they are the most characteristic parts of the current solver. Therefore, the reason this solver cannot maintain the interface needs to be investigated in this study.

Comparative Study of Solvers

Several simplified simulations are performed based on the analytical understanding of interface tracking and the reconstruction method to identify the reason for the phase mixing (or interface diffusion) problem. The current solver, *iCEF* is scrutinized as the first step.

The solver uses the color-function VOF (CF-VOF) as an interface reconstruction method. This method introduces artificial compression terms to the conservation equation of the void fraction to offset the numerical interface diffusion. OpenFOAM uses a multidimensional universal limiter with explicit solution (MULES) as a method to solve this form explicitly (STAR CCM+ uses High-Resolution Interface Capturing

(HRIC) instead). The method is the implementation of a flux-corrected transport scheme (FCT) theory, and it is used to solve a transport equation by employing an explicit universal multidimensional limiter. This method works well in the case of the slow-moving liquid body (or Co < 0.1), but has limited performance for a gas moving with high velocity (Roenby et al., 2016).

iCEF shares the same VOF model with the *interFoam* solver, which is an interface solver provided by OpenFOAM (it can be easily guessed from its name). The only difference is that it has an additional feature of solving phase change caused by heat transfer. Therefore, a simulation of an isothermal rising bubble case has been solved by both solvers to identify the origin of the diffusion problem.

In the two-dimensional 100 × 300 space, a square bubble with 20 × 20 mm of dimension is initially located at 20 mm above the bottom. The 100 × 300 uniform hexagonal mesh is set for the calculation. The kinematic viscosity of the liquid phase is set to be $2.940 \times 10^{-7} m^2/s$, while that of steam is set to be $2.051 \times 10^{-5} m^2/s$. The surface tension between the two phases is $0.0589\ N/m$.

The result of the isothermal rising bubble simulation using *iCEF* is shown in Figure 44. Although the phase change is not included for the simulation, the weird mixing of bubbles with liquid can be observed. An interesting point is observed in the result of the *interFoam* simulation shown in Figure 45. The bubble seems to rise properly, which causes wakes in their tails and leaves scattered small bubbles behind it. From the comparison of the two different results, we can conclude that the *iCEF* solver

has certain problems related to the interface capturing features and those problems are not related to the same features of *interFoam.*

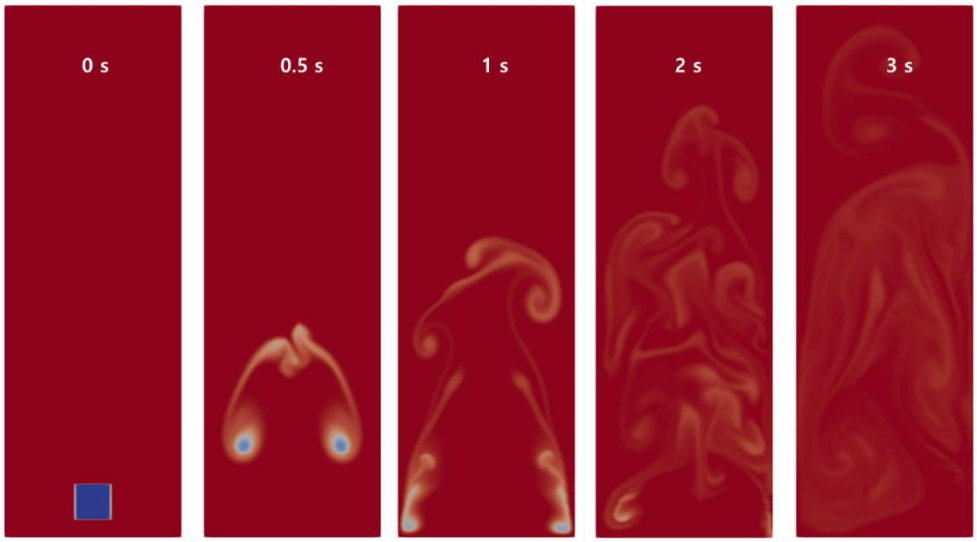

Figure 44. Isothermal rising bubble simulation using iCEF

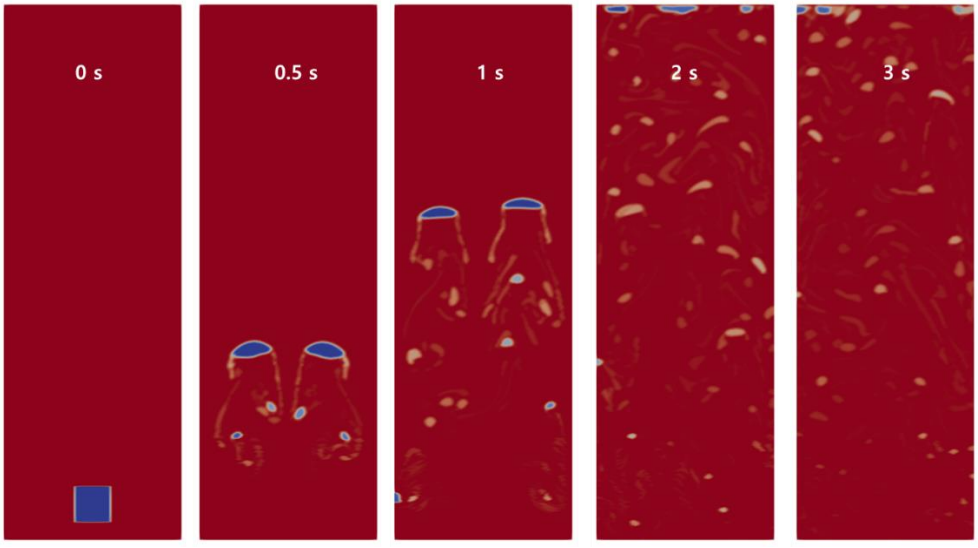

Figure 45. Isothermal rising bubble simulation using interFoam

Effect of Viscosity and Mesh Size

The rising bubble simulation has been studied by numerous researchers as a validation case of a two-phase flow solver. Hysing et al. (2009) published a pure numerical benchmark for a 2D rising bubble simulation. The material properties of the benchmark simulation setup are summarized in

Table 9. The *interFoam* solver has already been validated using the same set of conditions because it is a general interface solver. The primary difference between the test set used in section 2.5.2, and the benchmark test set is the value of viscosity. Therefore, the same value of the viscosity with the benchmark data is set for *iCEF* to identify that the solver can maintain the interface.

Table 9. The material properties of the cases

Case	$\boldsymbol{\rho_1}$ $[\boldsymbol{kg/m^3}]$	$\boldsymbol{\rho_2}$ $[\boldsymbol{kg/m^3}]$	$\boldsymbol{v_1}$ $[\boldsymbol{m^2/s}]$	$\boldsymbol{v_2}$ $[\boldsymbol{m^2/s}]$	g $[\boldsymbol{m/s^2}]$	$\boldsymbol{\sigma}$ $[\boldsymbol{N/m}]$
Benchmark	1000	1	10^{-2}	10^{-1}	0.98	1.96
Test set in 2.2	958.34	0.5984	2.940×10^{-7}	2.051×10^{-5}	9.81	0.0589

The result of the high viscosity rising bubble simulation is shown in Figure 46. The diffusion of the interface can be identified in this result. There is no scattering of the bubble, and the rate of weird mixing occurs at a lower rate because of the high viscosity. However, the shape of the bubble is distorted because of the mixed region at the tail of the bubble. This result helps us conclude that the viscosity does not affect the diffusion problem of the solver because the problem appears in both high and low viscosity simulations.

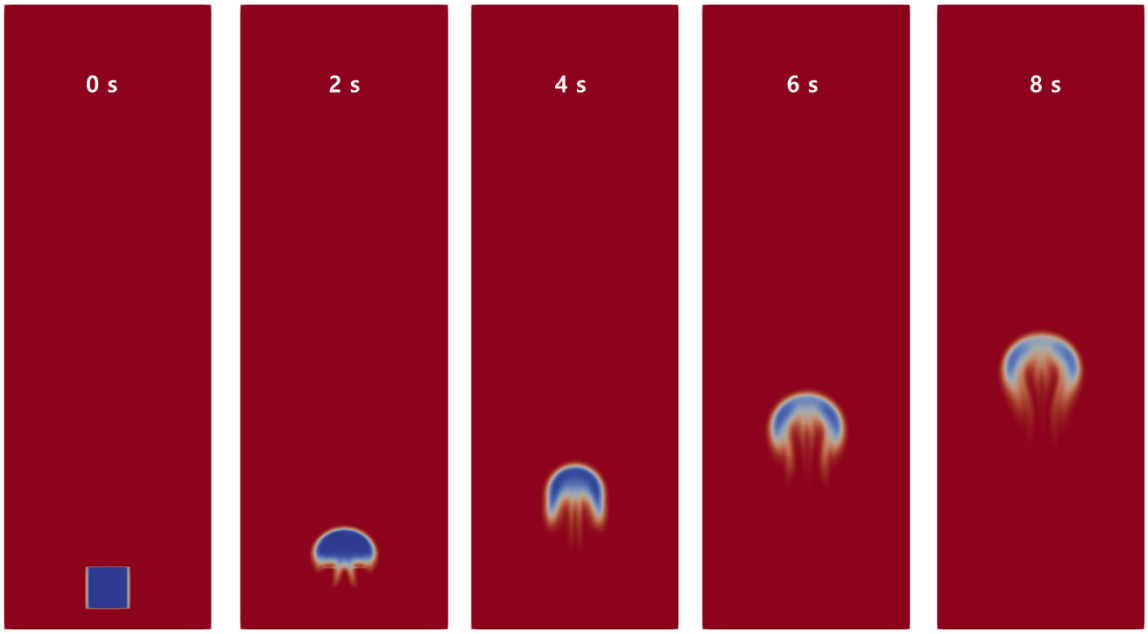

Figure 46. The result of high viscosity rising bubble simulation

The effect of the size of the mesh to the diffusion of the interface is also checked. In most studies related to the motion of the bubble, the adaptive mesh method is ensure that the size of the mesh near the interface is as small as possible. This implies the importance of the mesh size to calculate the force and mass balance at the interface, which is extremely complex. Therefore, a fine grid (100 × 600) is tested to observe the effect of the mesh size on the diffusion of the interface.

Figure 47 presents the result of the rising bubble simulation in the fine mesh condition. The solver does not work well and shows the same problem although the size of the mesh was doubled. Therefore, it is safe to conclude that this problem does not have any mesh sensitivity.

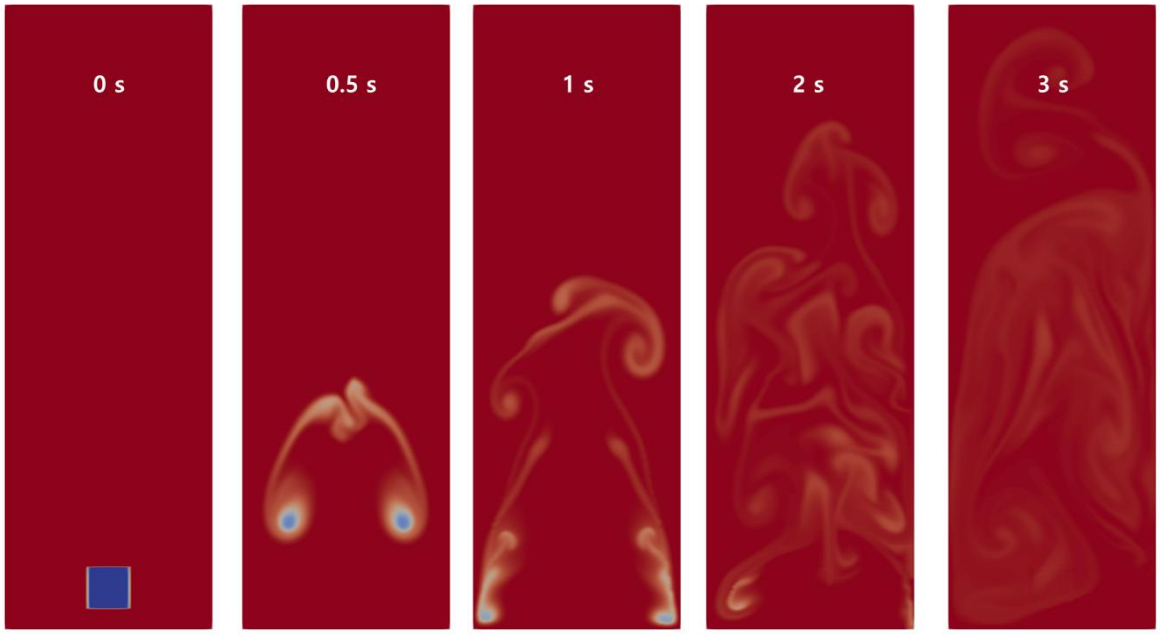

Figure 47. The result of rising bubble simulation in the fine mesh

5.2. Development Of Phase Change Solver

In this section, solvers are modified and build to overcome the problems specified in the previous section.

5.2.1 Rising Bubble Benchmark Case

Islam et al. (2020) reported using a single rising bubble benchmark case. Since it is one of the most recently introduced works related to the verification of the interface solver, it was adopted as a benchmark case in this study.

Mesh and Boundary Conditions

Based on the information given in the paper (Islam et al., 2020), a mesh size of 0.20 mm was selected in this study; it created 1 × 179 × 537 nodes for 0.2 × 35.71 × 107.14 mm of the simulation domain. Initially, a bubble with 2.5 mm of diameter was

located at 11.25 mm above the bottom. Dimensions of the square domain were determined based on the diameter of the bubble; the domain width, 2.5/0.07 mm, was used to minimize the wall effect. The height of the domain was set to be 3× the width.

Three different properties of fluids were used to catch the effect of different Molton (Mo) numbers. Table 10 represents the properties used in this study in detail.

Table 10 Properties of the fluid for the rising bubble simulation

Cases	Density $[kg/m^3]$	Viscosity $[kg/m \cdot s]$	Surface tension $[N/m]$	Mo $[-]$
1	1183.8	0.0060	0.0745	2.67×10^{-8}
2	1222.6	0.0114	0.0786	2.82×10^{-7}
3	1308.4	0.1066	0.0812	1.80×10^{-3}

Solver Setup

Turbulent modeling was not adopted to conduct a laminar simulation. The minimum time step of 10^{-4}s was set for 1 s of the total simulation time. An adjustable time step option was applied using the maximum Courant number of 0.25 as a control criterion. The PIMPLE method was applied as the pressure-velocity coupling method. The implicit Euler scheme was used as a time derivative, while the Gauss linear and upwind schemes were used to calculate gradient and divergence.

5.2.2 interCondensatingEvaporatingFoam_MULES

The first step of building a solver that can simulate two-phase flow, which includes phase change, includes finding and fixing problems with the original standard solver. This work mostly focused on the interface capturing of the solver because *interCondensatingEvaporatingFoam* showed no such features at all. The structure and contents of source code were thoroughly explored to modify the solver and fix the problem.

Solver Implementation

In the script of *interCondensatingEvaporatingFoam.C*, users can easily find the PIMPLE loop, which is not only the time-pressure coupling method but the main iteration for the time marching of the simulation. As indicated in Figure 48, there are three governing equations inside the loop that are the continuity equation (*alphaEqn.H*), momentum equation (*UEqn.H*), and energy equation (*TEqn.H*). As the loop starts, the advection of the volume fraction (α) is solved first using the header, *alphaEqn.H*. Then, the code updates the density and viscosity with a new liquid volume fraction value at each cell, and the flux value for the finite volume method (ϕ) is reconstructed. The momentum (*UEqn.H*) and energy equations (*TEqn.H*) are solved numerically using this updated value. The pressure corrector loop is the final step of the single time iteration, and it moves to the next time step starting with *alphaEqn.H*.

Figure 48. PIMPLE loop of *interCondensatindEvaporatingFoam.C*

There are indeed problems in the solving interface in this solver. In the solver, parameters related to the interface are defined and handled by the class, “interface.” Like in other CFD solvers, the surface tension is modeled as continuum surface force in OpenFOAM. In the model, the curvature of the interface is calculated from the distribution of the void fraction, and therefore, to identify where the interphase exists between two fluids, the continuity equation needs to be solved correctly. That is, the problem of the solver can be attributed to the header *alphaEqn.H* or the code related to it.

The modification of the standard solver is presented in Figure 49. As mentioned above, the problem is found in the step of calculating the continuity equation, which updates the information of the void fraction according to the boundary conditions. On the left side of the figure, *alphaEqnSubCycle.H* is the script where the calculation for the void fraction is performed. However, there is no update of the interface parameters after the calculation. Instead, it directly moves to the step of the momentum and energy conservation equations. Therefore, a line is added after the continuity equation to ensure that the solver update parameters of interface class appear on the right side of the figure. A new solver was thus designed by modifying the PIMPLE loop. The solver was named as *interCondensatingEvaporatingFoam_MULES*, because the MULES algorithm of the OpenFOAM now works well after the modification.

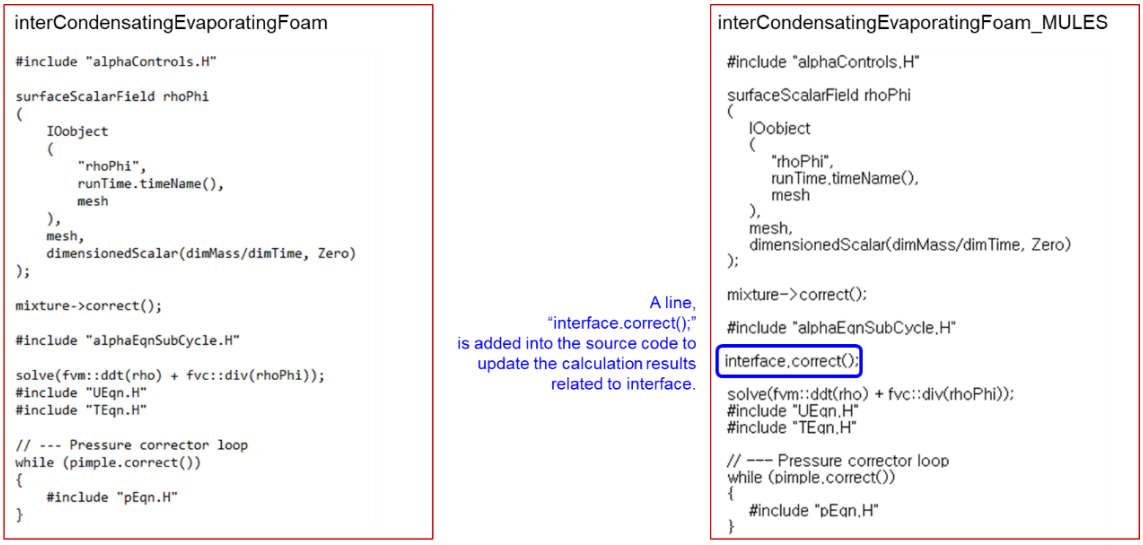

Figure 49. Modification of *interCondensatindEvaporatingFoam.C*

Result of Rising Bubble Simulation

Figure 50 presents the result of the rising bubble simulation performed using *interCondensating-EvaporatingFoam_MULE*. The result of the rising trajectory from the paper (Islam et al., 2020) is shown for the comparison on the left side of the figure. The result shows similar changes in the rising trajectory of bubbles according to their Mo number. A bubble with the largest Mo number of 1.80e-03 moves slowly upward and shows almost no zig-zag motion. A similar pattern of rising can be observed with a bubble with an intermediate Mo number; however, it shows the highest rising velocity among all cases. The smallest Mo number case (2.67e-08) has almost the same pattern and trajectory with the case from the paper.

Although the solver is using the standard method provided by OpenFOAM, some discrepancies were found especially for large Mo number cases. The bubble with the largest Mo number (1.80e-03) showed a much slower velocity than the one from the paper. Furthermore, the zig-zag motion of the 2.82e-07 case is too timid when compared to that presented in the paper. Therefore, there seems to be a further requirement of investigation in terms of both the reliability and sensitivity of the method.

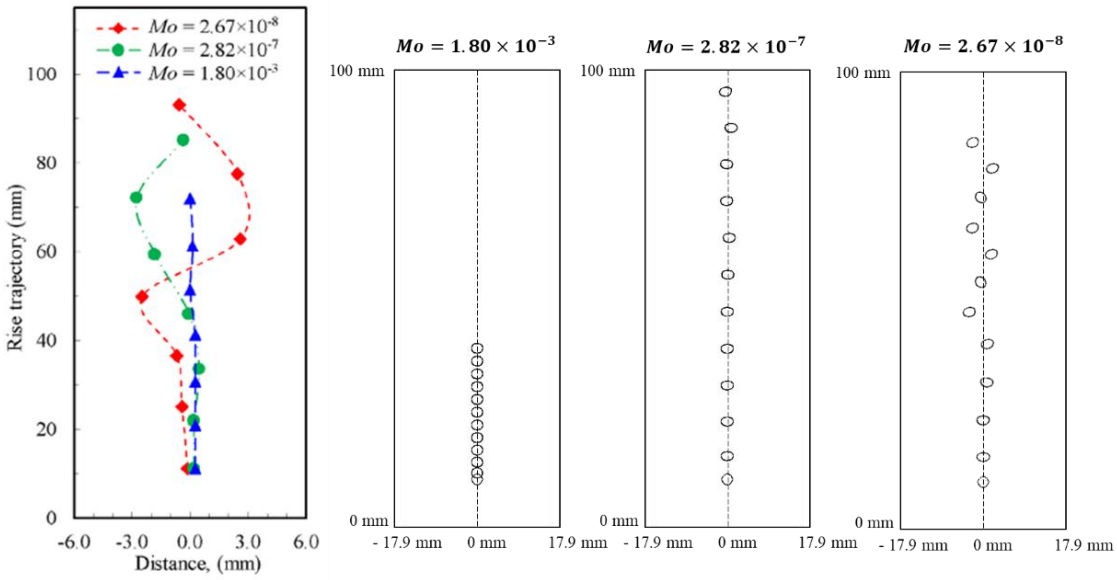

Figure 50. Result of the rising bubble using *interCondensatindEvaporatingFoam_MULES*

5.2.3 isointerCondensatingEvaporatingFoam

MULES is an algebraic VOF method that adds an artificial compression term in the continuity equation. It is widely used because of the simplicity of its implementation and efficiency. However, the method is based on a considerably more heuristic assumptions, and it is not as accurate as other schemes (Roenby et al., 2016). The geometric VOF scheme shows better performance from the viewpoint of accuracy; however, it requires complex geometric operations, which increase the cost of the simulation (Roenby et al., 2016). Since the goal of this study is to simulate complex and rapid two-phase flow inside the heat pipe, the iso-advector scheme, which is a widely used geometric VOF scheme, was applied to the phase-change simulation.

Solver Implementation

The iso-advector scheme has already been implemented into one of the OpenFOAM solvers, *interIsoFoam*. However, it has no features of solving the phase change yet. Therefore, the solver was merged with interCondensatingEvaporatingFoam to develop a new solver.

As mentioned in the section above, issues related to the interface are handled inside of the continuity equation. The *interIsoFoam* uses an "advector" class, which calculates and updates void fraction using the iso-advector scheme inside "*alphaEqn.H,*" as shown in Figure 51. Based on the structure of the solvers, the role of the header file, "*alphaEqn.H,*" is expected to be the same for all VOF solvers of OpenFOAM. Therefore, for the implementation of the iso-advector scheme to the phase-change solver *interCondensatingEvaporatingFoam*, the header file "*alphaEqn.H,"* was changed to the one of *interIsoFoam.*

```
{
    // Temporarily making U relative to mesh motion
    if (mesh.moving())
    {
        U -= fvc::reconstruct(mesh.phi());
    }

    // Updating alpha1
    advector.advect();

    // Making U absolute again after advection step
    if (mesh.moving())
    {
        U += fvc::reconstruct(mesh.phi());
    }

    #include "rhofs.H"
    rhoPhi = advector.getRhoPhi(rho1f, rho2f);

    alpha2 = 1.0 - alpha1;
    mixture.correct();
}

Info<< "Phase-1 volume fraction = "
    << alpha1.weightedAverage(mesh.Vsc()).value()
    << "  Min(" << alpha1.name() << ") = " << min(alpha1).value()
    << "  Max(" << alpha1.name() << ") = " << max(alpha1).value()
    << endl;
```

Figure 51. alphaEqn.H of interIsoFoam.C
Result of Rising Bubble Simulation

Figure 52 shows the result of the rising bubble simulation using *isointerCondensatingEvaporatingFoam*. The result of the rising trajectory from the paper (Islam et al., 2020) is shown for the comparison on the left side of the figure. A bubble from the Mo number of the 1.80e-03 case moves slowly upward and shows almost no zig-zag motion. A bubble with faster movement and a more zig-zag motion can be observed in an intermediate Mo number case. The smallest Mo number case (2.67e-08) shows a similar velocity with the intermediate case with a slightly wider horizontal movement.

The overall movement of bubbles showed less discrepancy with the data from the paper comparing to the result of *interCondensatingEvaporatindFoam_MULES* except for the smallest Mo number case. The case with 1.80e-03 of Mo number case shows a much slower resting velocity than the benchmark data. The bubble with the smaller Mo numbers (2.82e-07, 2.67e-08) showed better agreement with the data when their velocity and trajectory were compared.

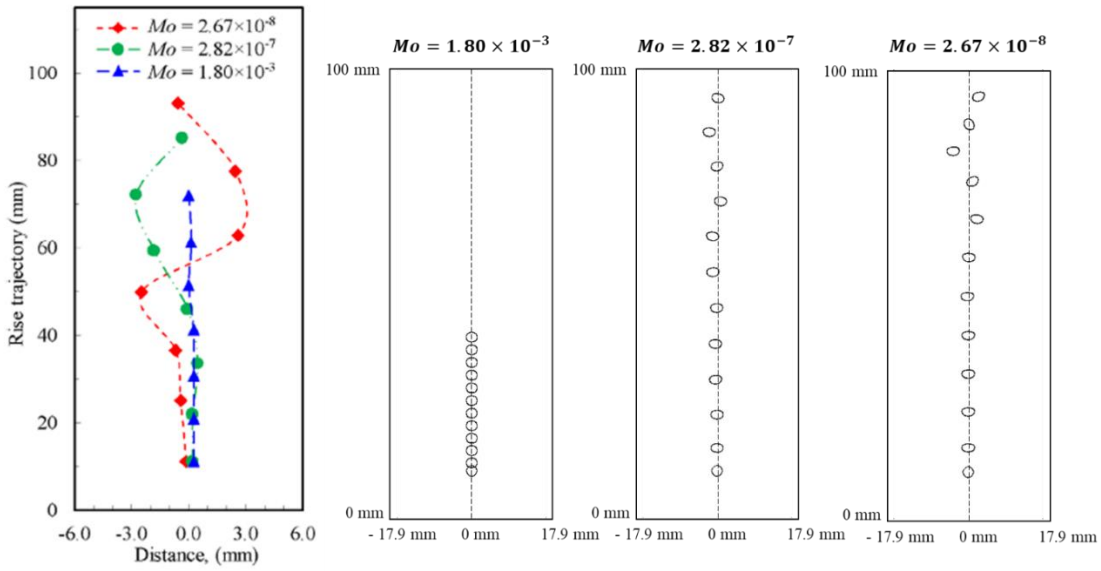

Figure 52. Result of the rising bubble using isointerCondensatindEvaporatingFoam

5.3. Investigation Of Phase Change Model

An investigation of the phase change model was conducted to check the capability of simulating phase change inside a heat pipe. Several phase change models have been proposed for the VOF (Chen et al., 2020) including the Lee, energy jump, Schrage, and some new models such as the Chen and Sun models.

Among these models, the Lee model is the simplest one, which calculates the source terms of the continuity equation using the deviation between the interfacial temperature and the saturation temperature. Owing to its simplicity, the model is studied and used widely. Recently suggested models such as the Chen and Sun models use thermal properties of the fluid, distribution of void fraction, and temperature. These two models do not use empirical constants, which can greatly benefit the application. Therefore, the performance of three models is evaluated and investigated using benchmark cases in this study.

5.3.1 Simulation Setup for the Benchmark Case

The Stefan problem and two-dimensional film boiling simulation are selected as a benchmark case in this study because they are the most widely used instances to check the performance of phase change solver with a clear and straightforward analytical solution.

Stefan Problem

A Stefan problem was solved using OpenFOAM as a benchmark case of the phase-change model. The Stefan problem is a boundary value problem adapted for the case with a moving phase boundary. A one-dimensional Stefan problem was solved in this study, and the location of the interface was used as an indicator of the verification.

Mesh and Boundary Conditions

The geometry and mesh structure of the one-dimensional Stefan problem are shown in Figure 53. The uniform mesh size of 2 μm was set, and the length of the computational domain was 1 mm; 500 meshes were generated in total.

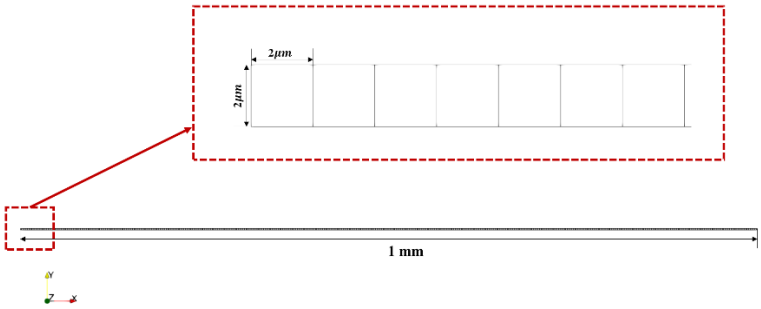

Figure 53. The geometry and the mesh structure of the one-dimensional Stefan problem

The initial setup of the void fraction of the liquid phase and temperature is shown in Figure 54. Initially, a thin vapor film with the thickness of a single mesh size was attached to the wall on the left side. The void fraction of the second cell was 0.5 because of the laminar increase in the liquid void fraction from 0 to 1; it was considered as an

initial interface. The temperature of the wall is 10 K larger than the saturated liquid phase temperature.

The wall condition is imposed at the left end while the outlet condition is set at the opposite end. Since OpenFOAM provides only three dimensions, the geometry is designed in a three-dimensional format at the start point; empty conditions are patched to walls at y and z directions to simulate the one-dimensional problem.

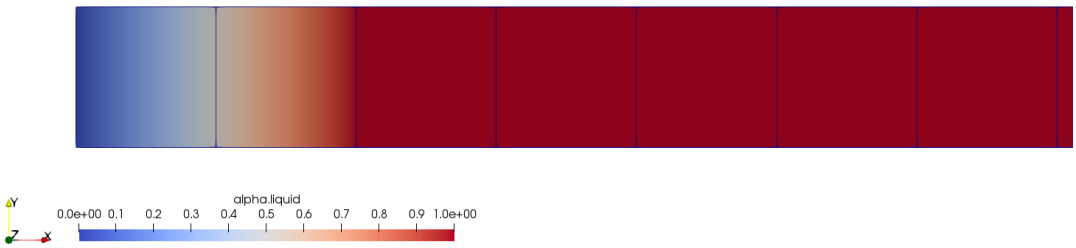

(a)

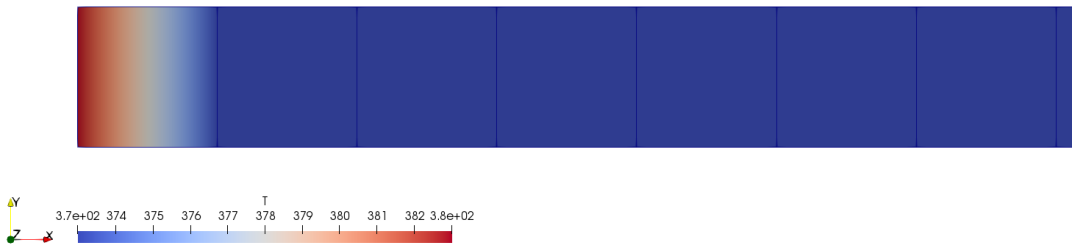

(b)

Figure 54. The initial distribution of (a) void fraction, (b) temperature of the Stefan Problem

Properties of water and vapor at 101.3 kPa were used in this benchmark case. The values of properties are listed in Table 11 in detail.

Solver Setup

A laminar option is set to prevent using any turbulent modeling in this study. The minimum time step of 10^{-7}s was set, and it was adjusted by the maximum Courant number of 0.1. The PIMPLE method was used as a pressure-velocity coupling method, and the implicit Euler scheme was used as a time derivative. The Gauss linear and upwind schemes were used to calculate the gradient and divergence.

Table 11. Properties of water and vapor at 101.3 kPa

	Density $[kg/m^3]$	Viscosity $[kg/m \cdot s]$	Heat capacity $[J/kg \cdot K]$	Thermal conductivity $[W/m \cdot K]$	Latent heat $[J/kg]$	Surface tension $[N/m]$
Vapor	0.597	1.26e-05	2030	0.025	2.26e06	0.059
Liquid	958.4	2.8e-04	4216	0.679		

Two-Dimensional Film Boiling

Two-dimensional film boiling is one of the most widely used benchmark cases for the phase change simulation. In this approach, the bottom of the simulation domain is heated with a higher temperature than the saturation temperature of the fluid. The position of bubbles generated by the phase change is set to the center of the domain by controlling the shape of the initial vapor film at the bottom. The verification can be confirmed by checking the Nusselt (Nu) number at the bottom wall and by comparing it with the analytical solution suggested by Klimenko (Klimenko, 1981).

Mesh and Boundary Conditions

The axisymmetric domain was set with 0.07868 m width and 0.11802 m height. The size of the domain was determined based on the "most dangerous" Taylor wavelength. A uniform mesh (80 × 240) configuration was used for the calculation. Initially, the bottom of the domain was filled with steam, and the interface shape was set according to

$$y(x,0) = \frac{0.07868}{128}\left[4.0 + cos\ \left(\frac{2\pi x}{0.07868}\right)\right]. \qquad Eq\ 4$$

A no-slip condition and a superheated temperature of 5 K was set for the bottom wall. The wall at the left side was set to an axis, and a free-slip condition was imposed on the right wall. Further, the top wall was considered as an outlet, and therefore, a pressure-outlet boundary condition was set. Initially, the liquid was saturated, and the temperature of the vapor film at the bottom was set to decrease linearly from the bottom wall to the interface. The initial distribution of the void fraction and temperature is shown in Figure 56.

The liquid and vapor were considered incompressible fluids, and their detailed properties are listed in Table 12.

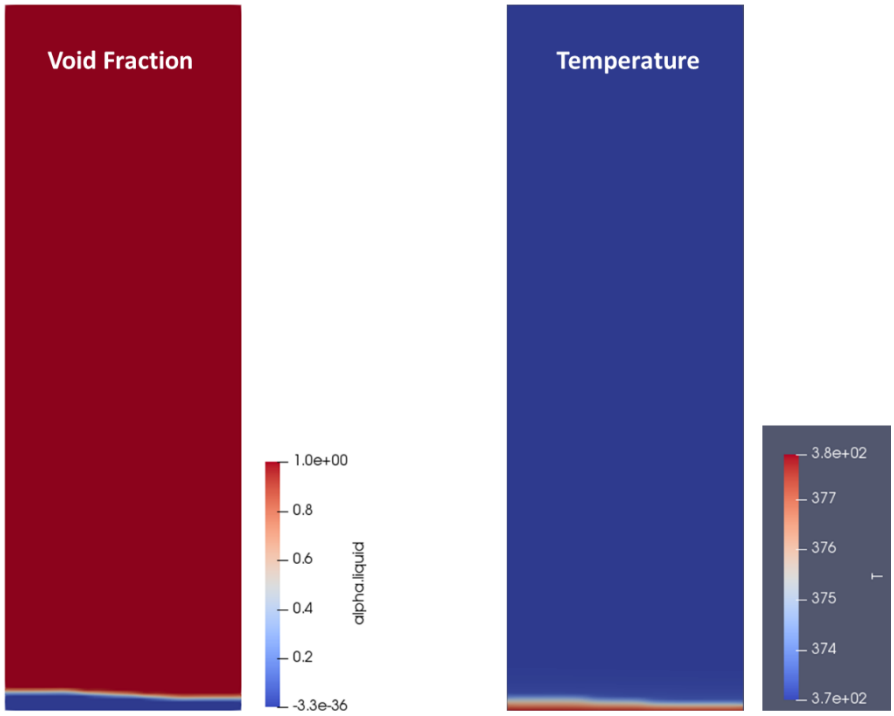

Figure 55. The initial distribution of the void fraction (left), the temperature (right)

Table 12. The properties of liquid and vapor for 2D film boiling problem

	Density $[kg/m^3]$	Viscosity $[kg/m \cdot s]$	Heat capacity $[J/kg \cdot K]$	Thermal conductivity $[W/m \cdot K]$	Latent heat $[J/kg]$	Surface tension $[N/m]$
Vapor	5	0.005	200	1	10000 & 100000	1
Liquid	200	0.1	400	40		

Solver Setup

No turbulent modeling was adopted to conduct a laminar simulation. The minimum time step of 10^{-6}s was set with an adjustable time-step option. The time step

was controlled by the maximum Courant number of 0.1, and the rest of the setting was set similarly to that in the one-dimensional Stefan problem. All other conditions were the same as that in the Stefan problem.

5.3.2 Lee Model

As mentioned above, the Lee model is one of the most widely used models because of its simplicity and other benefits. In the model, the source term of the mass conservation equation is defined as

$$S_v = \beta_e \alpha_l \rho_l (T - T_{sat}), \quad S_c = \beta_c \alpha_v \rho_v (T - T_{sat}) \qquad Eq\ 5$$

where β_e and β_v represent the mass transfer intensity factors (1/s). The model can simulate phase change without a predetermined phase interface because it only uses the deviation between the interfacial and saturation temperatures. It is suitable not only for saturated boiling but also for subcooled boiling; further, convergence control is relatively easy. However, the empirical constants and mass transfer intensity factor should be adjusted in the excessively wide range, which can cause limitations to apply the model under various scenarios. Based on these ideas, the Lee model with multiple values of mass transfer intensity factor was tested in the benchmark case.

Result of the Stefan Problem

Figure 56 represents the result of the Stefan problem using the Lee model. The simulation was conducted using three values of the mass transfer intensity factors (100,

1000, and 10000). Even though the value 0.1 is the most widely used value for the boiling case, it was excluded in this study because it caused an unstable and inaccurate result. The speed of the moving interface decreases as the value of constant increases. The simulation result showed the best agreement when the value of the constant was set to 100.

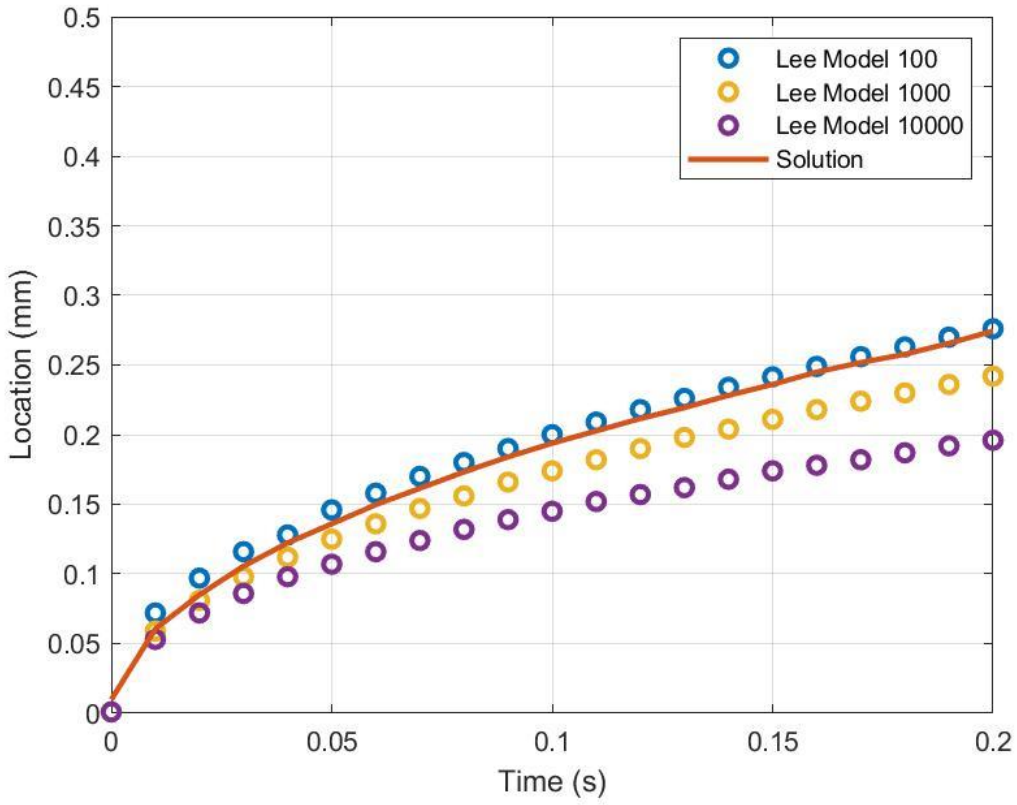

Figure 56. The result of the Stefan problem simulation using Lee Model

Result for Two-Dimensional Film Boiling

The result of the 2-D film boiling simulation using the Lee model is shown in Figure 57. The mass transfer intensity factor was set to 0.1 for both $h_{fv} = 10^4\ [j/kg]$

and 10^5 $[j/kg]$. As shown in the figure, the averaged Nu number shows good agreement with theoretical solutions. For the $h_{fv} = 10^4$ $[j/kg]$ case, the value of Nu number is 11.50, which has a 4.20 % of error with the Klimenko correlation, whereas the Nu number of the $h_{fv} = 10^5$ $[j/kg]$ case is 23.81 with a deviation of 8.03%.

The characteristics of the Lee model can be found based on the results of the Stefan problem and 2-D film boiling simulations. Owing to its simple structure and straight forward theoretical background, it is easy to obtain reasonable results for both benchmarks. However, the mass transfer intensity values applied to obtain those results were different. This implies that the value of the mass transfer intensity should be selected considering the types of phenomena inside of the simulation domain. This can be critical if multiple, complex phenomena are to be simulated.

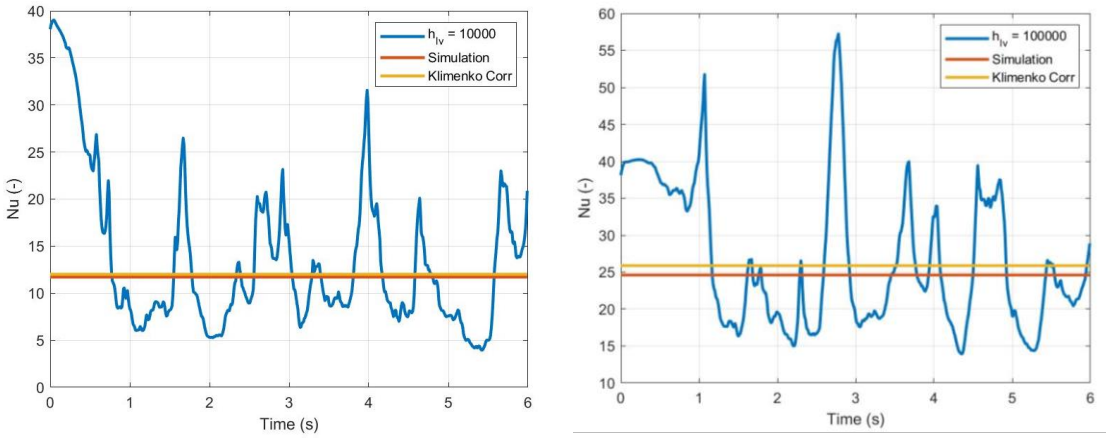

(a) (b)

Figure 57. The result of the 2-D film boiling simulation using Lee Model, (a) $h_{fv} = 10^4$ $[j/kg]$, (b) $h_{fv} = 10^5$ $[j/kg]$

5.3.3 Chen Model

Chen et al. (Chen et al., 2020) suggested a new model for the mass transfer intensity factor based on the physical process of heat transfers in the numerical domain as

$$S_v = \frac{1}{(0.5 + 0.5\alpha_l)\alpha_l} \frac{k_l}{h_{lv}\rho_v \Delta x} \frac{A_{int}}{V} \alpha_l \rho_v (T - T_{sat}) \qquad Eq\ 6$$

They evaluated the accuracy of their model by simulating a one-dimensional Stefan problem and a two-dimensional film boiling problem. Even though the results showed good performance in the paper, the simulation was conducted using a commercial program, ANSYS. Therefore, the Chen model was implemented into the OpenFOAM environment in this study, and its performance was tested using two benchmark cases.

Solver Implementation

Solvers developed in this study are based on the standard solver, *interCondensatingEvaporatingFoam*. The solver is built to simulate the phase-change using the Lee model. It is relatively more comfortable to add the model into the solver because the Chen model was suggested considering the structure of the Lee model.

The strategy of the implementation is straight forward. There are some constants based on properties of fluids ($k_l, h_{lv}, \rho_l, \rho_v$). Further, geometric parameters such as $\frac{1}{\Delta x}$

and $\frac{A_{int}}{V}$ can also be considered as constant parameters if a uniform mesh sized is assumed. Therefore, if the mass transfer intensity (β_E, β_c) is defined as

$$\beta_E = \frac{k_l}{h_{lv}\rho_v \Delta x}\frac{A_{int}}{V}, \beta_c = \frac{k_v}{h_{lv}\rho_{v\Delta x}}\frac{A_{int}}{V} \qquad Eq\ 7$$

only the rest of the part,

$$\frac{1}{(0.5 + 0.5\alpha_l)\alpha_l} \qquad Eq\ 8$$

needs to be implemented inside the source code.

As mentioned above, three conservation equations are solved numerically inside of the PIMPLE loop. There are source terms of mass conservation equation declared as vDotcAlphal and vDotvAlphal in alphaEqn.H and TEqn.H. Further, the source terms are defined as mDotc and mDotv in pEqn.H. In front of those source terms, the multiplication of Eq 8 was coded, as shown in Figure 58. The modified code was encoded with the solver name *interCondensatingEvaporatingFoam_Chen.*

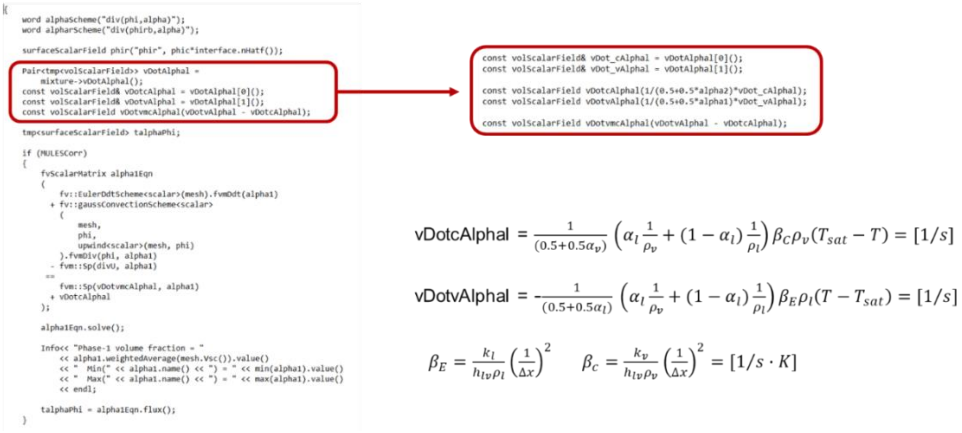

Figure 58. Implementation of the Chen model into OpenFOAM

Result of Stefan Problem

Figure 59 shows the result of the Stefan problem using the Chen model. The mass transfer intensity factor was calculated as 78.32 and applied to the input file phaseCahngeProperties.C. The speed of the moving interface almost overlapped with the theoretical solution.

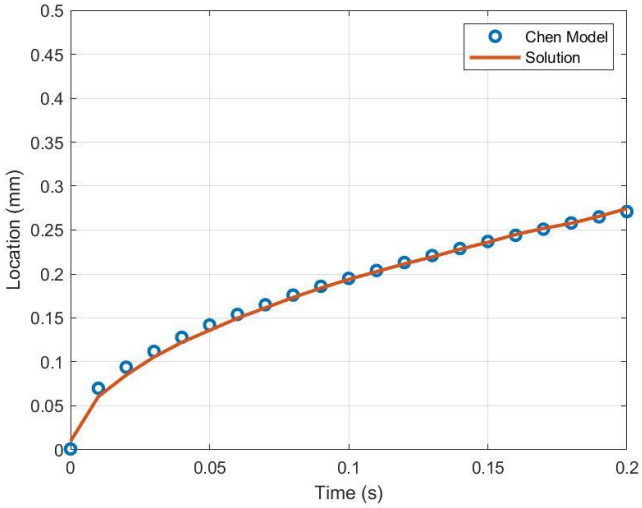

Figure 59. The result of the Stefan problem simulation using Chen Model

Result of the Two-Dimensional Film Boiling

The result of the 2-D film boiling simulation using the Chen model is presented in Figure 60. The mass transfer intensity factor was calculated as 82.71 for the $h_{fv} = 10^4\ [j/kg]$ case and 8.27 for the $10^5\ [j/kg]$ case. The result indicate that the steady-state of the flow pattern is achieved after 3.5 s of simulation time. Further, the pattern of the fluctuation of the Nu number did not follow the typical smooth curve even after it reached the steady state. The averaged Nu number was calculated with the data after 3.5 s, and it showed a relatively good agreement with theoretical solutions. For the $h_{fv} =$

10^4 $[j/kg]$ case, the value of Nu number is 13.41, which has an 11.66 % error with the Klimenko correlation, whereas the Nu number of the $h_{fv} = 10^5$ $[j/kg]$ case is 28.39 with a 9.69% deviation.

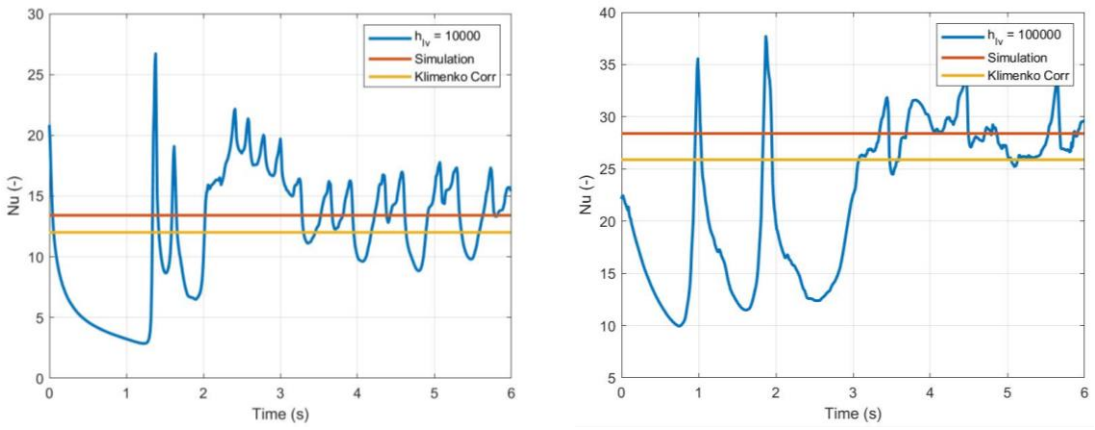

(a) (b)

Figure 60. The result of the 2-D film boiling simulation using Chen Model, (a) $h_{fv} = 10^4$ $[j/kg]$, (b) $h_{fv} = 10^5$ $[j/kg]$

5.3.4 Sun Model

Sun et al. (2012; 2014) suggested a model for the source term of continuity equation by explaining the interfacial heat flux jump using Fourier's law as

$$S_v = \frac{q'''}{h_{lv}} = \frac{2k_{uns}\nabla T \cdot \nabla \alpha_{uns}}{h_{lv}} \qquad Eq\ 9$$

The model can explain both unsaturated and saturated phase change, which is a strong advantage in the case of heat pipe simulation. In their paper, the model was verified using the Stefan problem and 2-D film boiling simulation, and the model was found to

be in excellent agreement with the analytical solutions. Since the model is not implemented in the OpenFOAM environment, building a solver with the model and verifying it with the same benchmark problems were conducted in this study.

Solver Implementation

Unlike the Chen model, the Sum model was built based on the configuration of the Lee model. Therefore, the input file to declare the mass transfer intensity factor was not required for the Sun model. Instead, the source term was declared and calculated only inside the header files for conservation equations, such as alphaEqn.H, pEqn.H, and TEqn.H. The implementation of the model into the alphaEqn.H is shown as an example in Figure 61. Source terms, vDotcAlphal and vDotvAlphal, are declared as volume scalar fields and calculated by multiplying and dividing multiple parameters. Below the calculation, a simple code was added for filtering the source term and the temperature from each cell and to block them from the non-physical value.

```
volVectorField gradAlpha1 = fvc::grad(alpha1);
volVectorField gradAlpha2 = fvc::grad(alpha2);
volVectorField gradT = fvc::grad(T);
volScalarField gradAlpha1_T = gradAlpha1&gradT;
volScalarField gradAlpha2_T = gradAlpha2&gradT;
dimensionedScalar kappa1 = thermo->kappa1();
dimensionedScalar kappa2 = thermo->kappa2();
dimensionedScalar hlv = thermo->Hf2() - thermo->Hf1();
dimensionedScalar rho1 = thermo->rho1();
dimensionedScalar rho2 = thermo->rho2();

volScalarField vDotcAlphal(-2*(1.0/rho1)*kappa1*gradAlpha1_T/hlv);
volScalarField vDotvAlphal(-2*(1.0/rho2)*kappa2*gradAlpha2_T/hlv);

forAll(vDotvAlphal, cellI)
{
    if ( (alpha1[cellI]>scalar(0.999)) && (T[cellI] > 373))
    {
            vDotvAlphal[cellI] = 0;
            T[cellI] = 373;
    }
}
```

Figure 61. Implementation of the Sun model into OpenFOAM

In the progress of the implementation, the change from the phase fraction to the volumetric generation rate was achieved by multiplying the specific volume of the vapor ($1/\rho_v$). In the standard solver, the volumetric generation rate attributed to the phase change is calculated by multiplying the alpha coefficient, which is defined as

$$\alpha_l \frac{1}{\rho_v} + (1-\alpha_l)\frac{1}{\rho_l} \qquad \textit{Eq 10}$$

However, multiplying the alpha coefficient may lead to errors if the interface is not sufficiently sharp. Furthermore, many previous studies adopt specific volume difference, instead of the alpha coefficient (Nabil & Rattner, 2016; Onishi et al., 2013; Rattner & Garimella, 2014). The specific volume difference between the vapor and the liquid is calculated as

$$\frac{1}{\rho_v} - \frac{1}{\rho_l} \qquad \textit{Eq 11}$$

In most liquid–gas phase change systems, including the water–steam case, the specific volume of the liquid has a considerably smaller value than the vapor, which is almost negligible. Therefore, $1/\rho_v$ was adopted instead of the alpha coefficient in this study, and the volumetric generation rate was calculated as

$$v_v = \frac{1}{\rho_l}\frac{2k_{uns}\nabla T \cdot \nabla \alpha_{uns}}{h_{lv}} \qquad \textit{Eq 12}$$

The same film boiling case was simulated by the Lee and Chen models to check the effect of using the specific volume of the vapor instead of the alpha coefficient.

Figure 62 presents the result of the Lee model simulation. Approximately 27 % of error from the theoretical solution was observed; when the averaged Nu was controlled by adjusting the mass transfer intensity factor, there is a high possibility to improve the gap. The flow pattern of the system was clearer and steadier when it was compared with the result obtained with the alpha coefficient shown in Figure 57.

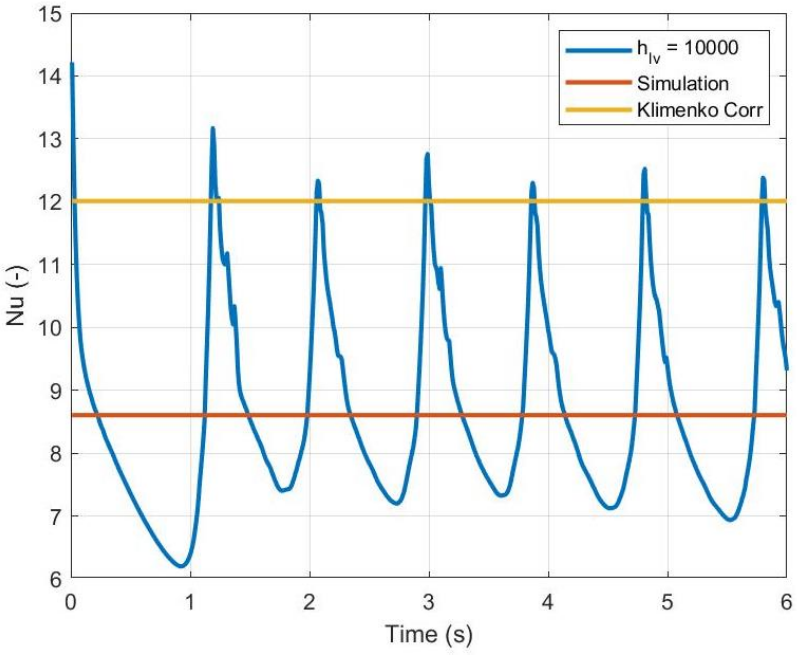

Figure 62. The result of the 2-D film boiling simulation using Lee Model with $1/\rho_v$

The improvement becomes clearer in the case of the Chen model. In Figure 63, the improved result of the film boiling simulation was observed when it was compared to the result shown in Figure 60. The Nu value oscillates regularly near the theoretical value and reaches a steady-state considerably faster than that in the previous result.

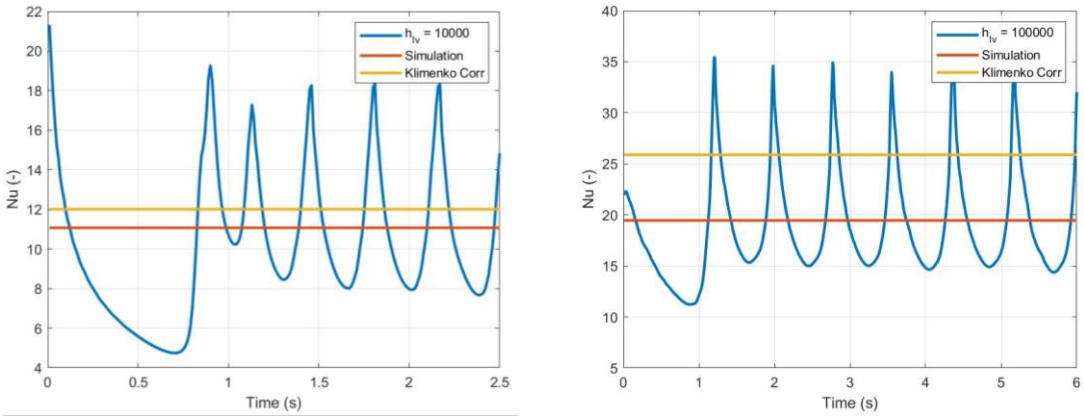

(a) (b)

Figure 63. The result of the 2-D film boiling simulation using Chen Model with $1/\rho_v$, (a) $h_{fv} = 10^4$ $[j/kg]$, (b) $h_{fv} = 10^5$ $[j/kg]$

Result of Stefan Problem

Figure 64 represents the result of the Stefan problem using the Sun model. It can be found that the speed of the moving interface follows the theoretical solution with only a small amount of deviation. The data were measured using the position of the cell with an approximated 0.5 of the void fraction. However, a highly diffused interface was observed. Since most phase change models including the Sun model were built under the assumption of a sharp interface, this highly diffused interface will hinder the reliability of the model. Therefore, there needs to be further investigation to identify why this occurs and why there is a difference in the result from the paper.

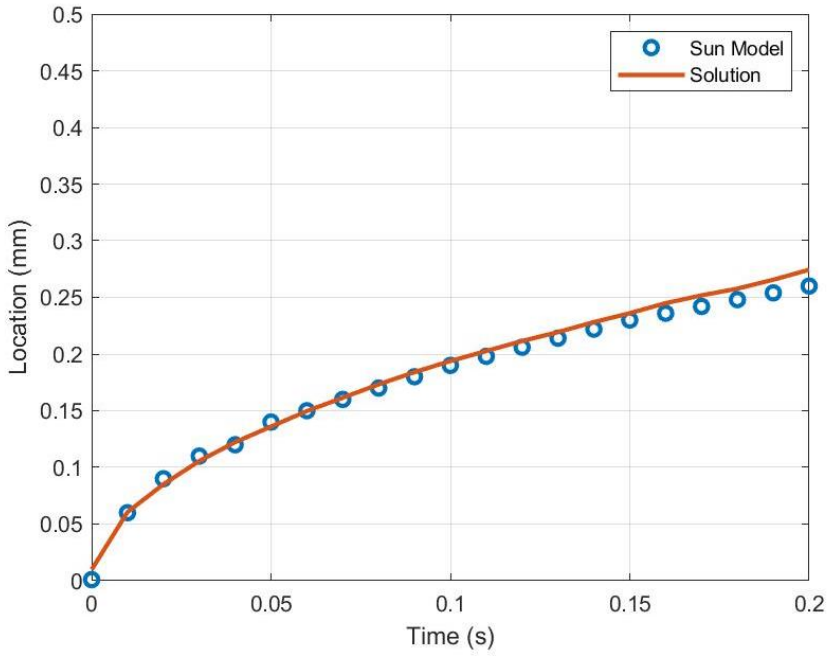

Figure 64. The result of the Stefan problem simulation using Sun Model

Result of Two -Dimensional Film Boiling

Figure 65 shows the simulation result of the two-dimensional film boiling case calculated using the Sun model. Only the result for the $h_{lv} = 100000$ case is presented because the $h_{lv} = 10000$ case showed large errors with non-physical flow patterns. From the figure, it can be found that the result shows a lower Nu value than the theoretical solution. Further, the flow did not maintain a periodical bubble rising, which resulted in the film disappearing because of the lack of evaporation.

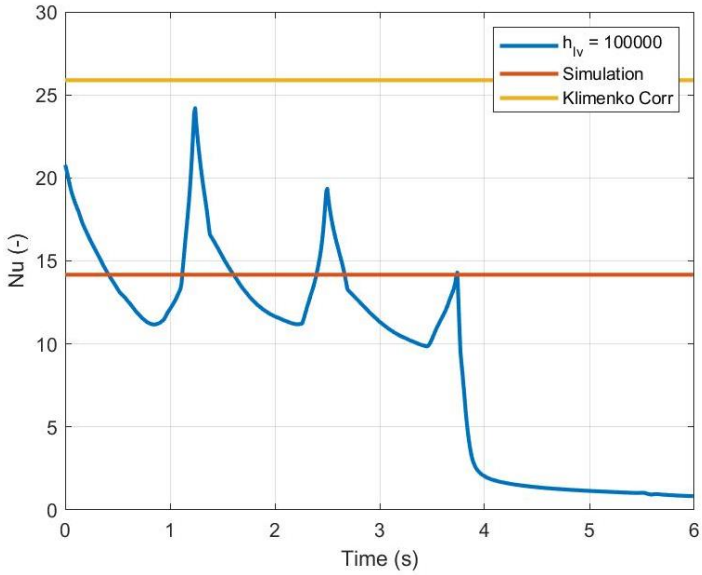

Figure 65. The result of the two-dimensional film boiling problem simulation using Sun Model

Since the initial setup of the Sun model showed a large discrepancy with the theoretical solution, investigations on the reason for the problem and modification of the solver were conducted. The investigation of the structure of the Sun model revealed that the gradient of phase fraction and temperature play a significant role in deciding the total volume change per unit time caused by the phase change. The volume change rate affects the value of Nu because the temperature difference between the superheated wall and the vapor is decided by the ratio of heat input rate to the mass transfer rate from the liquid phase to the vapor phase. Therefore, the main reason for the problems may be factors that affect the gradient value of the phase fraction and the temperature.

The interface sharpening scheme and mesh sensitivity were checked to confirm the effect of the gradient calculation. Since the theoretical background of the model assumes a sharp interface between liquid and vapor, the volume rate of the phase change

is different from the theoretical value if the interface is not sufficiently sharp. As mentioned above, the OpenFOAM provides the MULES algorithm to capture the interface between two phases. Users can control the number of iterations to enhance the interface capturing performance. Therefore, the total number of the iteration changed from 3 to 100 to check the effect of the scheme. Further, two grids with 160 × 480 and 240 × 720 of the number of mesh were set to investigate the mesh sensitivity. The gradient operator has a high sensitivity to the thickness of the interface, and the thickness may be affected by the size of the mesh.

The result of the calculation is shown in Figure 66. Both results present a different flow pattern from the one shown in Figure 65. The frequency of the rising bubble decreases with a decrease in the size of the mesh when the two different mesh sizes are compared. The value of Nu moves close to the theoretical solution as well. Thus, the Sun model has a high sensitivity to the calculation of the gradient operator at the interface, as indicated from this investigation. However, a firm conclusion cannot be obtained from these two results because the convergence of the sensitivity was not verified due to the limitation in computational power.

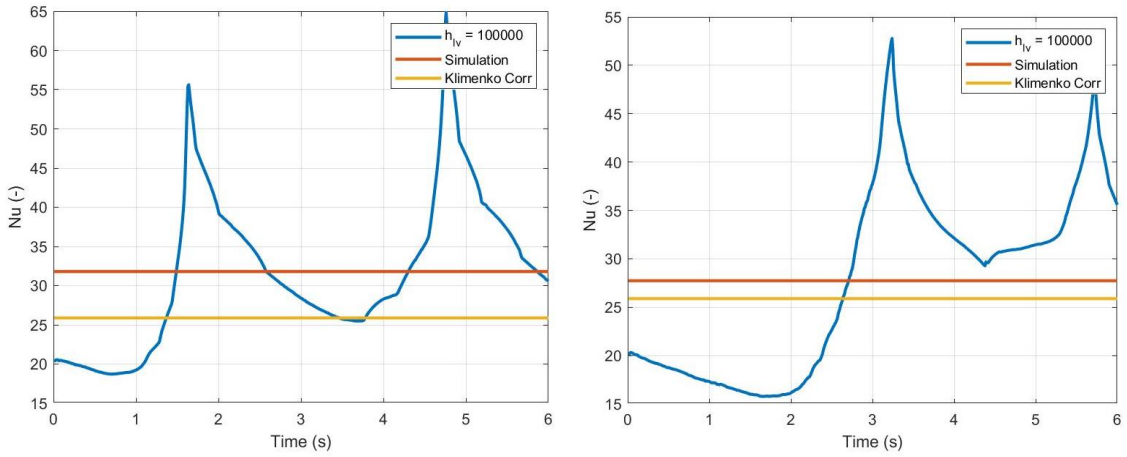

(a) (b)

Figure 66. The result of the 2-D film boiling simulation using Sun Model, (a) 160 x 480 mesh, (b) 240x720 mesh

Besides the value of the gradient terms, the sign was also considered in this study. Since the geometry of the simulation is not one-dimensional, a cell can have a negative value of $\nabla\alpha$ and ∇T with other adjacent cells. Therefore, a filter that can prevent the calculation of the reversed-phase change was applied, as shown in Figure 67.

```
volVectorField gradAlpha1 = fvc::grad(alpha1);
volVectorField gradAlpha2 = fvc::grad(alpha2);
volVectorField gradT = fvc::grad(T);
volScalarField gradAlpha1_T = gradAlpha1&gradT;
volScalarField gradAlpha2_T = gradAlpha2&gradT;
dimensionedScalar kappa1 = thermo->kappa1();
dimensionedScalar kappa2 = thermo->kappa2();
dimensionedScalar hlv = thermo->Hf2() - thermo->Hf1();
dimensionedScalar rho1 = thermo->rho1();
dimensionedScalar rho2 = thermo->rho2();

volScalarField alphalCoeff
(
    1.0/rho1 - alpha1
   *(1.0/rho1 - 1.0/rho2)
);

volScalarField vDotcAlphal(-0*2*1/rho1*kappa1*gradAlpha1_T/hlv);
volScalarField vDotvAlphal(-2*1/rho2*kappa2*gradAlpha2_T/hlv);

forAll(vDotvAlphal, cellI)
{
    if ( (alpha1[cellI]>scalar(0.999)) && (T[cellI] > 373))
    {
        vDotvAlphal[cellI] = 0;
         T[cellI] = 373;
    }
    if (vDotvAlphal[cellI]>0)
    {
        vDotvAlphal[cellI] = 0;
    }
}
```

Figure 67. The implementation of the filter inside of the PIMPLE loop.

Figure 68 shows the results of the simulation with the filter. There seems to be a considerable improvement in both the Nu value and the flow pattern, as indicated by the oscillation of the Nu value. The steady, regular, and periodic oscillation of the Nu value near the theoretical solution was achieved even though the averaged value of the Nu had an approximately 20 % discrepancy.

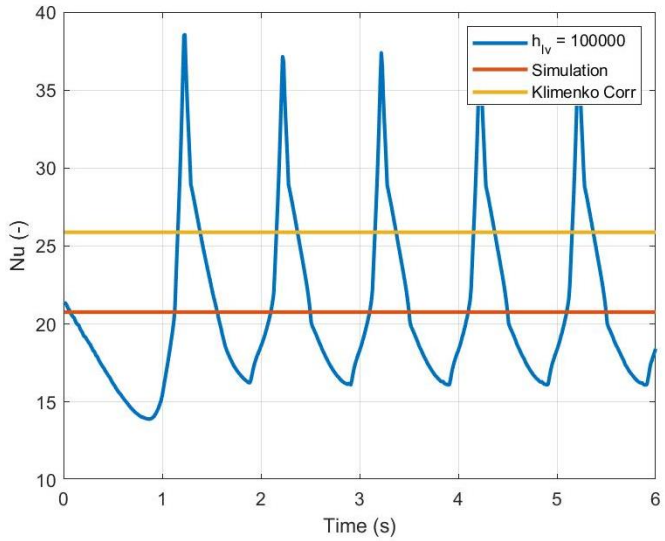

Figure 68. The result of the two-dimensional film boiling problem simulation using Sun Model with filter.

5.4. Film Flow Simulation

Based on the results obtained above, the flow boiling simulation was performed in this study using the Lee model. It is shown in benchmarks that the Lee model works well in phase change simulation; however, its performance is highly dependent on the value of mass transfer intensity. The objective of the simulation, therefore is to find the appropriate value of mass transfer intensity of the evaporation (β_E), which is a constant that needs to be empirically defined based on the consideration of the phenomena.

5.4.1 Simulation Setup

The custom solver, iCEFM was used to perform the CFD simulation in OpenFOAM. Considering the geometry of the experiment and the simulation cost, a two-dimensional (2D) simulation was conducted.

Mesh and Boundary Conditions

The geometry and boundary conditions of the flow boiling system is shown in Figure 69. The system comprises a 2D channel with 1 m length and 5.55 mm width, which represents the gap between the heater and tube of the experimental setup. Fluid properties of Novec 7000 were used. The experimental case with 2.5 kW of heating power and 0.409 m/s of inlet velocity (155 g/s of inlet mass flow rate) was selected as a benchmark case. The inlet velocity and uniform heat flux boundary conditions were applied according to the experimental condition. The fixed wall condition was set on the other side of the wall to investigate the film dynamics on the wall. The wall functions for turbulence modeling were applied to the walls on both sides.

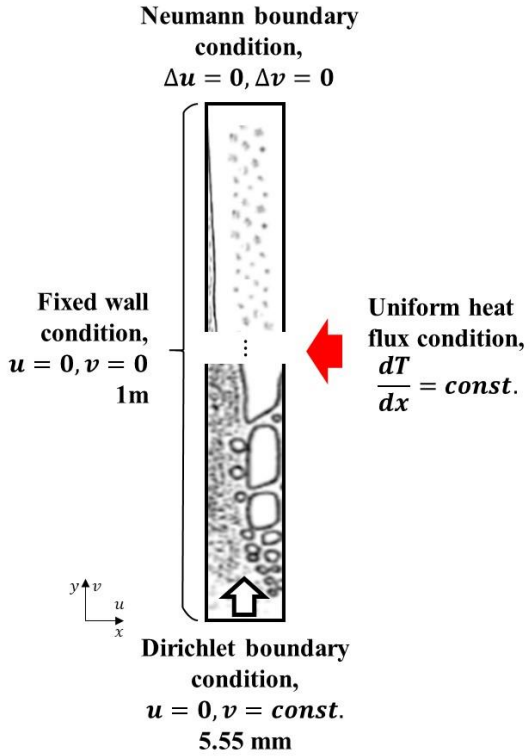

Figure 69. Geometry and boundary conditions of the flow boiling system.

The mesh sensitivity was checked using three different sizes of mesh ($25 \times 1000, 50 \times 2000,$ and 100×4000) as shown in Figure 70. The mean velocity profile near the wall region ($y^+ < 100$) with the isothermal condition was compared with the reference data (Kim et al., 1987) for the test. The velocity of the inlet was calculated as 0.6698 m/s using Eq 13 (Pope, 2000) to ensure that the viscous Reynolds number (Re_τ) is 180.

$$\mathrm{Re}_\tau = 0.09\,\mathrm{Re}^{0.88} \qquad \textit{Eq 13}$$

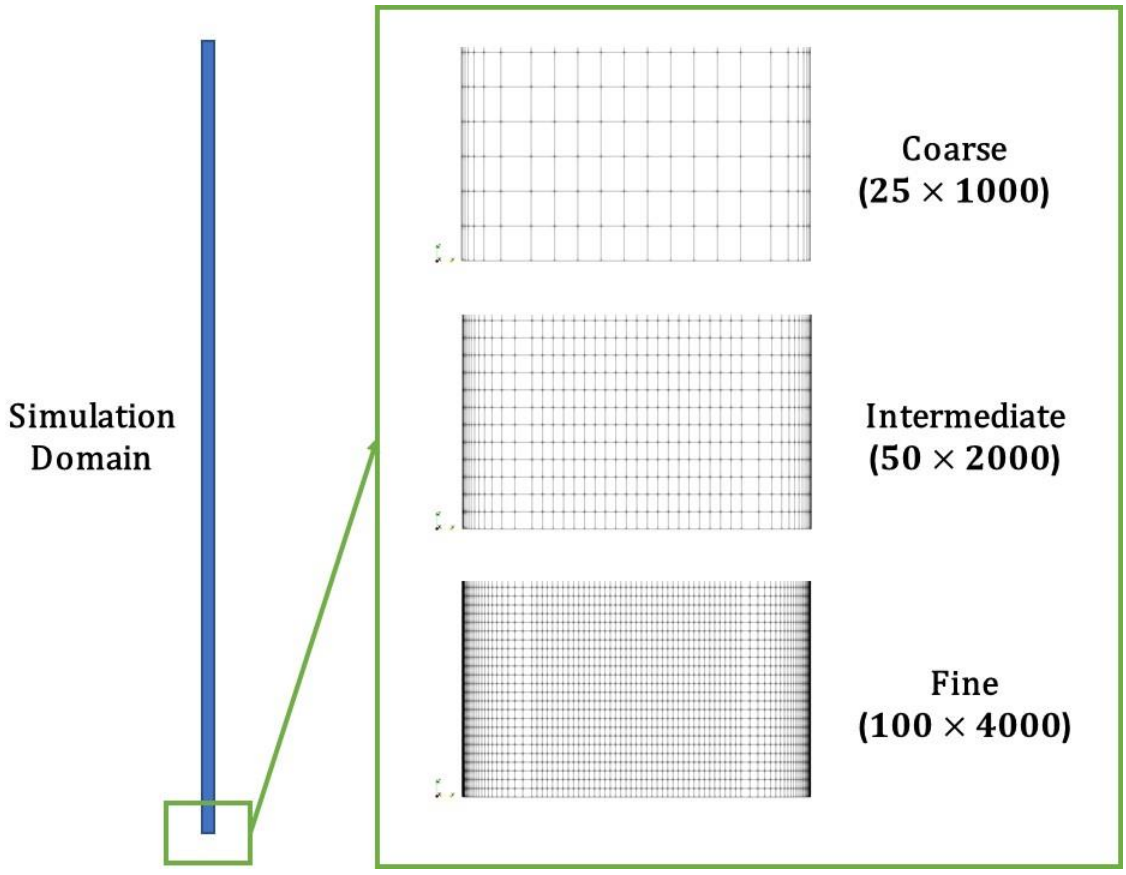

Figure 70. Different sizes of mesh used for the mesh sensitivity test.

The result of the normalized mean velocity profile calculation is shown in Figure 71. The velocity profile of the CFD simulation converges with an increase in the number of meshes. Although there are discrepancies at the viscous sublayer ($y^+ < 10$) and the buffer layer ($y^+ < 30$), the converged results showed good agreement in the log-layer ($30 < y^+$). Considering the computational costs, an intermediate mesh size (50×2000) was selected.

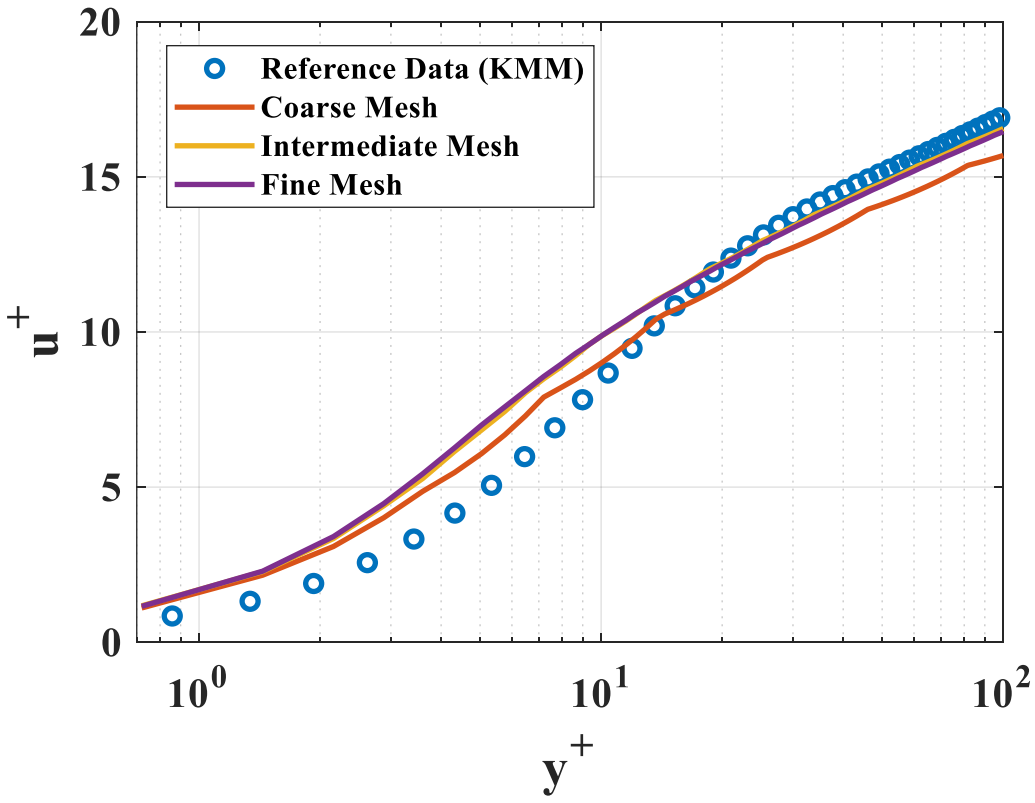

Figure 71. Normalized mean streamwise velocity profile.

Solver Setup

The interCondensatingEvaporatingFoam_MULES solver in the OpenFOAM toolbox was used. Unsteady Reynolds average Navier–Stokes (RANS) simulation was

performed with the $k-\omega$ turbulence model. The initial time step was set to $10^{-6}s$ with an adaptive time step for Co = 1.0. The total simulation time was set to 10 s.

An Euler implicit time scheme was applied for time discretization. The Euler implicit scheme was adopted to calculate the gradient terms numerically and the Gauss upwind scheme was adopted to calculate the divergence terms. The Laplacian terms were discretized by the Gauss linear corrected scheme.

The MULES algorithm was applied as an interface capturing algorithm. The PLIC method was adopted to enhance the performance of the interface capturing. The Lee model was used as a phase change model and multiple values of β_E from 0.01 to 10 were applied to find the value that best matches the film thickness from experimental data.

5.4.2 Simulation Result

The simulation results of the flow boiling CFD were checked. Flow patterns and film thickness data were extracted and compared with the experimental results.

Flow Pattern

Development of the flow boiling calculated by the CFD simulation is shown in Figure 72. The boiling starts from the upstream of the flow and the amount of the vapor increases as the flow moves downstream. The wave structure and entrainment of droplets caused by the interaction at the interface can be observed.

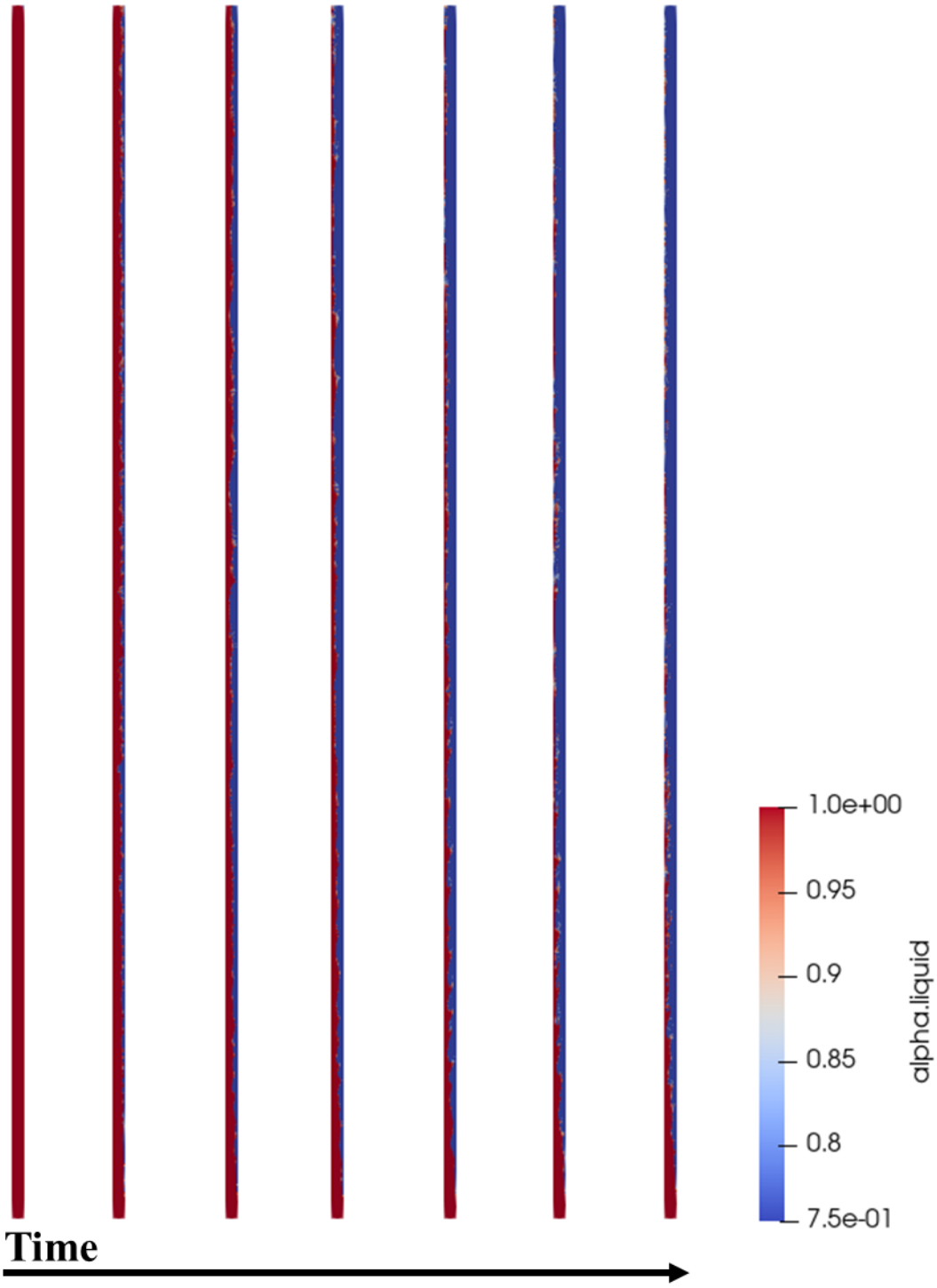

Figure 72. Development of the flow boiling respect to the simulation time.

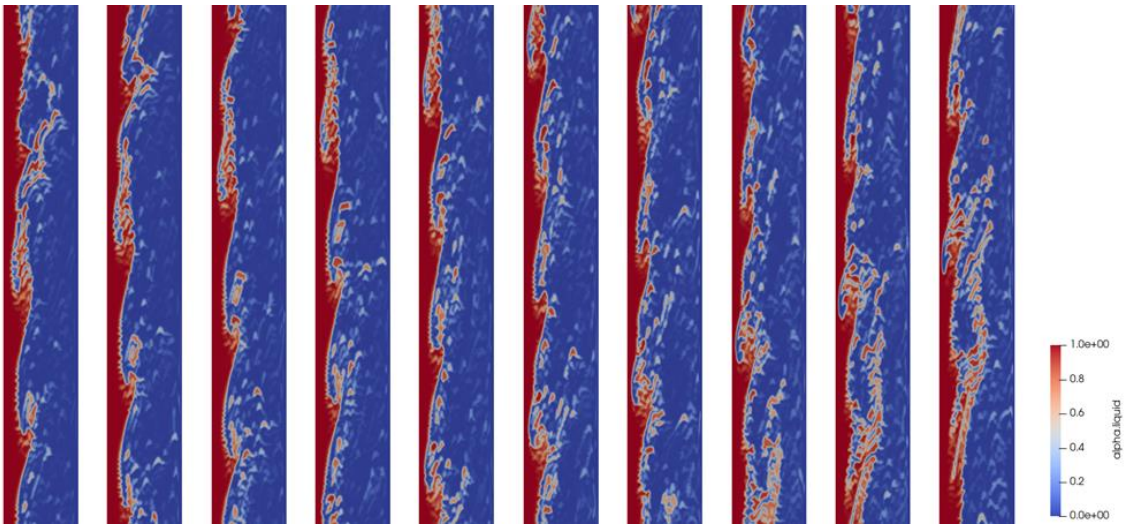

Figure 73. Flow pattern of the liquid film from the simulation.

Figure 73 presents the behavior of the liquid film calculated by the simulation. The structure of the film can be clearly recognized from the results. Disturbance waves are traveling above the base film. Some waves transform to the roll wave and generate entrainments when the velocity difference between vapor increases. Entrainments moves faster than the waves in the film and are accelerated further due to the high velocity of the vapor. The total thickness of the film become smaller as it moves downstream and the number of waves decreases as well.

Film Thickness

A set of simulation with varying mass transfer intensity (β_e) from 0.1 to 1 were performed to determine the appropriate value. The film thickness was measured at the same position with the experiment. A total of 1000 simulation results with 0.001 s of time step were collected after the simulation reached the steady state and they were

averaged to be used as a dataset. The same methodology explained in Figure 20 was used to measure the base film location. The phase fraction was used as an indicator of the base film location instead of the averaged light intensity of the LIF image. The results are plotted in Figure 74. The film thickness increases with an increase in β_e. The measured thickness from the experiment with the same boundary condition is 0.3756 mm. The film thickness of the phase change simulation with $\beta_e = 0.3$ for the Lee model is 0.3535 mm, and it shows the best agreement with the experimental data. When the data are interpolated, the expected value of β_e = 0.323 best matches the experimental data.

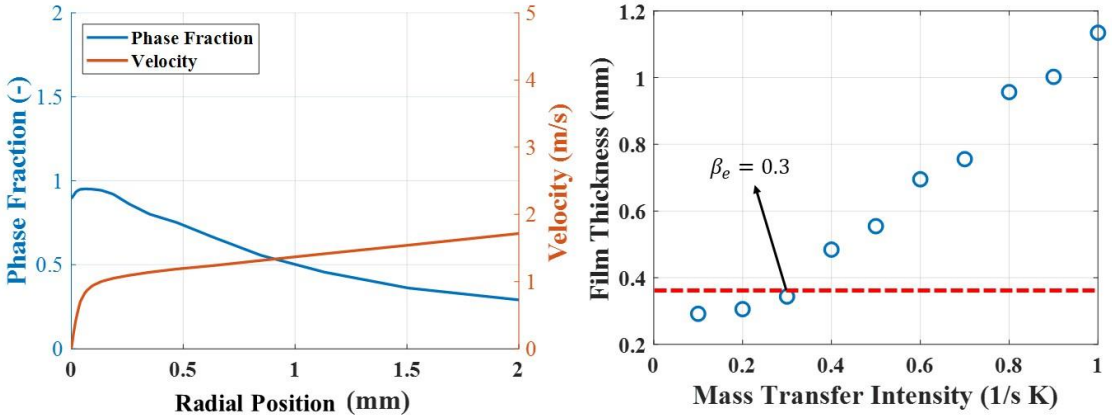

Figure 74. Averaged film thickness from varying mass transfer intensity (β_e).

Film Dynamics

Figure 75 presents the averaged radial velocity profile at the 0.85 m downstream from the inlet. When the point, where the slope of the average phase fraction changes, is considered as a boundary of the base film, 1.058 m/s of velocity at the top of the base

can be obtained. If all the liquid is assumed to flow as a base film, 3.139 m/s of the velocity can be calculated from the superficial velocity information of the experimental boundary condition. By calculating area-averaged velocity from the simulation result, 25.82 % of liquid can be considered as flowing as a form of the base film, and rest of the liquid travels as disturbance waves and droplets.

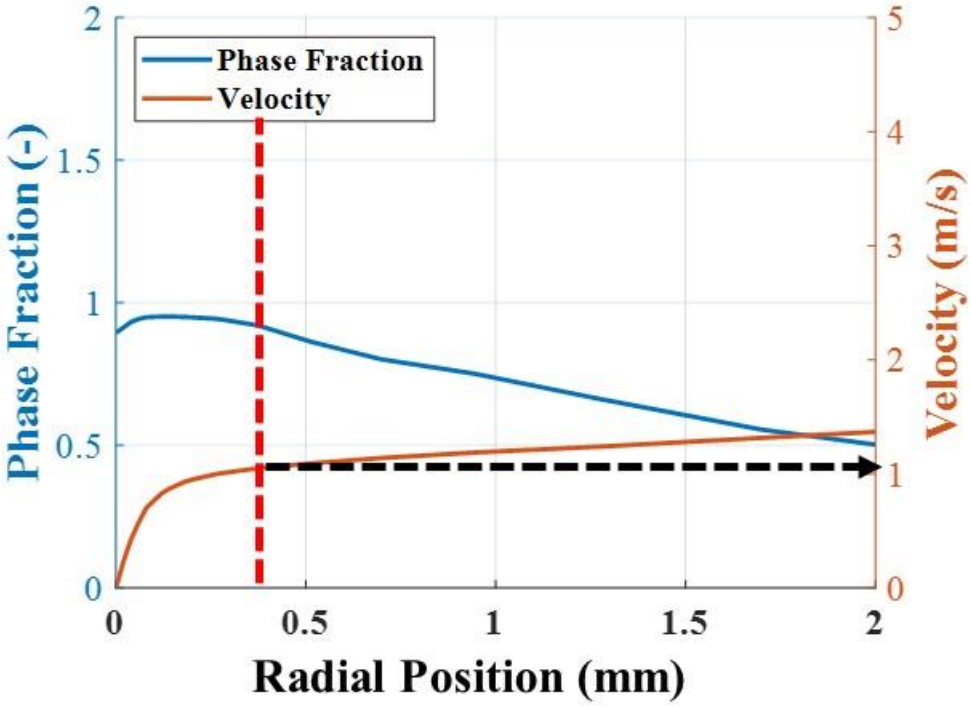

Figure 75. Averaged velocity and phase fraction of the simulation case with $\beta_e = 0.3$.

Figure 76, The film thickness obtained by CFD is plotted using the phase field of position and time. The same methodology explained in Figure 24 was applied to calculate the velocity of the wave from the CFD results. Total 50 waves were randomly selected from the simulation result and their slopes were measured in the phase field of

position and time. As a result, 1.1486 m/s of averaged wave velocity was obtained. When the value is compared to the experimental results, which is 1.0351 m/s, it has 10.97 % deviation.

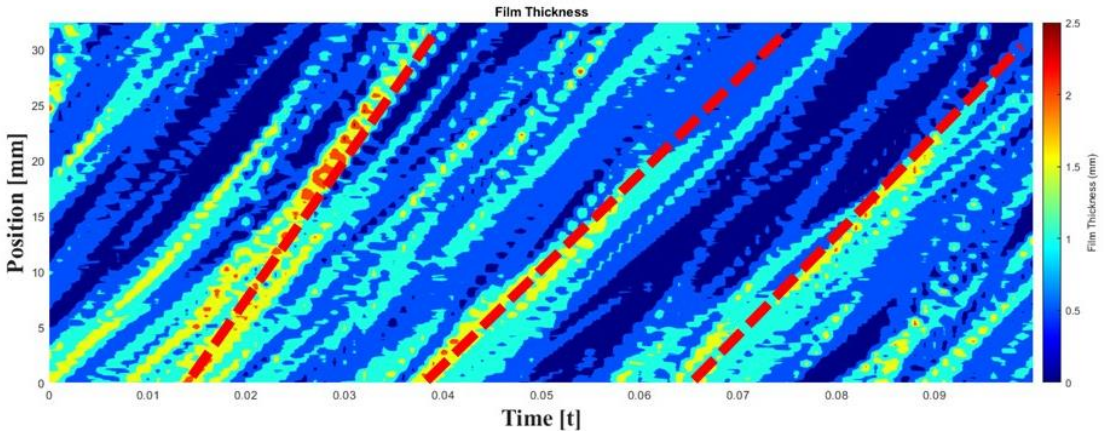

Figure 76. Liquid film phase field with respect to position and time from the results of the simulation.

CHAPTER VI

CONCLUSION

Annular flow boiling experiments in concentric and eccentric annuli were conducted in this study. The high-fidelity experimental data to support the validation of the CFD simulations was produced. Advanced measurement techniques including LIF, PIV, shadowgraph, and CCS were applied to investigate the complex behaviors of the flow including liquid films, entrainment and deposition of droplets, and to determine the difference between the concentric and eccentric geometries. Traditional sensors such as pressure transducers, thermocouples were used to measure pressure and temperature, respectively.

This document reported the detailed analyses of the outer liquid film behavior measured by LIF and CCS, pressure drop, and temperature data (and also the heat transfer coefficient values). The thickness of the base film was measured from 0.3358–0.3964 mm in the concentric geometry; the range of the base film thickness becomes 0.3303–0.3951 mm for the wide gap side of the annulus, and 0.1978–0.3898 mm for the narrow gap side in the eccentric geometry. The superficial velocity of the vapor is concluded as a primary factor of change in the value of parameters related to the liquid film including the base film thickness, and the wave amplitude based on the experimental data. The heat transfer coefficient was measured using the surface temperature of the heater. The heat transfer coefficient was ranged from 1341.95–4278.71 $W/m^2 \cdot K$ for the concentric geometry, and 2062.64–3095.68 $W/m^2 \cdot K$ for the eccentric geometry. The increasing trend was found according to the liquid superficial

velocity, and the reversed trend was observed for the vapor superficial velocity. Exceptionally low heat transfer coefficient was measured in the case of dry out, which is physically possible because of the loss of cooling.

The analysis results of the behavior of droplets obtained from the high-quality shadowgraph images were also reported. The velocity of bubbles located at the slow region was between 0.5–2.0 m/s, while the velocity of droplets was distributed from 1.0–5.0 m/s from the observation. Further, it was found that the velocity of the droplet was affected by the vapor superficial velocity significantly. In contrast, the velocity of bubbles did not seem to be seriously affected by the liquid superficial velocity.

The flow boiling CFD simulation was performed. The performance of a standard solver, interCondensatingEvaporatingFoam, which was provided by OpenFOAM v1906 as a phase change solver with the VOF method, was evaluated. The limitation of the solver in capturing the interface between liquid and vapor was identified. An excessive interface diffusion and unphysical mixing were found from the result of the standard solver of OpenFOAM. Therefore, two custom solvers were built to fix the problem and enhance the interface capturing performance by modifying and merging standard solvers. The verification of these solvers was achieved by solving the rising bubble benchmark problem.

Phase change models—Lee model, Sun model, and Chen model—were implemented into OpenFOAM and tested using benchmark problems. All of them showed good performance in the Stefan benchmark problem. The Lee and Chen models worked fine in a two-dimensional film boiling problem with 11.66% of the maximum

error with a theoretical solution. The Sun model, however, worked poorly with the problem because of errors caused by gradients of temperature and the void fraction. The performance of the Sun model was enhanced by increasing iterations of the MULES algorithm and a filter to prevent the reversed-phase change.

The film thickness data from the flow boiling simulation was compared to the experimental data to find the mass transfer intensity (β_e) for the Lee model. The simulation result with $\beta_e = 0.3$ showed the best match with the experimental result.

REFERENCES

Alekseenko, Sergey, Cherdantsev, A., Cherdantsev, M., Isaenkov, S., Kharlamov, S., & Markovich, D. (2012). Application of a high-speed laser-induced fluorescence technique for studying the three-dimensional structure of annular gas-liquid flow. *Experiments in Fluids*, *53*(1), 77–89. https://doi.org/10.1007/s00348-011-1200-5

Alekseenko, S. V., Antipin, V. A., Cherdantsev, A. V., Kharlamov, S. M., & Markovich, D. M. (2008). Investigation of waves interaction in annular gas-liquid flow using high-speed fluorescent visualization technique. *Microgravity Science and Technology*, *20*(3–4), 271–275. https://doi.org/10.1007/s12217-008-9028-1

Alekseenko, Sergey V., Cherdantsev, A. V., Cherdantsev, M. V., Isaenkov, S. V., & Markovich, D. M. (2015). Study of formation and development of disturbance waves in annular gas-liquid flow. *International Journal of Multiphase Flow*, *77*, 65–75. https://doi.org/10.1016/j.ijmultiphaseflow.2015.08.007

Alekseenko, Sergey V., Cherdantsev, A. V., Heinz, O. M., Kharlamov, S. M., & Markovich, D. M. (2014). Analysis of spatial and temporal evolution of disturbance waves and ripples in annular gas-liquid flow. *International Journal of Multiphase Flow*, *67*(S), 122–134. https://doi.org/10.1016/j.ijmultiphaseflow.2014.07.009

Angeli, P., & Gavriilidis, A. (2008). Hydrodynamics of Taylor flow in small channels: A review. *Proceedings of the Institution of Mechanical Engineers, Part C: Journal of Mechanical Engineering Science*, *222*(5), 737–751. https://doi.org/10.1243/09544062JMES776

Anglart, H. (2014). Modeling of liquid film flow in annuli. *Journal of Power of*

Technologies, *94*, 8–15.

B.J.Azzopardi. (1986). Disturbance wave frequencies, velocities and spacing in vertical annular two-phase flow. *Neculaer Engineering and Disign*, *92*, 83–94.

Bartel, M. D., Ishii, M., Masukawa, T., Mi, Y., & Situ, R. (2001). Interfacial area measurements in subcooled flow boiling. *Nuclear Engineering and Design*, *210*(1–3), 135–155. https://doi.org/10.1016/S0029-5493(01)00415-0

Belt, R. J., Van't Westende, J. M. C., Prasser, H. M., & Portela, L. M. (2010). Time and spatially resolved measurements of interfacial waves in vertical annular flow. *International Journal of Multiphase Flow*, *36*(7), 570–587. https://doi.org/10.1016/j.ijmultiphaseflow.2010.03.004

Berna, C., Escrivá, A., Muñoz-Cobo, J. L., & Herranz, L. E. (2014). Review of droplet entrainment in annular flow: Interfacial waves and onset of entrainment. *Progress in Nuclear Energy*, *74*, 14–43. https://doi.org/10.1016/j.pnucene.2014.01.018

Bottini, J. L., Zhu, L., Ooi, Z. J., Zhang, T., & Brooks, C. S. (2020). Experimental study of boiling flow in a vertical heated annulus with local two-phase measurements and visualization. *International Journal of Heat and Mass Transfer*, *155*, 119712. https://doi.org/10.1016/j.ijheatmasstransfer.2020.119712

Brackbill, J. U., Kothe, D. B., & Zemach, C. (1992). A continuum method for modeling surface tension. *Journal of Computational Physics*, *100*(2), 335–354. https://doi.org/10.1016/0021-9991(92)90240-Y

Brighton, J. A., & Jones, J. B. (1964). Fully Developed Turbulent Flow in Annuli. *Journal of Basic Engineering*, *86*(4), 835–842. https://doi.org/10.1115/1.3655966

Bruder, M., Sembach, L., Krumova, V., & Sattelmayer, T. (2018). Local data of heat flux, wall temperature and the void phase along the boiling curve during vertical subcooled flow boiling of refrigerant Novec 649 at a copper wall. *Data in Brief*, *21*, 1415–1429. https://doi.org/10.1016/j.dib.2018.10.138

Chen, G., Nie, T., & Yan, X. (2020). An explicit expression of the empirical factor in a widely used phase change model. *International Journal of Heat and Mass Transfer*, *150*, 119279. https://doi.org/10.1016/j.ijheatmasstransfer.2019.119279

Clump, C. W., & Kwasnoski, D. (1968). Turbulent flow in concentric annuli. *AIChE Journal*, *14*(1), 164–168.

Collier, J. G., & Thome, J. R. (1994). *Convective Boiling and Condensation* (3rd ed.). Clarendon Press.

D.Youngs, L. (1982). Time-dependent multi-material flow with large fluid distortion. *Numerical Methods for Fluid Dynamics*, 273–285.

Damsohn, M., & Prasser, H. M. (2009). High-speed liquid film sensor for two-phase flows with high spatial resolution based on electrical conductance. *Flow Measurement and Instrumentation*, *20*(1), 1–14. https://doi.org/10.1016/j.flowmeasinst.2008.06.006

Dasgupta, A., Chandraker, D. K., Kshirasagar, S., Reddy, B. R., Rajalakshmi, R., Nayak, A. K., Walker, S. P., Vijayan, P. K., & Hewitt, G. F. (2017). Experimental investigation on dominant waves in upward air-water two-phase flow in churn and annular regime. *Experimental Thermal and Fluid Science*, *81*, 147–163. https://doi.org/10.1016/j.expthermflusci.2016.10.012

Dittus, F. W., & Boelter, L. M. K. (1930). Heat transfer in automobile radiators of the tubular type. *International Communications in Heat and Mass Transfer*, *12*(1), 3–22. https://doi.org/https://doi.org/10.1016/0735-1933(85)90003-X

Dobran, F. (1983). Analyse hydrodynamique et thermique d'un ecoulement annulaire diphasique avec un nouveau modele de turbulence de film liquide. *International Journal of Heat and Mass Transfer*, *26*(8), 1159–1171. https://doi.org/10.1016/S0017-9310(83)80170-7

Fadhl B., Wrobel L. C., J. H. (2013). Numerical modelling of the temperature distribution in a two-phase closed thermosyphon. *Applied Thermal Engineering*, *60*, 122–131.

Furukawa, T., & Sekoguchi, K. (1986). Phase distribution for air-water two-phase flow in annuli. *Bulletin of JSME*, *29*(255), 3007–3014. http://www.mendeley.com/research/geology-volcanic-history-eruptive-style-yakedake-volcano-group-central-japan/

Hall Taylor, N., Hewitt, G. F., & Lacey, P. M. C. (1963). The motion and frequency of large disturbance waves in annular two-phase flow of air-water mixtures. *Chemical Engineering Science*, *18*(8), 537–552. https://doi.org/10.1016/0009-2509(63)85014-9

Hazuku, T., Takamasa, T., & Matsumoto, Y. (2008). Experimental study on axial development of liquid film in vertical upward annular two-phase flow. *International Journal of Multiphase Flow*, *34*(2), 111–127. https://doi.org/10.1016/j.ijmultiphaseflow.2007.10.008

Hernández, L., Enrique Julia, J., Ozar, B., Hibiki, T., & Ishii, M. (2011). Flow regime identification in boiling two-phase flow in a vertical annulus. *Journal of Fluids Engineering, Transactions of the ASME*, *133*(9), 1–10. https://doi.org/10.1115/1.4004838

Hewitt, G. F., & Govan, A. H. (1990). Phenomenological modelling of non-equilibrium flows with phase change. *International Journal of Heat and Mass Transfer*, *33*(2), 229–242. https://doi.org/10.1016/0017-9310(90)90094-B

Hewitt, G. F., & Hall-Taylor, N. S. (1970). Copyright. In *Annular Two-phase Flow*. https://doi.org/10.1016/b978-0-08-015797-9.50002-9

Hysing, S., Turek, S., Kuzmin, D., Parolini, N., Burman, E., Ganesan, S., & Tobiska, L. (2009). Quantitative benchmark computations of two-dimensional bubble dynamics. *International Journal for Numerical Methods in Fluids*, *60*(11), 1259–1288.

Ishii, M. (1975). *Thermo-Fluid Dynamic Theory of Two-Phase Flow*. Eyrolles.

Islam, M. T., Ganesan, P. B., Cheng, J., & Uddin, M. S. (2020). Single bubble rising behaviors in Newtonian and non-Newtonian fluids with validation of empirical correlations: A computational fluid dynamics study. *Engineering Reports*, *2*(1), 1–15. https://doi.org/10.1002/eng2.12100

Jeong, J. J., Ozar, B., Dixit, A., Juliá, J. E., Hibiki, T., & Ishii, M. (2008). Interfacial area transport of vertical upward air-water two-phase flow in an annulus channel. *International Journal of Heat and Fluid Flow*, *29*(1), 178–193. https://doi.org/10.1016/j.ijheatfluidflow.2007.07.007

Julia, J. E., & Hibiki, T. (2011). Flow regime transition criteria for two-phase flow in a vertical annulus. *International Journal of Heat and Fluid Flow*, *32*(5), 993–1004. https://doi.org/10.1016/j.ijheatfluidflow.2011.06.001

Julia, J. E., Ozar, B., Dixit, A., Jeong, J. J., Hibiki, T., & Ishii, M. (2009). Axial development of flow regime in adiabatic upward two-phase flow in a vertical annulus. *Journal of Fluids Engineering, Transactions of the ASME*, *131*(2), 0213021–02130211. https://doi.org/10.1115/1.3059701

Julia, J. E., Ozar, B., Jeong, J. J., Hibiki, T., & Ishii, M. (2011). Flow regime development analysis in adiabatic upward two-phase flow in a vertical annulus. *International Journal of Heat and Fluid Flow*, *32*(1), 164–175. https://doi.org/10.1016/j.ijheatfluidflow.2010.09.003

Kandlikar, S. G. (1990). A general correlation for saturated two-phase flow boiling heat transfer inside horizontal and vertical tubes. *Journal of Heat Transfer*, *112*(1), 219–228. https://doi.org/10.1115/1.2910348

Kelessidis, V. C., & Dukler, A. E. (1989). Modeling flow pattern transitions for upward gas-liquid flow in vertical concentric and eccentric annuli. *International Journal of Multiphase Flow*, *15*(2), 173–191. https://doi.org/10.1016/0301-9322(89)90069-4

Kim, J., Moin, P., & Moser, R. (1987). Turbulence statistics in fully developed channel flow at low Reynolds number. *Journal of Fluid Mechanics*, *177*, 133–166. https://doi.org/10.1017/S0022112087000892

Klimenko, V. V. (1981). Film boiling on a horizontal plate - new correlation. *International Journal of Heat and Mass Transfer*, *24*(1), 69–79.

https://doi.org/10.1016/0017-9310(81)90094-6

Lee, T. H., Park, G. C., & Lee, D. J. (2002). Local flow characteristics of subcooled boiling flow of water in a vertical concentric annulus. *International Journal of Multiphase Flow*, *28*(8), 1351–1368. https://doi.org/10.1016/S0301-9322(02)00026-5

Levy, S. (1999). *Two-phase flow in complex systems*. John Wiley & Sons.

Moeck, E. O., & Stachiewicz, J. W. (1972). A droplet interchange model for annular-dispersed, two-phase flow. *International Journal of Heat and Mass Transfer*, *15*(4), 637–653. https://doi.org/https://doi.org/10.1016/0017-9310(72)90110-X

Nabil, M., & Rattner, A. S. (2016). interThermalPhaseChangeFoam—A framework for two-phase flow simulations with thermally driven phase change. *SoftwareX*, *5*, 216–226. https://doi.org/10.1016/j.softx.2016.10.002

Nakoryakov, V. E., Kuznetsov, V. V., & Vitovsky, O. V. (1992). Experimental investigation of upward gas-liquid flow in a vertical narrow annulus. *International Journal of Multiphase Flow*, *18*(3), 313–326. https://doi.org/10.1016/0301-9322(92)90019-D

Nedderman, R. M., & Shearer, C. J. (1963). The motion and frequency of large disturbance waves in annular two-phase flow of air-water mixtures. *Chemical Engineering Science*, *18*(10), 661–670. https://doi.org/10.1016/0009-2509(63)85036-8

Okawa, T., Goto, T., & Yamagoe, Y. (2010). Liquid film behavior in annular two-phase flow under flow oscillation conditions. *International Journal of Heat and Mass*

Transfer, *53*(5–6), 962–971. https://doi.org/10.1016/j.ijheatmasstransfer.2009.11.024

Onishi, H., Kawamura, M., Tada, Y., & Takimoto, A. (2013). Numerical analysis on heat transfer characteristics of looped mini channel using phase-change VOF method. *ASME International Conference on Nanochannels, Mocrochannels and Minichannels*.

Ooi, Z. J., Kumar, V., & Brooks, C. S. (2019). Experimental database of two-phase natural circulation with local measurements. *Progress in Nuclear Energy*, *116*(December 2018), 124–136. https://doi.org/10.1016/j.pnucene.2019.04.003

Ozar, B., Brooks, C. S., Euh, D. J., Hibiki, T., & Ishii, M. (2013). Investigation of one-dimensional interfacial area transport for vertical upward air-water two-phase flow in an annular channel at elevated pressures. *Nuclear Engineering and Design*, *263*(2013), 362–379. https://doi.org/10.1016/j.nucengdes.2013.05.018

Pham, S. H., Kawara, Z., Yokomine, T., & Kunugi, T. (2014). Detailed observations of wavy interface behaviors of annular two-phase flow on rod bundle geometry. *International Journal of Multiphase Flow*, *59*, 135–144. https://doi.org/10.1016/j.ijmultiphaseflow.2013.11.004

Rattner, A. S., & Garimella, S. (2014). Simple mechanistically consistent formulation for volume-of-fluid based computations of condensing flows. *Journal of Heat Transfer*, *136*(7), 1–9. https://doi.org/10.1115/1.4026808

Renardy, Y., & Renardy, M. (2002). PROST: A parabolic reconstruction of surface tension for the volume-of-fluid method. *Journal of Computational Physics*, *183*(2),

400–421. https://doi.org/10.1006/jcph.2002.7190

Roenby, J., Bredmose, H., & Jasak, H. (2016). A computational method for sharp interface advection. *Royal Society Open Science*, *3*(11). https://doi.org/10.1098/rsos.160405

S. B. Pope. (2000). *Turbulent Flows*. Cambridge University Press.

Sadatomi, M., Sato, Y., & Saruwatari, S. (1982). Two-phase flow in vertical noncircular channels. *International Journal of Multiphase Flow*, *8*(6), 641–655. https://doi.org/10.1016/0301-9322(82)90068-4

Samkhaniani, N., & Ansari, M. (2012). A VOF method to phase change modeling. *Proceedings of 1st Iranian Conference on Heat and Mass Transfer-ICHMT2012*, *2*(October), 1–9.

Schubring, D., Ashwood, A. C., Shedd, T. A., & Hurlburt, E. T. (2010). Planar laser-induced fluorescence (PLIF) measurements of liquid film thickness in annular flow. Part I: Methods and data. *International Journal of Multiphase Flow*, *36*(10), 815–824. https://doi.org/10.1016/j.ijmultiphaseflow.2010.05.007

Schubring, DuWayne. (2009). *Behavior interrelationships in annular flow*. University of Wisconsin-Madison.

Situ, R., Hibiki, T., Sun, X., Mi, Y., & Ishii, M. (2004). Flow structure of subcooled boiling flow in an internally heated annulus. *International Journal of Heat and Mass Transfer*, *47*(24), 5351–5364. https://doi.org/10.1016/j.ijheatmasstransfer.2004.06.035

Su, G. Y., D'Aleo, F. P., Phillips, B., Streich, R. M., Al-Safran, E., Buongiorno, J., &

Prasser, H. M. (2019). On the oscillatory nature of heat transfer in steady annular flow. *International Communications in Heat and Mass Transfer*, *108*. https://doi.org/10.1016/j.icheatmasstransfer.2019.104328

Sun, D. L., Xu, J. L., & Wang, L. (2012). Development of a vapor-liquid phase change model for volume-of-fluid method in FLUENT. *International Communications in Heat and Mass Transfer*, *39*(8), 1101–1106. https://doi.org/10.1016/j.icheatmasstransfer.2012.07.020

Sun, D., Xu, J., & Chen, Q. (2014). Modeling of the evaporation and condensation phase-change problems with FLUENT. *Numerical Heat Transfer, Part B: Fundamentals*, *66*(4), 326–342. https://doi.org/10.1080/10407790.2014.915681

Sun, X., Kuran, S., & Ishii, M. (2004). Cap bubbly-to-slug flow regime transition in a vertical annulus. *Experiments in Fluids*, *37*(3), 458–464. https://doi.org/10.1007/s00348-004-0809-z

Sussman, M. (1994). A level set approach for computing solutions to incompressible two-phase flow. In *Journal of Computational Physics* (Vol. 114, Issue 1, pp. 146–159). https://doi.org/10.1006/jcph.1994.1155

Todreas, N. E., & Kazimi, M. S. (2011). *NUCLEAR SYSTEMS: Vol. i* (2nd ed., Issue 2011). CRC Press.

Ubbink, O., & Issa, R. I. (1999). A Method for Capturing Sharp Fluid Interfaces on Arbitrary Meshes. *Journal of Computational Physics*, *153*(1), 26–50. https://doi.org/10.1006/jcph.1999.6276

Ueda, T., & Suzuki, S. (1978). Behaviour of liquid films and flooding in counter-current

two-phase flow. Part 2. Flow in annuli and rod bundles. International Journal of Multiphase Flow. *International Journal of Multiphase Flow*, *4*(2), 157–170.

Unverdi, S. O., & Tryggvason, G. (1992). A front-tracking method for viscous, incompressible, multi-fluid flows. *Journal of Computational Physics*, *100*(1), 25–37. https://doi.org/10.1016/0021-9991(92)90307-K

Wallis, G. G. (1969). *One dimensional two-phase flow*. McGraw-Hill Book Co. Inc. http://repositorio.unan.edu.ni/2986/1/5624.pdf

Wörner, M. (2012). Numerical modeling of multiphase flows in microfluidics and micro process engineering: A review of methods and applications. *Microfluidics and Nanofluidics*, *12*(6), 841–886. https://doi.org/10.1007/s10404-012-0940-8

Yokoi, K. (2007). Efficient implementation of THINC scheme: A simple and practical smoothed VOF algorithm. *Journal of Computational Physics*, *226*(2), 1985–2002. https://doi.org/10.1016/j.jcp.2007.06.020

Yun, B. J., Bae, B. U., Euh, D. J., & Song, C. H. (2010). Experimental investigation of local two-phase flow parameters of a subcooled boiling flow in an annulus. *Nuclear Engineering and Design*, *240*(12), 3956–3966. https://doi.org/10.1016/j.nucengdes.2010.02.004

Zadrazil, I., Matar, O. K., & Markides, C. N. (2014). An experimental characterization of downwards gas-liquid annular flow by laser-induced fluorescence: Flow regimes and film statistics. *International Journal of Multiphase Flow*, *60*, 87–102. https://doi.org/10.1016/j.ijmultiphaseflow.2013.11.008

Zboray, R., & Prasser, H. M. (2013). Measuring liquid film thickness in annular two-

phase flows by cold neutron imaging. *Experiments in Fluids*, *54*(9). https://doi.org/10.1007/s00348-013-1596-1

Zhang, H. B., & Hewitt, G. F. (2017). New models of droplet deposition and entrainment for prediction of liquid film flow in vertical annuli. *Applied Thermal Engineering*, *113*, 362–372. https://doi.org/10.1016/j.applthermaleng.2016.11.029

Zhao, Y., Markides, C. N., Matar, O. K., & Hewitt, G. F. (2013). Disturbance wave development in two-phase gas-liquid upwards vertical annular flow. *International Journal of Multiphase Flow*, *55*, 111–129. https://doi.org/10.1016/j.ijmultiphaseflow.2013.04.001

Zuber, N., & Findlay, J. A. (1965). Average volumetric concentration in two-phase flow systems. *Journal of Heat Transfer*, *87*, 453–468.

APPENDIX A

RESULTS OF MEASUREMENTS

A.1 Concentric Geometry Test #1

Power [W]	**J_v [m/s]**	**J_l [m/s]**	**T_{top} [°C]**	**T_{bottom} [°C]**	**HTC [$W / m^2 \cdot K$]**
2000	6.216	0.3918	52.441	56.554	3269.78
2000	6.310	0.3336	52.190	56.350	3364.73
2000	6.362	0.3010	52.037	56.127	3421.50
2000	6.437	0.2544	51.565	55.694	3554.73
2000	6.490	0.2218	51.339	55.304	3630.44
2500	8.022	0.3332	55.236	58.294	3664.28
2500	8.112	0.2773	55.074	58.004	3733.70
2500	8.164	0.2447	54.812	57.707	3805.06
2500	8.262	0.1841	54.776	57.410	3857.18
2500	8.284	0.1701	54.305	57.011	3957.39
3000	9.839	0.2675	61.384	59.840	3485.15
3000	9.937	0.2070	61.237	59.556	3538.64
3000	10.026	0.1511	59.569	58.986	3803.54
3000	10.026	0.1511	62.488	58.504	3413.74
3000	10.101	0.1045	100.835	53.750	1465.96
3500	11.537	0.2764	64.523	61.358	3666.03
3500	11.611	0.2298	65.107	60.898	3620.58
3500	11.649	0.2065	72.665	60.288	2922.28
4000	13.264	0.2666	81.054	62.099	2734.18

A.2 Pressure Drop of Test #1

Power [W]	Inlet Mass Flow Rate [g/s]	J_v [m/s]	J_l [m/s]	Gauge Pressure [kPa]	Total Pressure Drop [kPa/m]	Pressure Drop at the Annular Region [kPa/m]
2000	154.167	6.216	0.3918	34.947	3.919	-2.864
2000	133.333	6.310	0.3336	33.718	2.575	-3.997
2000	121.667	6.362	0.3010	31.708	1.025	-4.918
2000	105.000	6.437	0.2544	29.330	0.338	-5.394
2000	93.333	6.490	0.2218	27.249	-0.740	-5.932
2500	136.667	8.022	0.3332	37.867	4.348	-3.521
2500	116.667	8.112	0.2773	35.331	2.351	-4.784
2500	105.000	8.164	0.2447	32.829	1.489	-5.436
2500	83.333	8.262	0.1841	30.991	-0.598	-6.122
2500	78.333	8.284	0.1701	27.755	-1.392	-6.210
3000	116.667	9.839	0.2675	39.189	4.146	-4.189
3000	95.000	9.937	0.2070	36.671	1.199	-5.291
3000	75.000	10.026	0.1511	33.735	0.197	-6.029
3000	75.000	10.026	0.1511	32.187	-0.637	-5.807
3000	58.333	10.101	0.1045	29.607	-2.857	-7.391
3500	123.333	11.537	0.2764	42.638	6.590	-3.001
3500	106.667	11.611	0.2298	38.036	4.472	-4.433
3500	98.333	11.649	0.2065	35.374	3.438	-5.049
4000	123.333	13.264	0.2666	44.330	8.268	-4.230

A.3 Concentric Geometry Test #2

Power [W]	J_v [m/s]	J_l [m/s]	Film Thickness [mm]		T_{top} [℃]	T_{bottom} [℃]	HTC $[W / m^2 \cdot K]$
			CCS	LIF			
2000	6.243	0.3755	0.3964	0.5024	53.491	54.912	3106.14
2000	6.347	0.3103	0.3732	0.3898	53.416	54.821	3170.96
2000	6.415	0.2684	0.3683	0.3328	52.705	54.364	3326.46
2000	6.452	0.2451	0.3694	0.3328	52.525	53.912	3378.35
2000	6.527	0.1985	0.3524	0.3232	52.646	53.766	3395.42
2500	8.030	0.3285	0.3756	0.3708	57.377	56.871	3331.65
2500	8.112	0.2773	0.3744	0.3328	56.928	56.666	3431.77
2500	8.176	0.2377	0.3606	0.3328	55.469	56.133	3693.77
2500	8.254	0.1888	0.3646	0.3232	55.931	55.835	3650.76
2500	8.292	0.1655	0.3575	0.3232	54.588	55.271	3906.38
3000	9.802	0.2908	0.3552	0.3328	60.323	58.292	3611.86
3000	9.892	0.2349	0.3506	0.3328	60.002	58.152	3689.97
3000	9.952	0.1977	0.3497	0.3232	58.167	57.509	3994.13
3000	10.034	0.1464	0.3358	0.3136	64.122	57.072	3231.04
3500	11.581	0.2484	0.3514	0.3232	63.220	60.025	3844.41
3500	11.656	0.2019	0.3442	0.3136	71.018	59.520	3054.26
4000	13.219	0.2946	0.3470	0.3136	70.667	62.089	3496.84

A.4 Pressure Drop of Test #2

Power [W]	Inlet Mass Flow Rate [g/s]	J_v [m/s]	J_l [m/s]	Gauge Pressure [kPa]	Total Pressure Drop [kPa/m]	Pressure Drop at the Annular Region [kPa/m]
2000	148.333	6.243	0.3755	33.241	3.669	-3.244
2000	125.000	6.347	0.3103	31.474	2.092	-4.403
2000	110.000	6.415	0.2684	29.494	0.761	-5.132
2000	101.667	6.452	0.2451	26.432	-0.053	-5.655
2000	85.000	6.527	0.1985	25.610	-1.462	-6.258
2500	135.000	8.030	0.3285	35.736	4.736	-3.602
2500	116.667	8.112	0.2773	33.418	2.504	-4.695
2500	102.500	8.176	0.2377	30.759	1.574	-5.421
2500	85.000	8.254	0.1888	28.450	-0.639	-6.362
2500	76.667	8.292	0.1655	26.048	-1.262	-6.301
3000	125.000	9.802	0.2908	36.857	5.460	-3.724
3000	105.000	9.892	0.2349	35.407	2.881	-4.702
3000	91.667	9.952	0.1977	31.039	1.750	-5.291
3000	73.333	10.034	0.1464	27.813	-1.161	-6.643
3500	113.333	11.581	0.2484	38.795	5.613	-4.096
3500	96.667	11.656	0.2019	34.296	3.168	-5.351
4000	133.333	13.219	0.2946	46.834	10.096	-2.402

A.5. Eccentric Geometry Test #3

Power [W]	J_v [m/s]	J_l [m/s]	Film Thickness [mm]	T_{top} [℃]	T_{bottom} [℃]	HTC [$W / m^2 \cdot K$]
2000	6.221	0.3802	0.3537	51.924	53.675	3366.31
2000	6.328	0.3150	0.3669	52.146	54.379	3382.46
2000	6.381	0.2824	0.3516	51.808	54.000	3475.64
2000	6.450	0.2405	0.3625	51.534	53.623	3568.18
2000	6.481	0.2219	0.3542	51.457	53.419	3600.93
2500	7.994	0.3425	0.3794	55.708	56.542	3571.75
2500	8.078	0.2913	0.3540	55.117	56.034	3710.38
2500	8.139	0.2540	0.3555	54.784	55.543	3798.35
2500	8.208	0.2121	0.3532	54.712	55.298	3843.89
2500	8.242	0.1911	0.3344	54.267	54.803	3944.60
3000	9.759	0.3095	0.3715	58.157	57.857	3918.58
3000	9.836	0.2629	0.3519	57.709	57.480	4023.95
3000	9.912	0.2163	0.3464	57.319	57.127	4122.94
3000	9.977	0.1767	0.3390	56.618	56.392	4278.71
3000	9.996	0.1651	0.3245	60.204	56.069	3700.11
3500	11.540	0.2671	0.3499	64.639	59.153	3653.32
3500	11.593	0.2345	0.3622	64.855	58.793	3644.57
3500	11.647	0.2019	0.3392	118.184	57.998	1341.95
4000	13.198	0.2993	0.3653	66.975	60.746	3882.27

A.6. Pressure Drop of Test #3

Power [W]	Inlet Mass Flow Rate [g/s]	J_v [m/s]	J_l [m/s]	Gauge Pressure [kPa]	Total Pressure Drop [kPa/m]	Pressure Drop at the Annular Region [kPa/m]
2000	155.000	6.198	0.3942	35.336	3.423	-2.682
2000	136.667	6.282	0.3430	33.477	2.346	-3.837
2000	121.667	6.351	0.3011	30.796	1.519	-4.740
2000	107.500	6.416	0.2615	29.418	0.350	-5.508
2000	93.333	6.481	0.2219	28.066	-1.020	-5.934
2500	138.333	8.001	0.3379	37.942	3.923	-4.048
2500	128.333	8.047	0.3099	35.548	3.733	-4.464
2500	110.000	8.131	0.2587	33.249	1.923	-5.266
2500	98.333	8.185	0.2261	30.974	1.174	-5.217
2500	85.000	8.246	0.1888	29.078	-0.639	-6.269
3000	135.000	9.744	0.3188	40.163	6.006	-3.869
3000	115.833	9.832	0.2652	37.910	3.963	-4.388
3000	103.333	9.889	0.2303	34.595	2.677	-5.540
3000	83.333	9.981	0.1744	32.005	0.183	-6.010
3000	75.000	10.019	0.1511	29.760	-0.755	-6.415
3500	128.333	11.502	0.2904	42.128	7.301	-3.796
3500	109.167	11.590	0.2369	38.497	5.010	-4.795
3500	96.667	11.647	0.2019	37.549	3.263	-5.644
4000	126.667	13.237	0.2760	46.000	7.896	-4.559

APPENDIX B

PLOTTED RESULTS

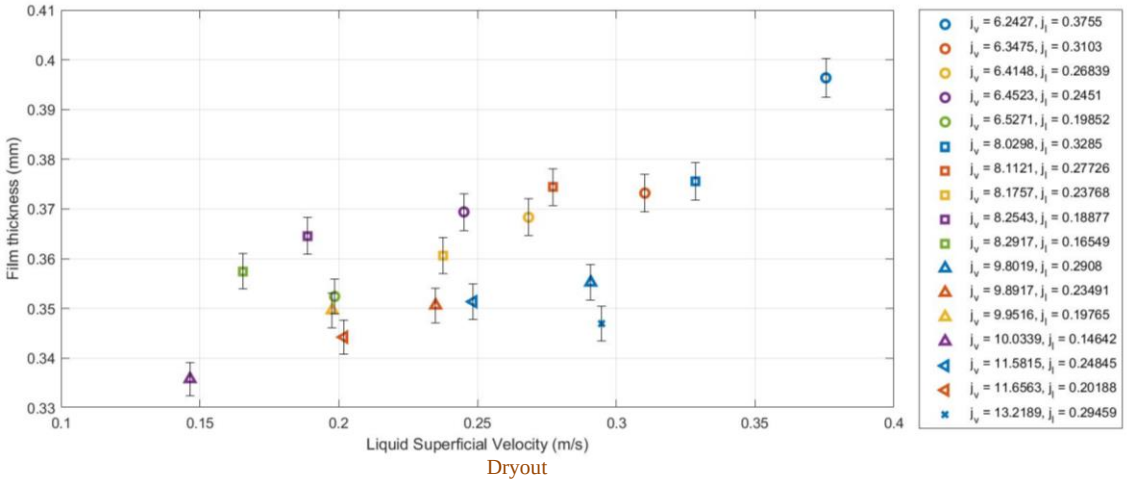

(a)

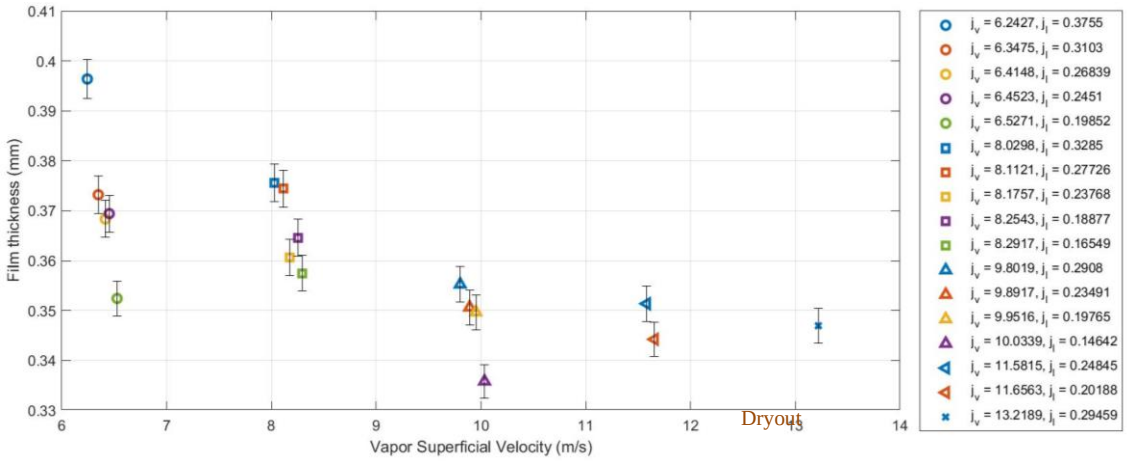

(b)

Figure A.1. Thickness of concentric case plotted against (a) liquid superficial velocity, (b) vapor superficial velocity.

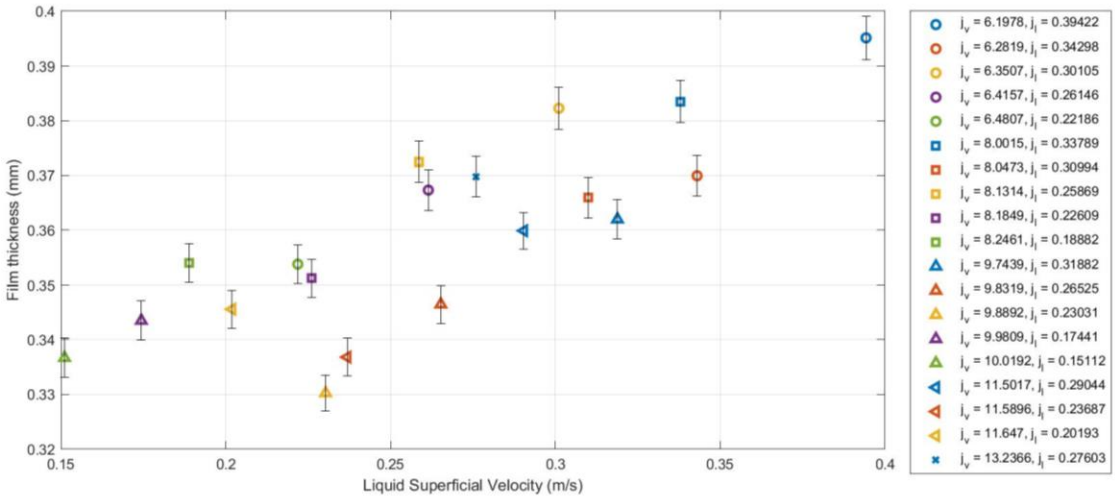

(a)

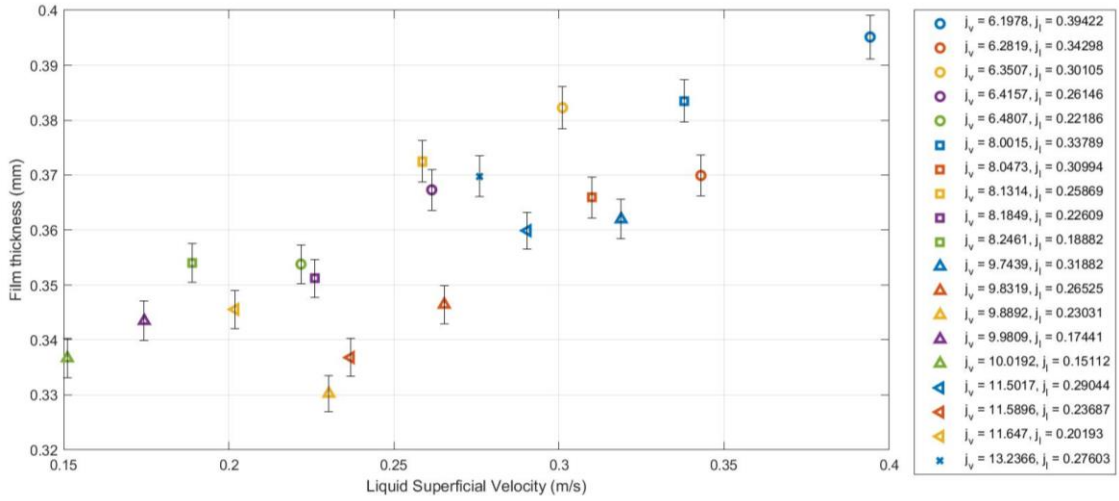

(b)

Figure A.2. Thickness of eccentric case (CCS, large gap side) plotted against (a) liquid superficial velocity, (b) vapor superficial velocity.

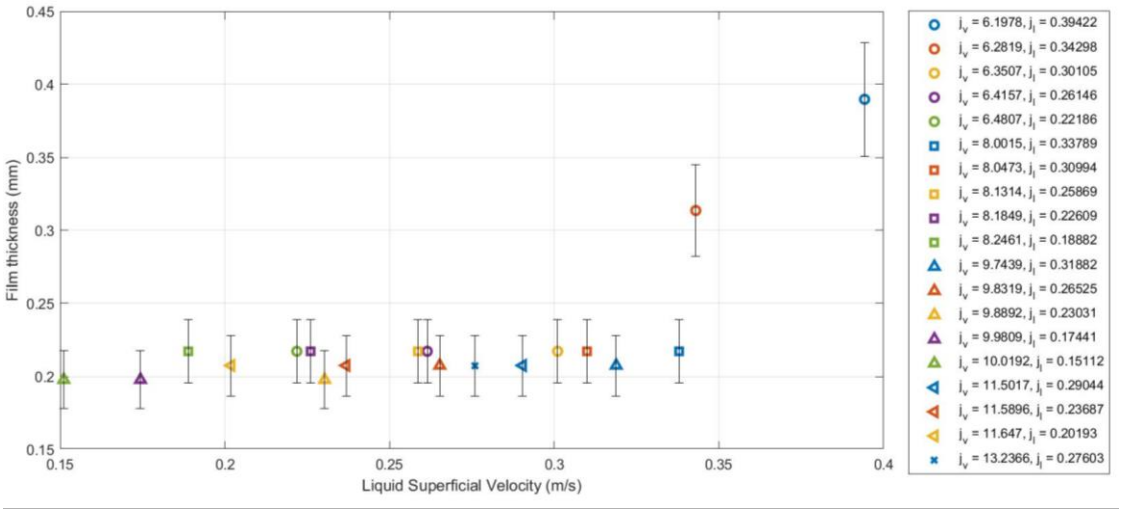

(a)

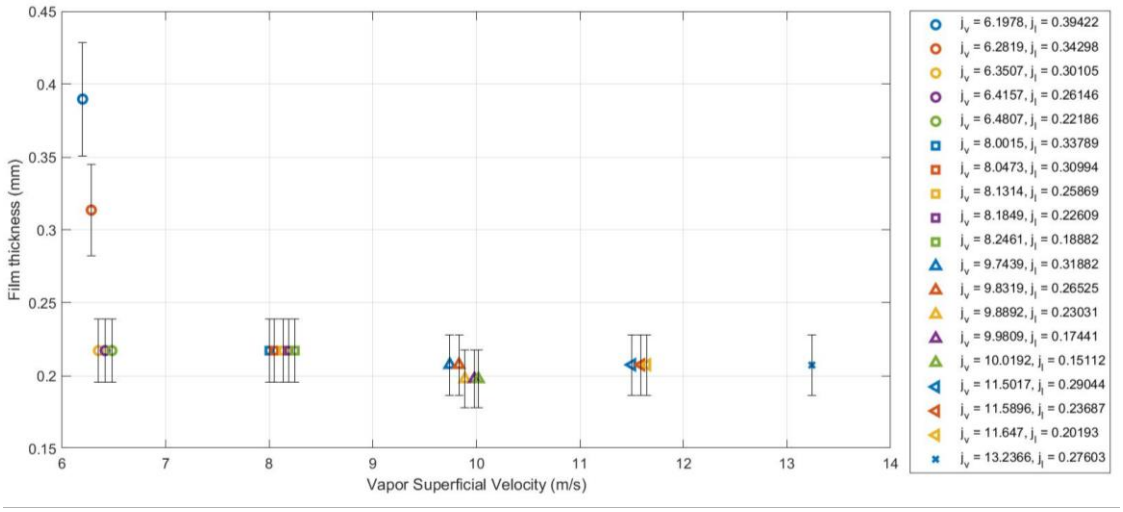

(b)

Figure A.3. Thickness of eccentric case (LIF, small gap size) plotted against (a) liquid superficial velocity, (b) vapor superficial velocity.

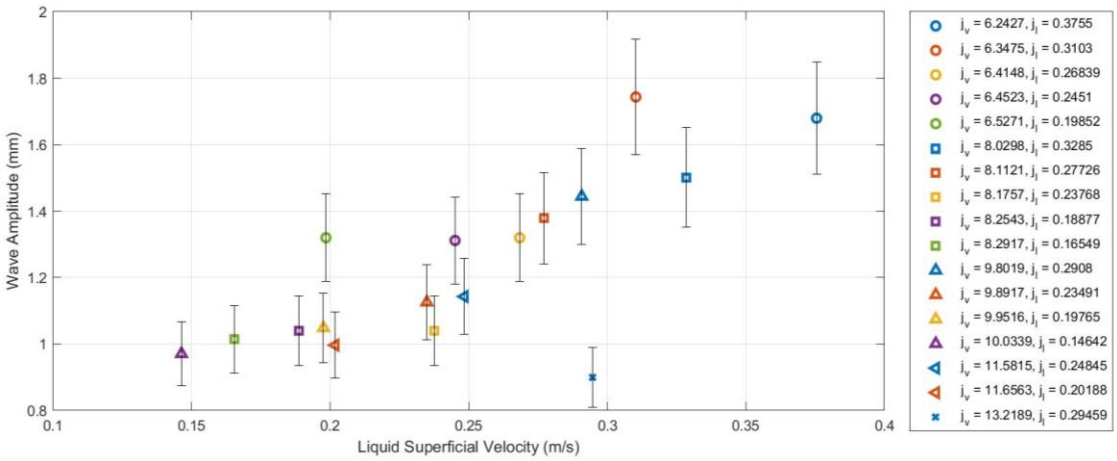

(a)

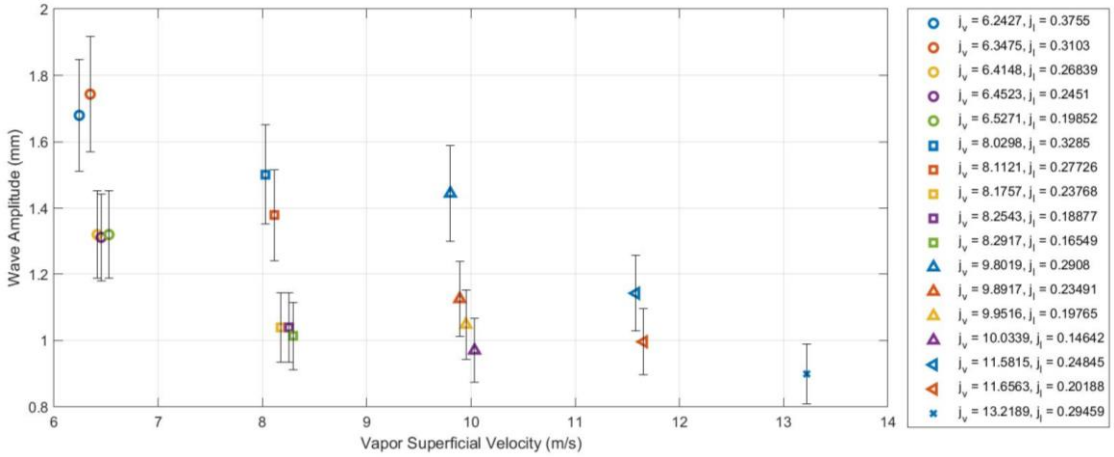

(b)

Figure A.4. Wave amplitude of concentric case plotted against (a) liquid superficial velocity, (b) vapor superficial velocity.

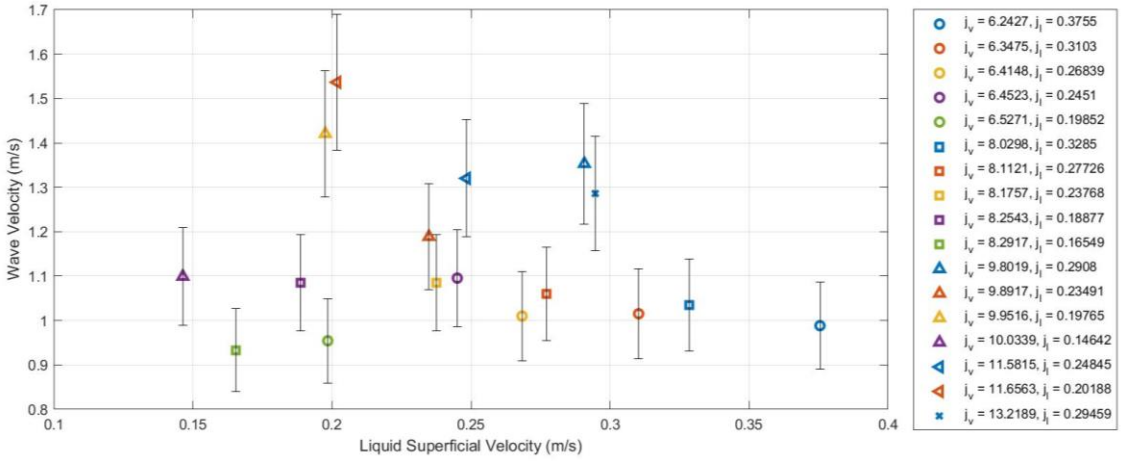

(a)

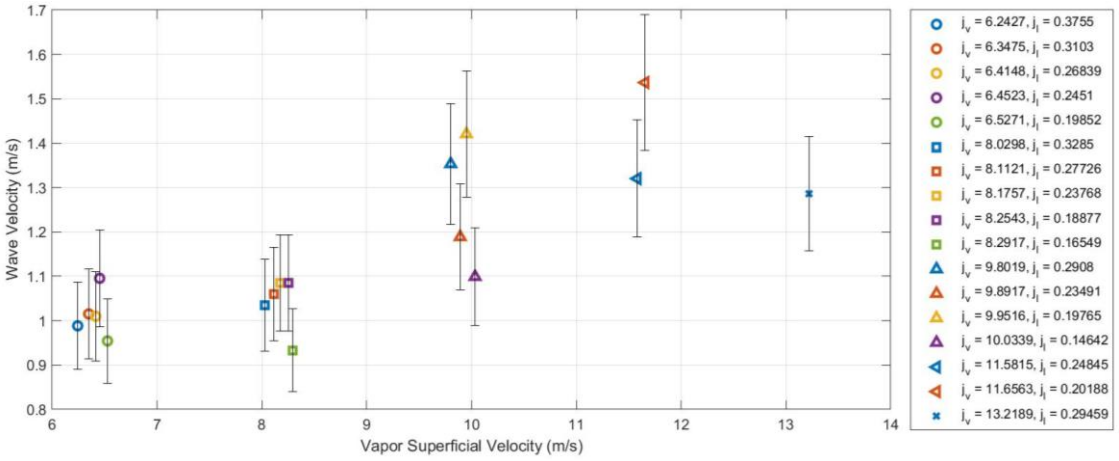

(b)

Figure A.5. Wave velocity of concentric case plotted against (a) liquid superficial velocity, (b) vapor superficial velocity.

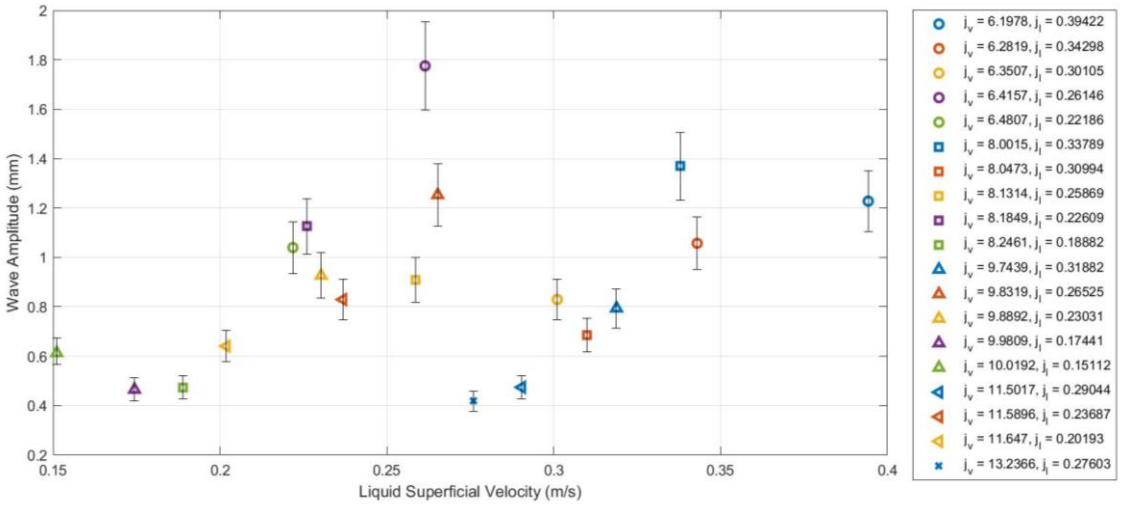

(a)

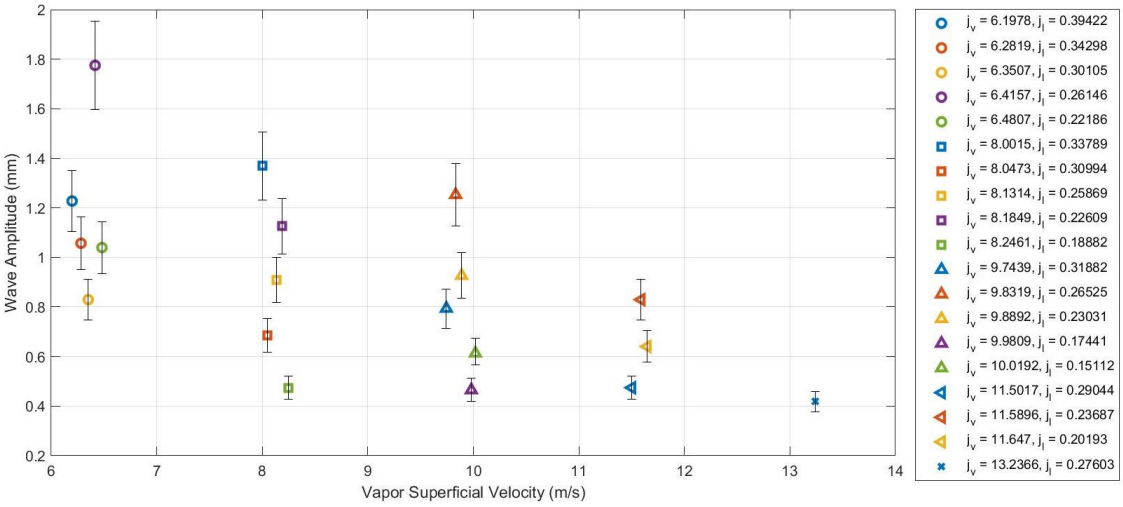

(b)

Figure A.6. Wave amplitude of eccentric case plotted against (a) liquid superficial velocity, (b) vapor superficial velocity.

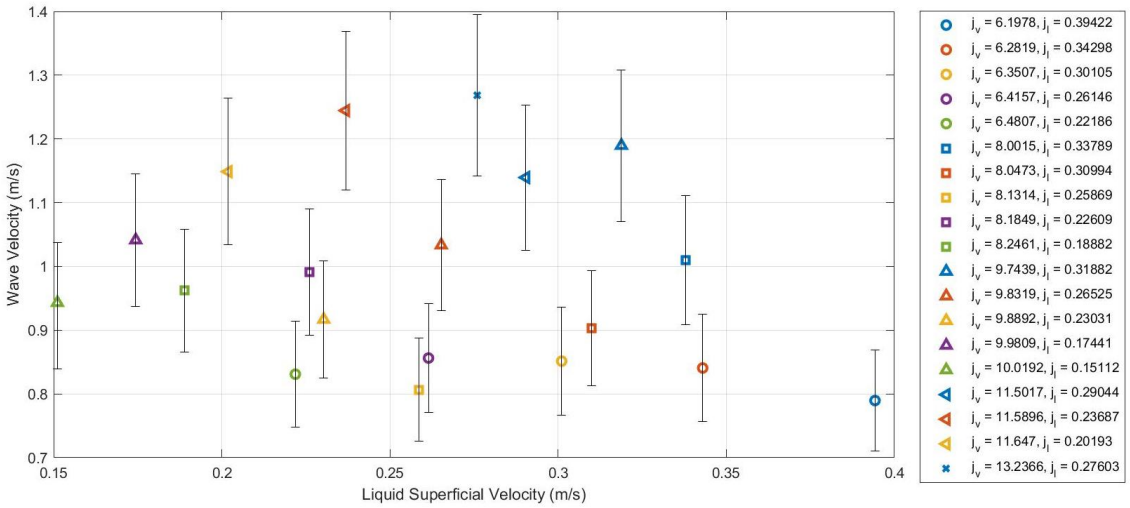

(a)

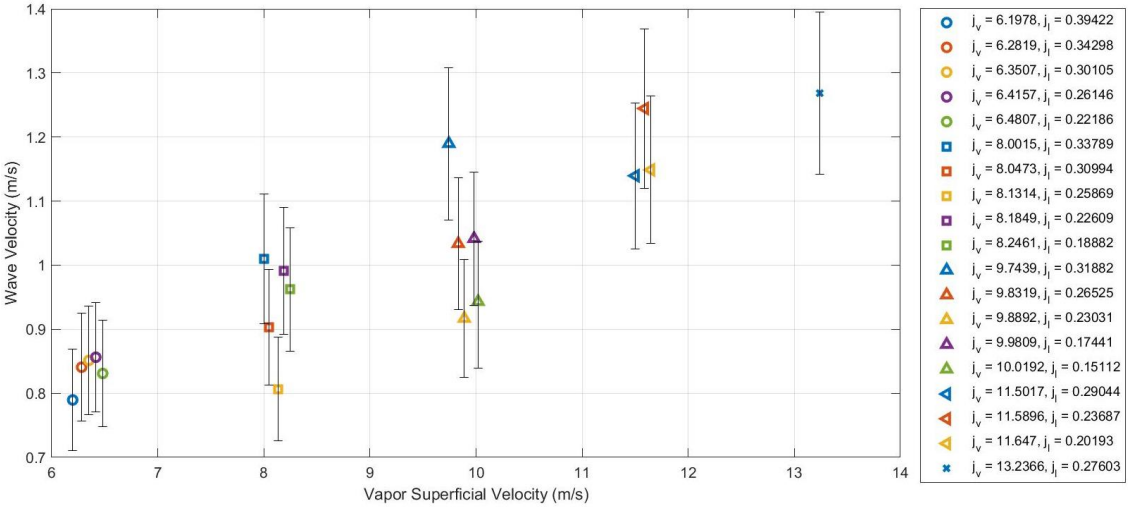

(b)

Figure A.7. Wave velocity of eccentric case plotted against (a) liquid superficial velocity, (b) vapor superficial velocity.

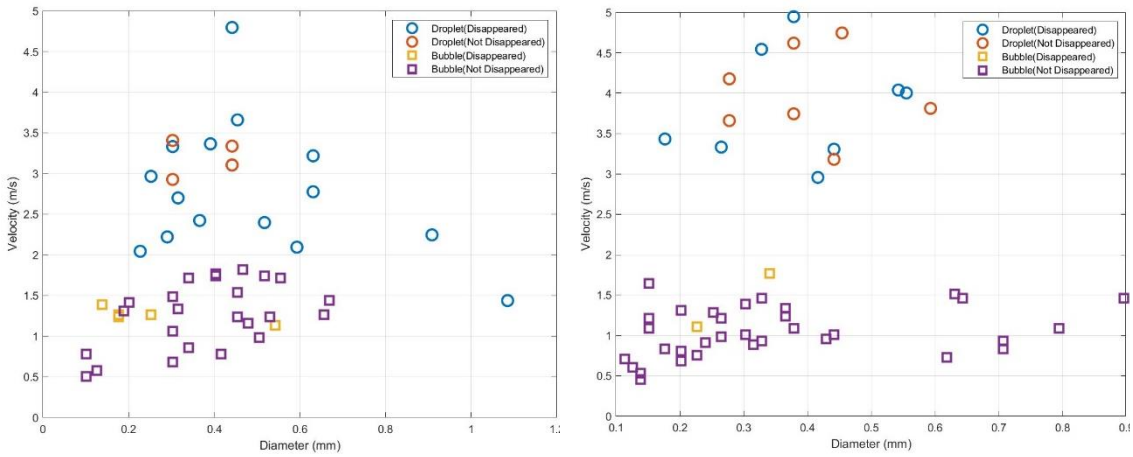

Figure A.8. Size and velocity distributions of droplets and bubbles with boundary conditions, (a) j_v=9.744, j_l=0.3188 (b) j_v=10.019, j_l =0.1511.

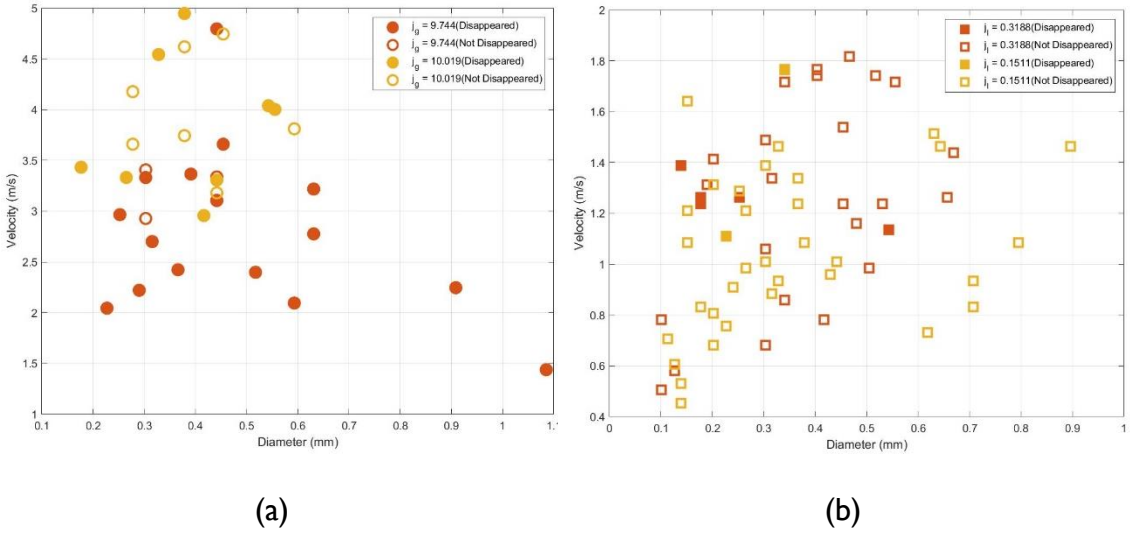

Figure A.9. Size and velocity distributions of (a) droplets and (b) bubbles.

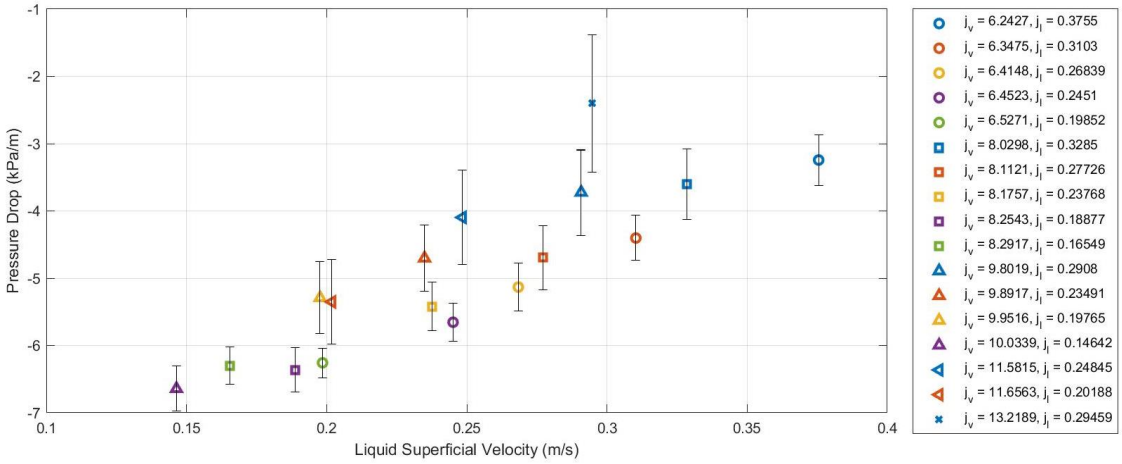

(a)

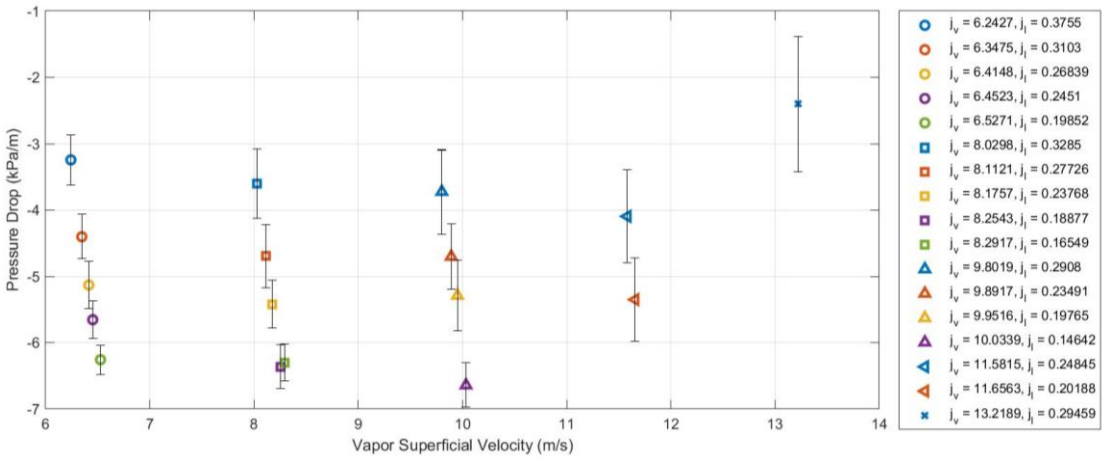

(b)

Figure A.10. Pressure drop of concentric case plotted against (a) liquid superficial velocity, (b) vapor superficial velocity.

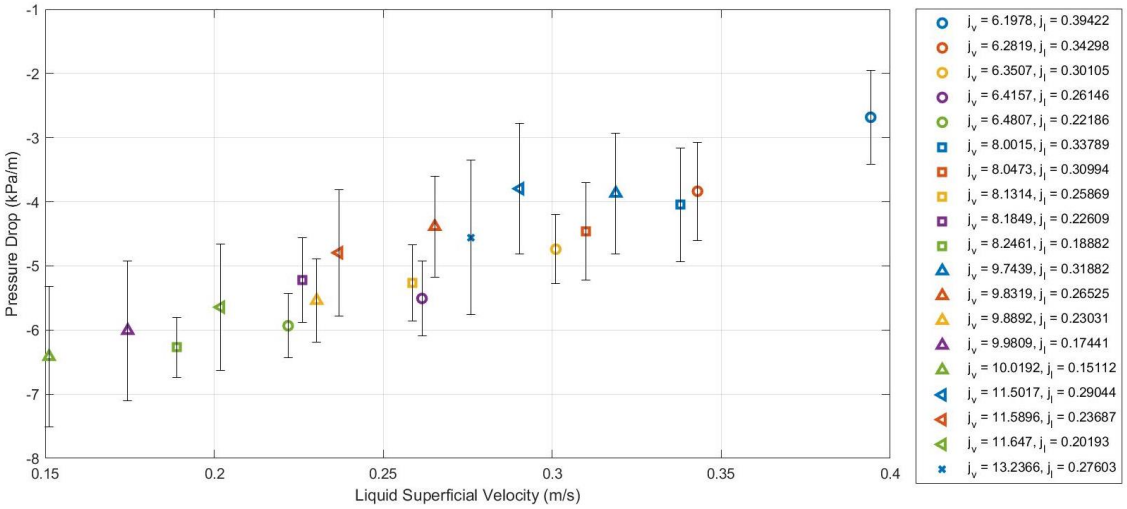

(a)

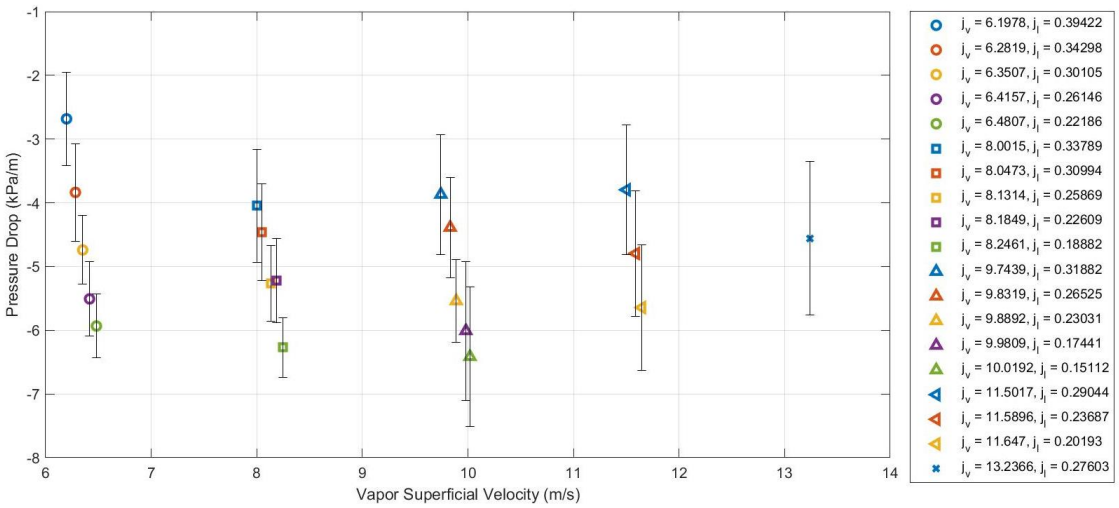

(b)

Figure A.11. Pressure drop of eccentric case plotted against (a) liquid superficial velocity, (b) vapor superficial velocity.

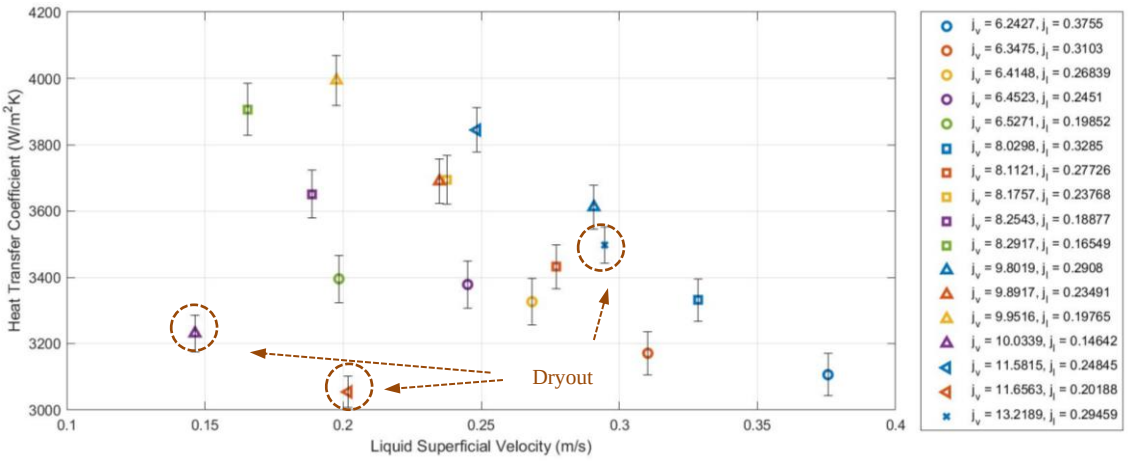

(a)

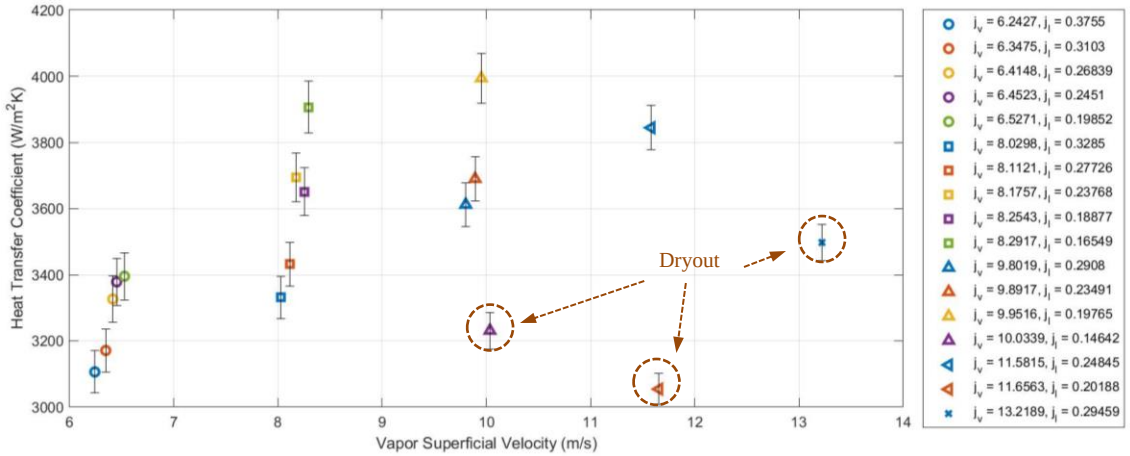

(b)

Figure A.12. Heat transfer coefficient of concentric case plotted against (a) liquid superficial velocity, (b) vapor superficial velocity.

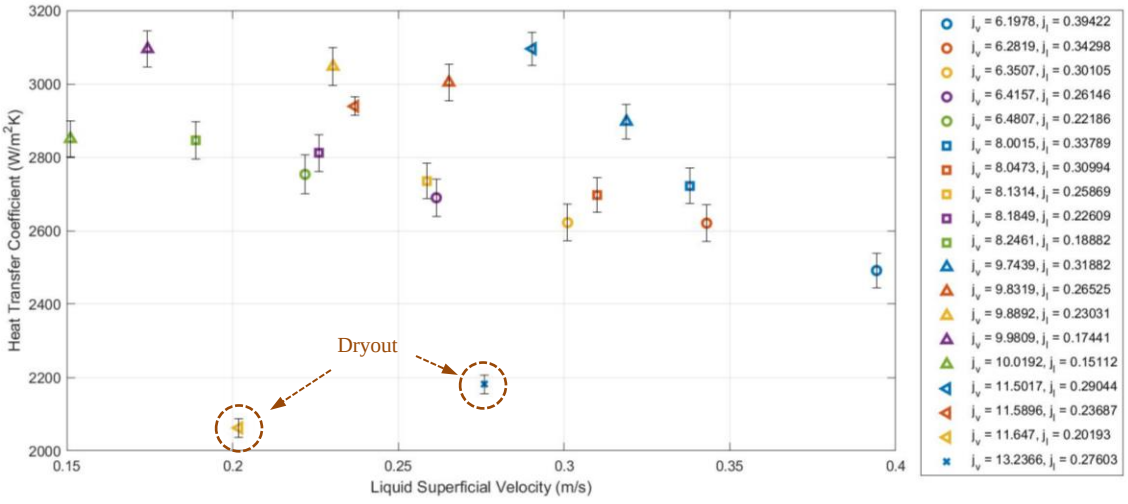

(a)

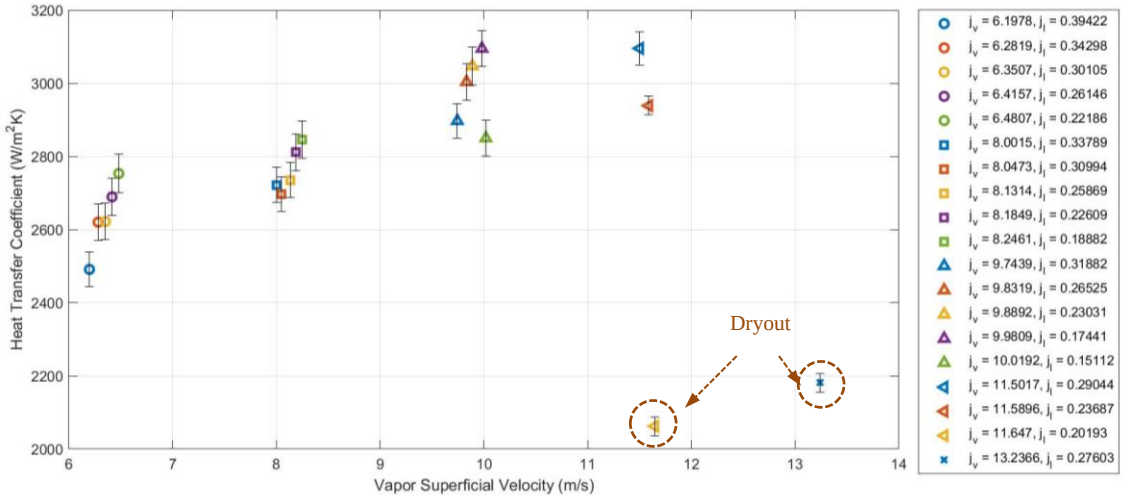

(b)

Figure A.13. Heat transfer coefficient of eccentric case plotted against (a) liquid superficial velocity, (b) vapor superficial velocity.